APPLICATIONS OF LIKELIHOOD ANALYSIS IN GAMMA-RAY ASTROPHYSICS

A DISSERTATION

SUBMITTED TO THE DEPARTMENT OF PHYSICS

AND THE COMMITTEE ON GRADUATE STUDIES

OF STANFORD UNIVERSITY

IN PARTIAL FULFILLMENT OF THE REQUIREMENTS

FOR THE DEGREE OF

DOCTOR OF PHILOSOPHY

By

William Tompkins

March 1999

I certify that I have read this dissertation and that in my opinion it is fully adequate, in scope and quality, as a dissertation for the degree of Doctor of Philosophy.

_____
Peter Michelson
(Principal Adviser)

I certify that I have read this dissertation and that in my opinion it is fully adequate, in scope and quality, as a dissertation for the degree of Doctor of Philosophy.

_____
Vahé Petrosian

I certify that I have read this dissertation and that in my opinion it is fully adequate, in scope and quality, as a dissertation for the degree of Doctor of Philosophy.

_____
Robert Wagoner

Approved for the University Committee on Graduate Studies:

_____

Abstract

The field of γ-ray astronomy relies heavily on the statistical analysis of data. Because of the paucity of data, and the often large errors associated with detecting γ-rays, analysis and interpretation of the data require sophisticated statistical techniques. Techniques for extending the currently used maximum likelihood technique to more complicated data sets are presented. Similarly presented are methods of calculating the distribution and behavior of the maximum likelihood statistic used to measure source significance.

A new method for calculating source variability is also proposed, and used to examine the sources found by the Energetic Gamma Ray Experiment Telescope (*EGRET*) on board the Compton Gamma Ray Observatory (*CGRO*). The results show that the Active Galactic Nuclei (AGN), pulsars, and unidentified sources have markedly different variability, and that the unidentified sources fall into at least two classes, differing in variability and spatial distribution. A class composed of possible Supernova Remnant associations (SNR) is distinctly more variable than the pulsars, but has a variability consistent with that of the other low latitude unidentified sources.

Finally, the results of the Fall 1997 *GLAST* prototype beam test are presented. The results of the beam test are compared with simulated results, and found to be in remarkably good agreement.

Acknowledgements

As the eighth and final Stanford Ph.D. produced by the Stanford *EGRET* project, I once again repeat our gratitude to those in the collaboration who have made our work possible. I am deeply indebted to all of those people at Goddard Space Flight Center, the Max Plank Institut für Extraterrestriche Physik, Hampden-Sidney College, Grumman Aerospace, and Stanford University who worked so hard for so many years to design, build, fly and support the *EGRET* instrument. Similarly, I would like to thank those whose analytical work I have tried to build upon, specifically Tom Loredo, for his papers on Bayesian methods in Astrophysics, and John Mattox, for his `LIKE` program.

I have learned a great deal from many of those on the *EGRET* team, as well as the outside scientists who work in the high energy γ-ray region; too many people to list individually here. But specifically, I would like to thank Dave Thompson and Bob Hartman at Goddard for their help and guidance, and their interest in my research.

The *GLAST* collaboration is similar in scope, and again there are too many to thank individually. I would like to mention Steve Ritz, Toby Burnett, and Eric Grove as some of those who always surprised me by listening as if I knew what I were talking about, and who made me feel like a scientist rather than a grad student lackey.

Closer to home are the people I have worked with at Stanford and SLAC. Bill Atwood taught me a great deal about particle physics, but more important to me was the implicit trust he showed in my abilities as a physicist during the beam test. No mention of the beam test can be made without a reference to Chris Chaput as well, without whom the whole process would have taken much more time, and been much less fun.

I am frequently amazed at the freedom given me by Peter Michelson, my advisor, to pursue those research areas which I have found most interesting. In addition to finding the funding for all of my research, Peter has always supported my efforts, even when they threatened to veer from astrophysics into statistics. Helping keep the Stanford group focused on the astrophysics has been Y.C. Lin, who always seems to stay focused on the science, even when the rest of us get bogged down in the systematics.

Pat Nolan wears many different hats in the Stanford group, and I owe him thanks in each of his different roles. As the institutional memory of the Stanford *EGRET* group, he has taught a succession of graduate students about the instrument, about the analysis, and about the science. He has always been willing to help when I have difficulty, whether that is with understanding a theory or proofreading a paper. I knew that I was finally ready for my Ph.D. when he actually asked *me* for advice. In addition to his role as a research scientist, Pat is invaluble as the person who keeps the *EGRET* computers running. Without him, there would be chaos.

Each graduate student learns a tremendous ammount from the preceeding grad students, and I am no exception. Joe Fierro and Tom Willis were both far more patient than I would have been, as they explained elementary astronomy or the mysterious workings of *EGRET* to me. Mallory Roberts was good to talk to for a non-*EGRET*-team perspective. The fellow graduate student to whom I owe the most, however, is Brian Jones, a friend for nearly ten years, a roommate for three, and an officemate for over five. In our constant discussions and arguments we managed to learn a great deal of physics and statistics.

Other friends in the Stanford Physics department have also been great friends, most particularly Doug Natelson. It was always refreshing to hear the perspective of a non-astrophysicist. Plus, he can make a good curry.

My family has been tremendously supportive during my long trek towards a doctorate. Even if they weren't sure if I knew what I was doing, my parents have always been great.

I end the list with both the most important scientist in my life, and my wife-to-be: Barb Reisner. I owe her more than words can express.

For my parents

Contents

List of Tables

List of Figures

xviii

Chapter 1

The Sky in Gamma-Rays

In the quest to understand the nature of the more enigmatic astrophysical objects, astronomers have constantly sought new sources of data. One means of seeing the different aspects of these objects is to look at them in different wavelengths, as was first done in the 1930s when the radio range was first explored. Later, with the advent of spaceborne detectors, the X-ray, infrared, and ultraviolet regions began to be explored in detail as well. One of the last wavelength bands to be opened was the γ-ray region, due to the low fluxes of cosmic γ-rays and the high backgrounds with which the instruments must cope. A summary of the instrumental history is given in Chapter 2.

Each new band has presented a unique way of studying the universe, and the high energy γ-ray region (20 MeV – 100 GeV) is no exception. Many of the most energetic sources in the sky emit most of their observable energy output in γ-rays. To understand the source, one must understand the energy production. And to measure the energy production, one must look at the γ-rays. In addition, γ-rays from distant objects generally proceed unimpeded from their source to the earth. A visible photon has a 99.995% chance of being absorbed as it passes through the central disk of our galaxy, while a γ-ray photon has about a 1% chance of interacting [30]. Thus, γ-rays come to us directly from their production site, allowing astrophysicists access to the inner details of the objects they study.
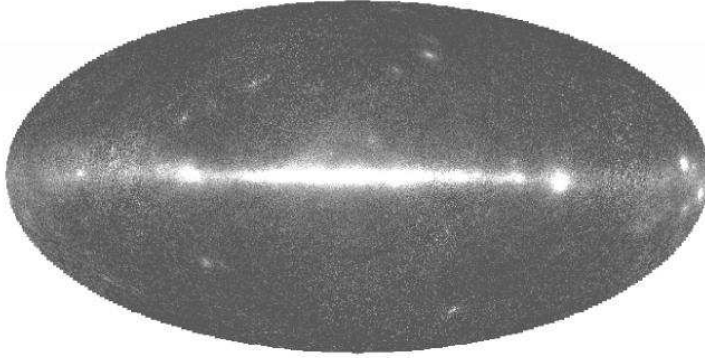
Figure 1.1:   The γ-ray sky above 100 MeV, as measured by *EGRET*.

1.1   Diffuse Emission

1.1.1   Galactic Emission

While dust and gas in our galaxy does not absorb the γ-rays from distant objects, it does obscure them in a different way. Cosmic rays interacting with galactic gas make the galactic disk the brightest γ-ray source in the sky, and can make it difficult to find fainter sources. But one person's background can be another person's treasured signal: this galactic emission (in conjunction with radio maps indicating where the gas is) can be used to infer the cosmic ray density function [7, 45, 44].

Because of the large point spread functions on γ-ray telescopes, it is difficult to resolve many of the weaker sources. Some of the apparently diffuse galactic emission will no doubt turn out to be from unresolved γ-ray pulsars (§1.2.1). In turn, some of the γ-ray sources currently in catalogs are probably due to enhanced diffuse emission, rather than being from a compact object.

There is also a γ-ray source at (or near) the center of our galaxy [65]. The strong diffuse emission makes it difficult to study, but it does have a pulsar-like (and not diffuse-like) energy spectrum, leading to the hypotheses that it might be multiple pulsars, or perhaps diffuse emission from a region with a peculiar cosmic ray spectrum. Other possibilities have been suggested, including that of emission from a central black hole, or the possibility of dark matter annihilation at the galactic core.

The merits of these various hypotheses are discussed at length by Mayer-Hasselwander [65].

The Large Magellanic Cloud (LMC) is the only normal galaxy other than our own which is visible in high energy γ-rays. The emission from this dwarf companion galaxy to the Milky Way is consistent with the expected diffuse emission from the same cosmic ray interactions which produce the diffuse background in our own galaxy [88, 62]

1.1.2 The Extra-Galactic Background

In addition to the diffuse Galactic γ-ray background, there is an apparently isotropic background flux of γ-rays. This presumably extragalactic background has an energy spectrum consistent with that of the AGN, and is probably composed mainly (or fully) of sub-threshold AGN [89, 103]. It is interesting to speculate on sources of a truly isotropic γ-ray background, but experimental results will have to wait for the next generation of γ-ray telescopes.

1.2 Point Sources

1.2.1 Pulsars

The only identified compact sources of γ-rays in our galaxy are the six γ-ray pulsars [32, 33, 75, 77, 97, 99]. They exhibit fairly hard spectra in the *EGRET* energy range, and show little sign of variability (§8.4). Sophisticated models of the γ-ray production have been developed, notably the outer gap [18, 19, 82, 104] and the polar cap [39, 22] models, but current observations are not sufficiently precise to distinguish them.

1.2.2 Active Galactic Nuclei

Ninty-three of the 271 *EGRET* sources are BL Lacertae (BL Lac), Optically Violent Variable (OVV) Quasi-Stellar Objects (QSO), or high-polarization QSO, which are

collectively termed blazars, and one is the radio galaxy Cen A [40]. These objects are all termed Active Galactic Nuclei (AGN), together with many objects which are not seen in γ-rays such as the Seyfert galaxies (type I and II) and other types of QSO. The unified AGN model indicates that all of the above, observationally different, objects are in fact same type of object: a supermassive black hole at the center of a galaxy, surrounded by a hot accretion disk, and producing relativistic jets of charged particles. This system is surrounded by a torus of gas which obscures the central disk from many angles. The observational differences between the classes of AGN stem from the orientation of the jets compared to the line of sight, as well as the size of the central black hole, and its accretion rate.

The blazars are those AGN which have their jets pointed at us, and the high energy emission is produced by the relativisic jet. The most plausible mechanism for the power-law emission seen at *EGRET* energies is the "synchrotron self-Compton" (SSC) process, whereby synchrotron photons emitted by the electrons in the jet at radio to X-ray energies are scattered by other electrons in the jet into γ-ray energies.

AGN are dramatically variable in γ-rays. Flares typically last tens of days, but variability is seen from day to day as well [12]. The energy spectrum is typically a power law with index ≈ -2.1.

1.2.3   The Unidentified Sources

Well over half of the *EGRET* sources do not have identified counterparts in other wavelengths. This is primarily due to the large error regions obtained: there are frequently multiple possible counterparts within the 95% error ellipse. Many of the high latitude unidentified sources will no doubt be identified as AGN, but there is also a population of galactic unidentified sources [53, 38]. Some of these are probably pulsars, but many are not, as evidenced by their variability (§8.4), energy spectrum [69, 73], and the sheer number of sources. The puzzle of the nature of these unidentified sources is an exciting challenge to the next generation of γ-ray telescopes.

1.2.4 Gamma-Ray Bursts

Since 1967, flashes of γ-rays have been observed from the sky. These bursts are often much brighter than the rest of the sky at their peak, and show variation on a time scale of a few milliseconds.

Soft Gamma Repeaters

A few of these bursts, with softer energy spectra, were seen to burst repeatedly from the same spot on the sky. Four different "Soft Gamma Repeaters" have been identified, three of which are identified with supernova remnants [58]. The inferred neutron star origin of these burst has been confirmed with X-ray observations.

Classical Gamma-Ray Bursts

More puzzling are the so-called "classical" gamma ray bursts, which are much more numerous than the SGRs. These are apparently extragalactic in origin, implying that enormous energies are involved. Most of the science on γ-ray bursts has been done at lower energies, specifically by the *BATSE* [67, 68] and *BeppoSAX* [35] instruments, but very large fluxes above 30 MeV have been observed with *EGRET* as well [61, 17, 23, 85, 87, 84]. In addition, *EGRET* made the remarkable discovery of delayed high energy emission from an apparently brief burst. The observation by *EGRET* of an 18 GeV photon over an hour after a burst was seen by *BATSE* was quite unanticipated by theory [46].

1.2.5 Local Gamma Ray Sources

The Sun

The quiescent sun is not visible in γ-rays, although there is presumably a low γ-ray flux from interactions between cosmic rays and gas near the surface of the sun [94]. Solar flares, however, can be extremely bright in high-energy γ-rays [52]. Because the large flux of X-rays accompanying a flare trigger the anti-coincidence shield of a γ-ray telescope, it is difficult to measure the true flux from a bright flare.

The Moon and Planets

Cosmic ray interactions with the lunar surface produce a low flux of high energy γ-rays, which has been detected by *EGRET* [94]. In addition, lower energy γ-ray spectrometers have been part of missions to the Moon, Mars, and a near Earth asteroid. The γ-ray lines detected have been used to measure the isotopic and elemental abundances in these objects, and thus yield clues to their formation.

The Earth

The material at the surface of the Earth produces these same low energy γ-ray lines. In addition, flashes of low energy γ-rays from lightning have been observed by *BATSE*. The largest source of terrestrial source of γ-rays for an orbiting telescope, however, is the atmosphere. Cosmic ray interactions with the Earth's atmosphere produce showers containing a very large flux of high energy γ-rays. These showers proceed in the same direction as the cosmic ray, and must originate in the atmosphere: thus these γ-rays are seen to come from the edge of the Earth's disk, rather than uniformly across the disk [93].

The rejection of this γ-ray background is based on direction. The combination of directional cuts, together with the significant width of the point spread function for γ-ray telescopes can make analysis difficult, and lead to spurious detections if one is not careful [103].

Chapter 2

Spaceborne Gamma-Ray Telescopes

2.1   Principles of Gamma-Ray Detection

There are a number of different methods for detecting γ-rays. At lower energies (100 keV – 30 MeV), either crystal scintillators or semiconductors are typically used. Both types of detectors rely on the ionization caused by the passage of the gamma ray: in a semiconductor the electrons and holes are collected with an electric field, while in a scintillator they produce visible photons which are then amplified with a photomultiplier tube. The energy of the gamma ray can be measured by the ionization response. A number of different means can be used to measure the direction of the gamma ray, including the use of a collimator, a coded aperture in conjunction with a position sensitive detector, multiple position sensitive layers (measuring two successive Compton scatters at the higher energies), or time of flight information between physically separated detectors.

At higher energies ($>$ 10 MeV), the dominant interaction in a high-Z material is the conversion of the γ-ray into an e^+/e^- pair. A succession of detectors which measure the ionization produced by the pair of charged particles can reconstruct incident γ-ray direction. The energy of the γ-ray can be measured by the scattering of the e^+ and e^- tracks in the detector material, but better measurements can be

obtained with a calorimeter (generally a scintillator) positioned behind the tracking detector.

2.2   Early Gamma-Ray Instruments

2.2.1   Balloon experiments

In the 1940's, experiments began to be flown on balloons, airplanes, and rockets to determine the nature of cosmic rays, using Geiger-Müller tubes [83], ionization chambers [43], and cloud chambers [21]. Although experimentalists searched for a primary γ-ray component, the difficulties presented by the low rate of celestial γ-rays, the high backgrounds, and immature balloon technology defeated experimentalists for twenty years. After the first satellite detections, a balloon-borne experiment did confirm the Galactic plane emission in 1970 [56]. Another balloon experiment provided the first evidence of pulsed γ-rays from the Crab pulsar in 1971 [14].

2.2.2   Early satellites

The first detection of astrophysical γ-rays was in 1962, when an instrument on board the moon probe *Ranger 3* detected an apparently isotropic flux of γ-rays [3]. In 1968, an experiment on board the third Orbiting Solar Observatory (*OSO-3*) detected a total of 621 events above 50 MeV, with an apparent excess along the Galactic plane and at the Galactic center [20].

The *OSO-3* instrument consisted mainly of scintillation detectors read out by photomultiplier tubes. The initial conversion was detected with four successive plates of scintillator: two of CsI followed by two plastic planes (Figure 2.1). The pair then passed through a Čerenkov telescope composed of a lucite block and a photomultiplier tube, which ensured that the particles were directed down, rather than up. A calorimeter composed of a block of NaI followed by alternating layers of tungsten and NaI was used for an energy measurement. The entire apparatus was enclosed in plastic scintillator used as an anti-coincidence shield. Because the telescope did not track the positions of the e^+/e^- pair, it did not make any measurement of the

direction of the γ-rays. The limited directional response of about 15°, however, acted as a collimator.
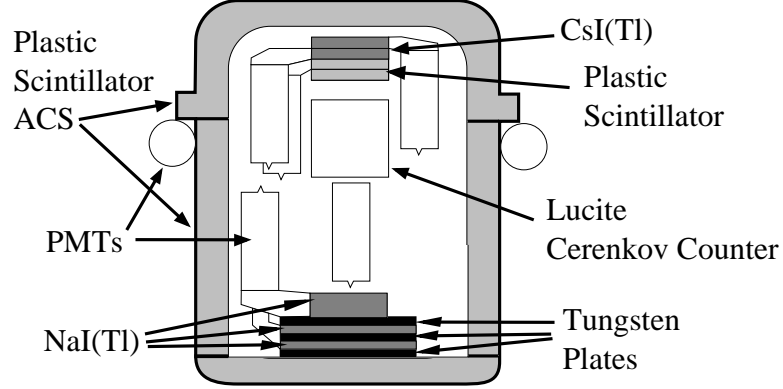
Figure 2.1: Schematic diagrams of the *OSO-3* instrument.

The instrument suffered from calibration problems which were resolved with the aid of the following balloon-borne instruments [59]. The effective area at multi-GeV energies was approximately 9 cm^2.

2.2.3 *SAS-2* and *COS-B*

In 1972, the second Small Astronomy Satellite (*SAS-2*), was launched, containing a γ-ray telescope with a peak effective area of about 115 cm^2. As important as the increased effective area was the directional resolution of the on-board spark chamber (Figure 2.2): about 5° at 30 MeV and 1° at 1 GeV.

The *SAS-2* detector measured the e^+/e^- tracks in the spark chamber to provide both the direction of the incoming γ-ray, as well as the energy (by measuring the scatter of the track). A set of scintillator tiles in the middle of the spark chamber, together with the Čerenkov detector below, provided the trigger for the spark chamber.

Due to the failure of a power supply, *SAS-2* only took data for slightly over six months. During its operation, it detected over 8000 γ-ray events, and identified emission from the Crab [95] and Vela pulsars [96]. In addition, it found the the first

γ-ray source which was not immediately associated with an object detected in other wavelengths: Geminga [57, 31].
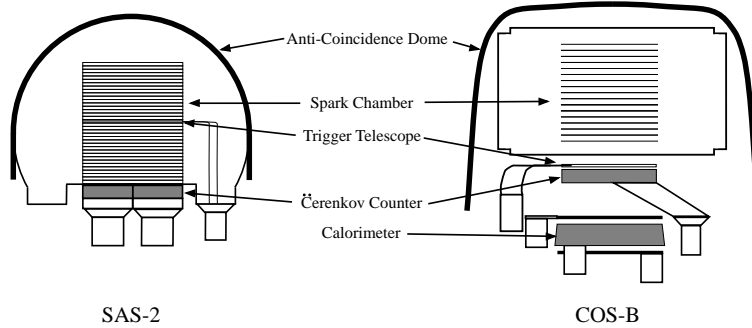
Figure 2.2:   Schematic diagrams of the *SAS-2* and *COS-B* instruments.

The *COS-B* instrument, launched in 1975, was similar in design and capability to the *SAS-2* mission. It did incorporate a calorimeter (Figure 2.2), and thus provided improved energy resolution. The seven year lifetime of the *COS-B* instrument provided much improved measurements of the previously detected sources, as well as establishing many new detections, resulting in 17 sources detected along the galactic plane [8, 64].

2.3   *CGRO*: a New Era in Gamma-ray Astronomy

In April 1991, the Compton Gamma Ray Observatory (*CGRO*) was launched on board the Space Shuttle Atlantis (STS-37). A product of the NASA *Great Observatories for Space Astrophysics* program, the instruments on board were designed to study the γ-ray sky from 25 keV to more than 10 GeV. Because of the large energy coverage, four different γ-ray telescopes were put on board, each designed for a different energy range and purpose (Figure 2.3).
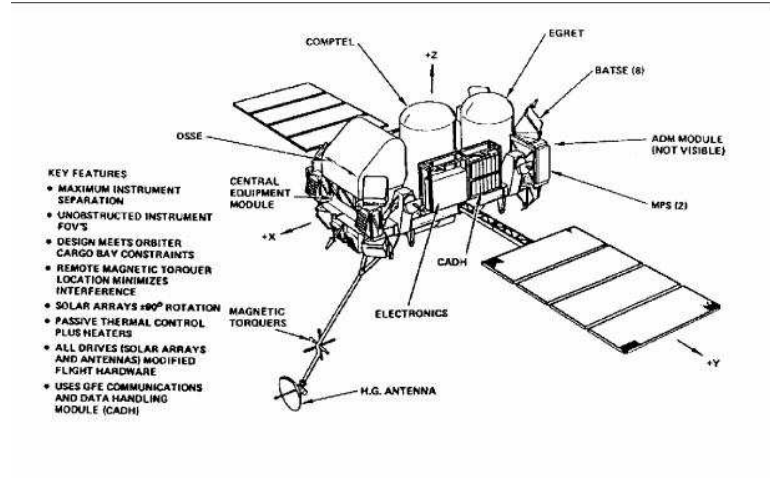
Figure 2.3: The *CGRO* satellite. The *BATSE* detector is comprised of eight distinct pieces on the corners of the spacecraft bus, while along the top of the satellite are *EGRET* and *COMPTEL*, pointing in the Z direction, and *OSSE*, which has its own orientation capability.

2.3.1 *BATSE*

The Burst And Transient Source Experiment (*BATSE*) is a unique γ-ray telescope. Designed to measure quickly varying signals in the 25 keV – 2 MeV region, the *BATSE* detector consists of eight scintillation counters. By comparing the measurements of the different detectors, the position of a flaring source can be ascertained to within about 8°.

2.3.2 *OSSE*

The Oriented Scintillation Spectrometer Experiment (*OSSE*) measures from 50 keV to 10 MeV. With an energy resolution of about 8% and a field of view of 3.8° x 11.4°, it is designed to detect emission lines.

2.3.3 *COMPTEL*

The Compton Telescope (*COMPTEL*) measures double Compton scattering events in two scintillators separated by 1.5 m. In this way, it obtains both the direction

and energy of the incident γ-ray. Its energy range is governed by the region where Compton scattering is a significant interaction process of γ-rays: from 1 – 30 MeV.

2.4 High Energies with CGRO: *EGRET*

The Energetic Gamma Ray Experiment Telescope (*EGRET*) is the successor to the earlier *SAS-2* and *COS-B* instruments (Figure 2.4). Similarly designed with a magnetic core spark chamber, it differs mainly from these previous instruments in its size (Figure 2.6). The triggering of *EGRET* is somewhat different as well: the requirement that the secondary particles have downward trajectories is enforced by a time of flight (TOF) system rather than a Čerenkov telescope. The segmentation of the two TOF planes into two 4x4 arrays of scintillator permits directional triggering as well [98].
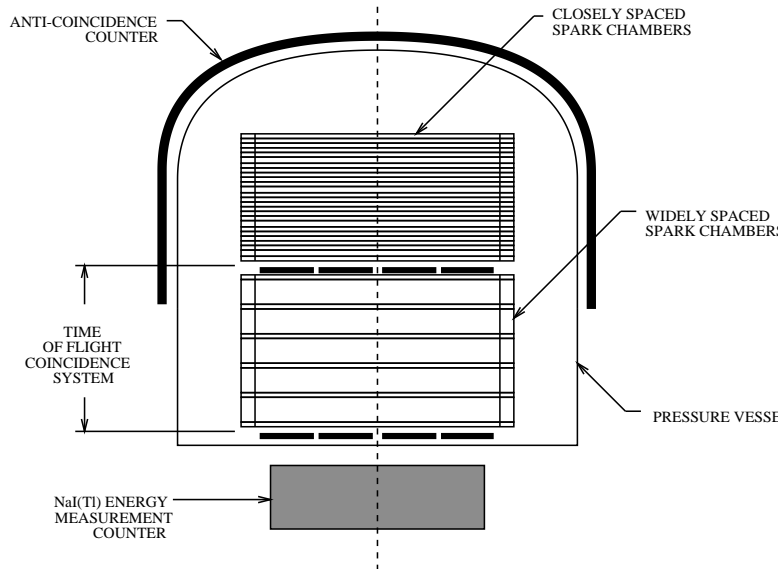
Figure 2.4: Schematic diagram of the *EGRET* instrument.

Of the 256 possible upper-tile/lower-tile combinations, 96 are able to trigger *EGRET*. These correspond to those directions from which the particle would have left a track in the spark chamber. These 96 combinations were grouped into 74 instrument configuration modes [98]. In addition to the typical mode which triggers on

any γ-ray which converted in the tracker, there were other modes designed to limit exposure in a given direction. Thus, the telescope can be pointed near the horizon without being overwhelmed by triggers from Earth albedo γ-rays. Because of failures in the photomultiplier tubes, extra configuration modes have been added during the *EGRET* mission, resulting in 87 different configurations [26].

The *EGRET* tracker consists of 28 closely spaced spark chamber modules, interleaved with sheets of tantalum (Ta). The Ta ($Z = 73$) provides the most likely interaction point for an incoming γ-ray; above the critical energy of 10.7 MeV, this is most likely to be a pair conversion event. Each spark chamber module consists of two orthogonal sets of wires. When triggered by the TOF system (and not vetoed by the anti-coincidence dome), a high voltage is applied across the sets, leading to a spark where the the interior gas has been ionized. The spacing of the wires (0.8 mm) sets the nominal accuracy of the track measurement.

The Total Absorption Shower Counter (TASC) sits below the TOF system, and is comprised of approximately 8 radiation lengths of NaI read out by photomultiplier tubes. It measures the energy of the particle pair with a resolution of about 20% FWHM when both the e^+ and e^- are intercepted. At low energies, this measurement needs to be corrected for the energy lost by the pair as they traverse the spark chamber. At the highest energies, leakage from the TASC becomes an important issue.

Events in *EGRET* are time-tagged with an accuracy of 100 μs, which permits the study of the lightcurve shape of the γ-ray pulsars. The instrumental dead time of 100 ms after each event is rarely a concern, given the low flux of high energy γ-rays. During extremely bright solar flares and bursts, however, *EGRET* has been dead time-limited [52, 87].

The *EGRET* instrument was calibrated before launch at both the Stanford Linear Accelerator Center and the MIT Bates Linear Accelerator [98], resulting in extensive tables of the instrument response to γ-rays with various energies and incident directions for all of the various triggering modes. Further calibration studies have been performed in orbit to ensure that degradation over its nearly eight year lifetime (much

longer than the planned mission length) does not affect the accuracy of the scientific results [26].

The scientific results from the *EGRET* mission are numerous, including the first all-sky survey at high energy γ-ray wavelengths, and comprise nearly all of the high energy results discussed in Chapter 1.

2.5   The Future: *GLAST*

While the *EGRET* instrument improved on the previous γ-ray telescopes mainly in its size, the proposed Gamma-ray Large Area Space Telescope (*GLAST*) gains primarily through improved technology. The proposed *GLAST* baseline instrument[*] is composed of a 5x5 array of towers (Figure 2.5). Each tower has 16 planes of silicon strip detectors, used to track the e^+/e^- pair, a hodoscopic calorimeter with eight layers of CsI logs, and an anti-coincidence detector (ACD) composed of plastic scintillator [70, 4, 10, 11]. The striking differences between the *GLAST* instrument and the previous telescopes are the flattened aspect ratio due to the lack of a time of flight or Čerenkov detector, and the lack of a monolithic anticoincidence shield (Figure 2.6).

These differences are due to the on-board computing power available to the *GLAST* instrument. The discrimination between upward- and downward-going events is handled by on board event reconstruction. Similarly, the rejection of the hadronic background is accomplished by projecting the track back into the segmented ACD, and checking for a hit there. The segmentation of the ACD prevents a veto of the event by backsplash X-rays from the calorimeter triggering the ACD. These structural changes permit a much wider field of view for the instrument, and a higher sensitivity, particularly at high energies where low energy photons produced by the shower in the calorimeter can trigger an anti-coincidence shield.

The technological improvements are not limited to the computers, however. The

---

[*]Alternative technologies have been proposed for the telescope, including scintillating fiber and gaseous detectors. These technologies are somewhat less developed than the silicon strip and CsI detectors discussed here, and thus are not used in this baseline design.
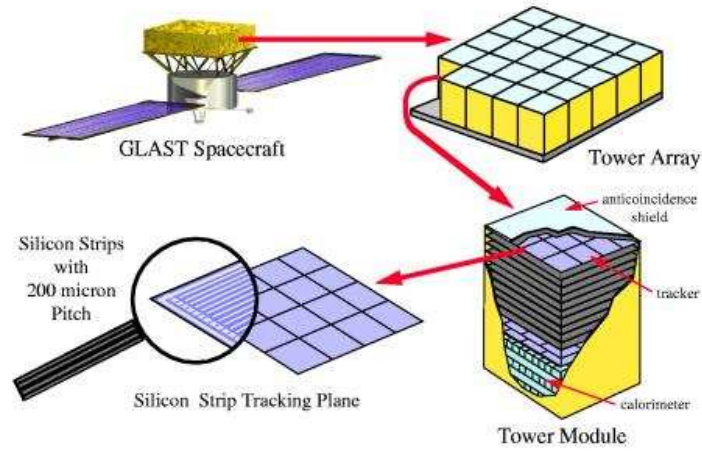
Figure 2.5:   Artist's illustration of the *GLAST* instrument and spacecraft.
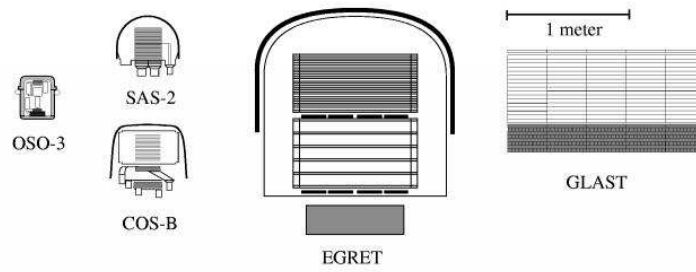
Figure 2.6:   Schematic diagrams of the *SAS-2*, *COS-B*, *EGRET*, and *GLAST* instruments, to scale.

silicon strip detectors, with a strip pitch of 200 μm, provide a much more accurate measurement of the particle tracks than did the spark chambers, resulting in a significantly improved point spread function. The use of these detectors also eliminates the need for the gas used in a spark chamber, as well as the need for high voltages on the instrument, both of which are difficult to deal with on board a spacecraft. The partition of the calorimeter into 2.75 cm wide logs, in alternating directions, permits particles to be tracked in the calorimeter as well. This will permit the study of γ-rays which convert in the calorimeter, and thus greatly increase the sensitive area at high energies.

GLAST will have an on axis sensitive area of approximately 6000 cm^2 at 100 MeV, over seven times the sensitive area of *EGRET*. This factor of improvement increases significantly at higher and lower energies: *GLAST* will be have an energy range from approximately 20 MeV to several hundred GeV. The point spread function (PSF) at low energies will be less than half as wide as the *EGRET* PSF , and at high energies less than one sixth as wide. Similarly, the energy resolution will be improved by a factor of two. As significant as these improvements is the much wider field of view, with more than 5 times the solid angle coverage of *EGRET*.

The combination of these improvements will certainly revolutionize the field of γ-ray astronomy. *GLAST* will detect several thousand AGN [103], and with its large sky coverage can monitor them for flares. *GLAST* will also detect many new γ-ray pulsars, while the much improved high energy performance will permit exciting new studies of the Crab, Vela, and Geminga pulsars. Perhaps most exciting are the new classes of sources which *GLAST* will see: with its smaller point spread function, *GLAST* will be able to see some of the structure of extended sources, and will be able to pinpoint the locations of the *EGRET* unidentified sources, enabling their identification with sources at other wavelengths.

Chapter 3

Likelihood Analysis of *EGRET* and *GLAST* data

3.1 Principles of Likelihood Analysis

The use of the likelihood function in data analysis extends back through the work of Bayes [6] in 1763, while extensive development of the Maximum Likelihood statistic began with Fisher [34] in 1921. Detailed explanations of both the Bayesian and Frequentist uses of likelihood can be found elsewhere [55, 24], and there will not be an attempt to detail the myriad results here. Rather there will a small introduction, suitable for understanding the other results presented here.

In most places in this thesis, the Maximum Likelihood statistic is used, rather than a Bayesian analysis. This is generally because it is easier computationally to maximize a function of many variables than to integrate it. In addition, the use of a flat prior (which a Bayesian would claim is implicit in the use of Maximum Likelihood) seems reasonable for the analysis in question.

3.1.1   The Likelihood Function

Given a data set D and a parametrized model $M(\mathbf{x})$, the likelihood of the model is simply the probability of obtaining the data set if the model is true:

$$\mathcal{L}(M(\mathbf{x})) = P(D|M(\mathbf{x})).$$

In general, the value of the likelihood itself is not meaningful, but the ratio of two likelihood values does have meaning, and can be used to determine which of the two models is more likely to be correct.

Thus the value of $\mathbf{x}$ which maximizes the likelihood function is taken to be the estimate of the true value, and the more quickly the likelihood function falls off from this maximum, the smaller the confidence regions will be.

It is typical in Maximum Likelihood work to use logarithms of the likelihoods, which renders some of the computations easier and makes them less prone to numerical error. Thus we have the log likelihood ratio for comparison of two models:

$$\ln \mathcal{L}\left(M_1\right) - \ln \mathcal{L}\left(M_2\right).$$

When evaluating methods of estimation, the important properties of the calculated estimate of a parameter (or "estimator") are

- *Consistency*– That the estimator converges to the true value as more data are accumulated.

- *Efficiency*– The rate at which the estimator converges to the true value. If this is equal to the Rao-Cramèr-Frechet bound (the maximum rate of convergence), the estimator is said to be *efficient* [24].

- *Bias*– The expectation of the difference of the estimator and the true value.

- *Robustness*– The insensitivity of the estimator to errors in the assumed probability distributions (such as noise).

It can be proved [55] that if a consistent, efficient estimator exists, then the Maximum Likelihood estimate is both consistent and efficient. The Maximum Likelihood estimate may be biased, however, and its robustness depends on the models used. If the estimate is biased, an unbiased estimator can be constructed from the Maximum Likelihood estimate; however, the unbiased estimate is not efficient.

3.1.2 Confidence Regions

An easy way of determining a confidence region for the model parameter $\mathbf{x}$ is given in Eadie [24]. We begin by noting the distribution function of $\chi^2(N)$ (where N is the number of "degrees of freedom"):

$$f_{\chi^2(N)}(x) = \frac{\left(\frac{x}{2}\right)^{\left(\frac{N}{2}\right)-1} e^{-\frac{x}{2}}}{2\Gamma\left(\frac{N}{2}\right)},$$

and defining $\chi^2_\alpha(N)$ through

$$\alpha = \int_0^{\chi^2_\alpha(N)} f_{\chi^2(N)}(x)dx,$$

where $0 \leq \alpha \leq 1$.

This function is used to define an α–confidence region, or that region which has probability α of containing the true value:

> *The α–confidence region is the locus of values of* $\mathbf{x}$ *where* $2\ln\mathcal{L}(M(\mathbf{x}))$ *is within* $\chi^2_\alpha(k)$ *of the maximum likelihood value, where k is the number of parameters (the dimensionality of* $\mathbf{x}$*).*

Strictly speaking, the above definition of the confidence region is an approximation, true as the amount of data becomes large. For small data sets, Eadie, et al. [24] provide corrections to this interval. There are other confidence regions which can be defined (see §5.2.2), but this procedure provides the smallest possible region.

3.1.3   Wilks' Theorem

An equivalent statement, known as Wilks' theorem [102, 15, 24] is:

> *If the model $M(\mathbf{x_0})$ (termed the Null model) is correct, and the maximum likelihood value obtained by allowing the k parameters of $\mathbf{x}$ to vary is $\mathcal{L}(\mathbf{x}_M)$, then the statistic*

$$C = 2\left[\ln \mathcal{L}(M(\mathbf{x}_M)) - \ln \mathcal{L}(M(\mathbf{x}_0))\right]$$

> *is asymptotically distributed like $\chi^2(k)$ as the size of the data set increases.*

There is an important caveat, however. The proof of this theorem requires the inverse of the matrix $\left(\frac{\partial^2 \ln \mathcal{L}(\mathbf{x})}{\partial x_i \partial x_j}\right)_{\mathbf{x}=\mathbf{x_0}}$, which may be singular (e.g. if $\frac{\partial \mathcal{L}(\mathbf{x})}{\partial x_i} = 0$ for some parameter x_i). Thus there are cases where an alternate distribution for the maximum likelihood ratio must be found (c.f. chapter 6).

3.2   Calculations of Likelihood

Likelihood analysis has been used for analysis of γ-ray data for both the *EGRET*, *COMPTEL*, and *COS-B* instruments [63, 86, 79], as well as X-ray instruments like the *Einstein* observatory [78]. Binned data has typically been used, and models (often quite elaborate) of the non-source background have been constructed. This section examines the computations of likelihood which are used in such analysis, and develops some mathematical tools which can be used to investigate the capabilities of such analyses.

3.2.1   Unbinned Likelihood

The model predicts a rate of γ-rays as a function of direction (galactic longitude and latitude, or ℓ and b), energy (E), and time (t): $R(\ell, b, E, t)$. If we construct bins of size $d\ell \times db \times dE \times dt$, where each bin is sufficiently small, the rate will be roughly constant across each bin, and there the chance of getting more than one photon in a

bin can be made arbitrarily small. Using the properties of the Poisson distribution, we can calculate the likelihood of getting a photon in a bin:

$$P_1 = R(\ell, b, E, t) \, d\ell \, db \, dE \, dt \times e^{-R(\ell,b,E,t) \, d\ell \, db \, dE \, dt},$$

and the likelihood of not getting a photon in a bin:

$$P_0 = e^{-R(\ell,b,E,t) \, d\ell \, db \, dE \, dt}.$$

If we write the set of bins with a photon as P, and the set with no photons as Q, we can write the likelihood of the entire data set as

$$
\begin{aligned}
\mathcal{L}(R) &= \prod_{i \in P} R(\ell_i, b_i, E_i, t_i) \, d\ell \, db \, dE \, dt \, e^{-R(\ell_i,b_i,E_i,t_i) \, d\ell \, db \, dE \, dt} \\
&\times \prod_{i \in Q} e^{-R(\ell_i,b_i,E_i,t_i) \, d\ell \, db \, dE \, dt} \\
&= \prod_{i \in P} R(\ell_i, b_i, E_i, t_i) \, d\ell \, db \, dE \, dt \times \prod_{i \in P,Q} e^{-R(\ell_i,b_i,E_i,t_i) \, d\ell \, db \, dE \, dt}.
\end{aligned}
\tag{3.1}
$$

Taking the logarithm of both sides, letting sums become integrals where appropriate, and writing the number of photons as N, we have

$$
\begin{aligned}
\ln \mathcal{L}(R) &= \sum_{i \in P} \ln R(\ell, b, E, t) + \sum_{i \in P} \ln(d\ell \, db \, dE \, dt) \\
&- \sum_{i \in P,Q} R(\ell_i, b_i, E_i, t_i) \, d\ell \, db \, dE \, dt \\
&= \sum_{i \in P} \ln R(\ell_i, b_i, E_i, t_i) + \left[\ln\left(d\ell \, db \, dE \, dt\right)\right]^N \\
&- \int R(\ell, b, E, t) \, d\ell \, db \, dE \, dt.
\end{aligned}
\tag{3.2}
$$

The second term in equation (3.2) is independent of the model parameters: it depends only on the data. It will drop out when we calculate likelihood ratios or look for the maximum likelihood model. Thus we may discard it and write simply

$$\ln \mathcal{L}(R) = \sum_{i \in P} \ln R(\ell_i, b_i, E_i, t_i) - \int R(\ell, b, E, t) \, d\ell \, db \, dE \, dt. \tag{3.3}$$

The integral term in equation (3.3) is just the total number of photons predicted by the model, which we can write as N_{pred}. We are left with

$$\ln \mathcal{L}(R) = \sum_{i=1}^{N} \ln R(\ell_i, b_i, E_i, t_i) - N_{\mathrm{pred}}, \tag{3.4}$$

where ℓ_i, b_i, E_i, and t_i denote the position, energy, and time of the i'th photon.

The computation time needed to evaluate $\ln \mathcal{L}$ for a model is dominated by the calculation of R, and will thus scale linearly with the number of photons detected. In general, a fixed amount of time will also be required to calculate N_{pred} for a given model as well.

3.2.2   Binned Likelihood

If we do not make the bins of the previous section infinitesimal, we must integrate to find the rate in each bin:

$$r_j = \int_{\mathrm{bin}\, j} R(\ell, b, E, t)\, d\ell\, db\, dE\, dt.$$

Using the Poisson distribution

$$P(n, \mu) = \frac{e^{-\mu}\mu^n}{n!}$$

as the probability of observing n counts when the rate is μ, we can write the likelihood

$$\mathcal{L} = \prod_{j} \frac{e^{-r_j} r_j^{n_j}}{n_j!}, \tag{3.5}$$

where n_j is the number of photons in bin j.

Taking the logarithm, we have

$$\ln \mathcal{L} = \sum_{j} -r_j + n_j \ln r_j - \ln n_j!.$$

As in the previous section, we may omit the last term, as it is model independent,

and note that the first term is the total number of counts predicted:

$$\ln \mathcal{L} = \sum_j n_j \ln r_j - N_{\text{pred}}.$$ (3.6)

This result is quite similar to the unbinned result. In fact, if we sum over counts, rather than bins, the only difference is the replacement of $\ln R(\ell_i, b_i, E_i, t_i)$ in equation (3.4) with $\ln r_i$ in equation (3.6), where r_i is the rate in the bin containing photon i. Thus the difference is in replacing the modeled rate for the exact direction, energy, and time of each photon with the integrated rate over the bin where the photon was detected.

The computational cost here scales with the total number of bins, unless n_i is generally zero (which reduces to the unbinned case of scaling with N). Thus this calculation can be significantly faster than the unbinned computation in equation (3.4), albeit at the cost of lost information. We will return the comparison of unbinned and binned likelihood in §3.4, but first we must develop some of the machinery necessary for such a comparison. The reader interested in applying this machinery, but who dislikes gory math, is invited to skip from the motivation (equation (3.7)) to the result (equation (3.12)).

3.2.3 Expectation Value of the Likelihood Ratio

It is useful to be able to calculate the expected value of the likelihood ratio of different models, in order to calculate the power of the likelihood ratio test. We can do this by noting that the probability of a data set is given by the likelihood function itself. Thus, if the model M_{T} is true, the average log likelihood ratio of two models M_1 and M_2 is given by the sum over all possible data sets D

$$\langle \Delta \ln \mathcal{L}(M) \rangle = \sum_D \mathcal{L}(D|M_{\text{T}}) \left[\ln \mathcal{L}(D|M_1) - \ln \mathcal{L}(D|M_2) \right]$$ (3.7)

Let us write the data set as a collection of N vectors, $\mathbf{x}_i$, each of which represents an observed photon. The components of each vector will thus be the observed direction, observed energy, and time of detection. We can write the true model prediction

of the rate of photons with observed values $\mathbf{x}$ as $N_{\mathrm{T}} R_{\mathrm{T}}(\mathbf{x})\, d\mathbf{x}$, where $R_{\mathrm{T}}(\mathbf{x})$ is normalized such that $\int R_{\mathrm{T}}(\mathbf{x})\, d\mathbf{x} = 1$. Similarly, we can write the predictions of M_1 and M_2 as $N_1 R_1(\mathbf{x})$ and $N_2 R_2(\mathbf{x})$. The probability of observing a given data set is then

$$\mathcal{L}(\{N, \mathbf{x}\}\,|M) = \frac{e^{-N_{\mathrm{T}}} N_{\mathrm{T}}^N}{N!} \prod_{i=1}^{N} R(\mathbf{x}_i)\, d\mathbf{x}_i, \tag{3.8}$$

and we can verify that it is appropriately normalized

$$
\begin{aligned}
\int_{\{N,\mathbf{x}\}} \mathcal{L}(\{N, \mathbf{x}\}\,|M_{\mathrm{T}}) &= \sum_{N=0}^{\infty} \int d\mathbf{x}_1 \int d\mathbf{x}_2 \ldots \int d\mathbf{x}_N \frac{e^{-N_{\mathrm{T}}} N_{\mathrm{T}}^N}{N!} \prod_{i=1}^{N} R_{\mathrm{T}}(\mathbf{x}_i) \\
&= 1.
\end{aligned}
$$

The average log likelihood of data sets with N photons is then

$$
\begin{aligned}
\langle \Delta \ln \mathcal{L}(\{\mathbf{x}\}\,|M) \rangle &= \sum_{N=0}^{\infty} \int d\mathbf{x}_1 \int d\mathbf{x}_2 \ldots \int d\mathbf{x}_N \frac{e^{-N_{\mathrm{T}}} N_{\mathrm{T}}^N}{N!} \prod_{i=1}^{N} R_{\mathrm{T}}(\mathbf{x}_i) \times \\
&\quad \left[\left(\sum_{i=1}^{N} \ln N_1 R_1(\mathbf{x}_i)\, d\mathbf{x}_i - N_1 \right) - \left(\sum_{i=1}^{N} \ln N_2 R_2(\mathbf{x}_i)\, d\mathbf{x}_i - N_2 \right) \right] \\
&= \left[\sum_{N=0}^{\infty} \int d\mathbf{x}_1 \ldots \int d\mathbf{x}_N \frac{e^{-N_{\mathrm{T}}} N_{\mathrm{T}}^N}{N!} \prod_{i=1}^{N} R_{\mathrm{T}}(\mathbf{x}_i) \sum_{i=1}^{N} \ln \frac{N_1 R_1(\mathbf{x}_i)}{N_2 R_2(\mathbf{x}_i)} \right] \\
&\quad + N_2 - N_1
\end{aligned}
\tag{3.9}
$$

The normalization of R_{T} allows us to note that

$$
\int \prod_i R_{\mathrm{T}}(\mathbf{x}_i) \ln R_1(\mathbf{x}_j)\, d\mathbf{x}_k =
\begin{cases}
\prod\limits_{i \neq k} R_{\mathrm{T}}(\mathbf{x}_i) \ln N_1 R_1(\mathbf{x}_j) & j \neq k \\
\prod\limits_{i \neq k} R_{\mathrm{T}}(\mathbf{x}_i) \int R_{\mathrm{T}}(\mathbf{y}) \ln N_1 R_1(\mathbf{y})\, d\mathbf{y} & j = k
\end{cases}
, \tag{3.10}
$$

and thus equation (3.9) simplifies to

$$
\begin{aligned}
\langle \Delta \ln \mathcal{L}(\{\mathbf{x}\}\,|M) \rangle &= \sum_{N=0}^{\infty} \frac{e^{-N_{\mathrm{T}}} N_{\mathrm{T}}^N}{N!} \sum_{i=1}^{N} \int d\mathbf{y}\, R_{\mathrm{T}}(\mathbf{y}) \ln \frac{N_1 R_1(\mathbf{y})}{N_2 R_2(\mathbf{y})} + N_2 - N_1 \\
&= \sum_{N=0}^{\infty} \frac{e^{-N_{\mathrm{T}}} N_{\mathrm{T}}^N}{N!} N \int d\mathbf{y}\, R_{\mathrm{T}}(\mathbf{y}) \ln \frac{N_1 R_1(\mathbf{y})}{N_2 R_2(\mathbf{y})} + N_2 - N_1
\end{aligned}
$$

$$
\begin{aligned}
&= \sum_{N=1}^{\infty} \frac{e^{-N_{\mathrm{T}}} N_{\mathrm{T}}^{N-1}}{(N-1)!} N_T \int d\mathbf{y}\, R_{\mathrm{T}}(\mathbf{y}) \ln \frac{N_1 R_1(\mathbf{y})}{N_2 R_2(\mathbf{y})} + N_2 - N_1 \\
&= N_T \int d\mathbf{y}\, R_{\mathrm{T}}(\mathbf{y}) \left(\ln R_1(\mathbf{y}) - \ln R_2(\mathbf{y}) \right) \\
&\quad + N_T \ln N_1 - N_T \ln N_2 + N_2 - N_1 \quad\quad\quad (3.11)
\end{aligned}
$$

When we are discussing models which are maximum likelihood models, a further simplification can usually be made. If we write the model parameters as $\{\theta, N_{\mathrm{pred}}\}$, so that our normalized $R = R(\theta)$, the conditions of maximum likelihood will generally be

$$
\frac{\partial \ln \mathcal{L}(M(\theta, N_{\mathrm{pred}}))}{\partial \theta_k} = 0 \;,\; \frac{\partial \ln \mathcal{L}(M(\theta, N_{\mathrm{pred}}))}{\partial N_{\mathrm{pred}}} = 0.
$$

Writing the second condition in full, we see

$$
\begin{aligned}
0 &= \frac{\partial}{\partial N_{\mathrm{pred}}} \sum_{i=1}^{N} \ln N_{\mathrm{pred}} R(\mathbf{x}_i) - N_{\mathrm{pred}} \\
&= \frac{\partial}{\partial N_{\mathrm{pred}}} \left[\sum_{i=1}^{N} \ln N_{\mathrm{pred}} + \sum_{i=1}^{N} \ln R(\mathbf{x}_i) - N_{\mathrm{pred}} \right] \\
&= \frac{\partial}{\partial N_{\mathrm{pred}}} \left[N \ln N_{\mathrm{pred}} + \sum_{i=1}^{N} \ln R(\mathbf{x}_i) - N_{\mathrm{pred}} \right] \\
&= \frac{N}{N_{\mathrm{pred}}} - 1,
\end{aligned}
$$

or $N = N_{\mathrm{pred}}$.

This will not be true if constraints on model parameters are enforced (i.e. if a source flux is required to be non-negative, and the unconstrained maximum likelihood model would have a negative source flux). Usually, however, such constraints are not applicable, and equation (3.11) reduces to

$$
\langle \Delta \ln \mathcal{L}(\{\mathbf{x}\}\,|M) \rangle_{\mathbf{x}} = N_T \int d\mathbf{y}\, R_{\mathrm{T}}(\mathbf{y}) \left(\ln R_1(\mathbf{y}) - \ln R_2(\mathbf{y}) \right) \quad\quad (3.12)
$$

This rather simple result can be used to calculate how much our test statistic will decrease if a binned model is used rather than an unbinned model (§3.4), the optimal

sizes for bins, and (with some extensions) the threshold intensity for the detection of a source (§4.2).

3.3   Models Used for Likelihood Analysis

3.3.1   An "Exact" Model

The models for which we calculate likelihoods must give probabilities of a given data set being seen. Thus, the models must include both the astrophysical reality (that there is a point source with a certain flux at a certain location) and the instrument response to the incoming γ-rays.

The instrument response to an incoming gamma ray can be characterized rather simply: for a given incoming photon direction and energy (ℓ_0, b_0, E_0), we want to know the probability of a detected direction and energy (ℓ, b, E). This will be a function of the state and orientation of the instrument (I), and so we can write this as $P(\ell, b, E | \ell_0, b_0, E_0, I(t))$.

There are three principal sources of astrophysical gamma rays. There are point sources, which typically have a power law energy spectrum, perhaps with a spectral break at high energy, and which may exhibit time variability on millisecond time scales. There is galactic diffuse emission due to interaction of high energy cosmic rays with the diffuse gas in our galaxy. This has a spatial form which can be estimated from radio maps of the galactic gas, and the spectrum over the *EGRET* energy range can be approximated as a power law with index of $\alpha_M \approx -2.1$ [45]. Finally, there is a diffuse extra-galactic background, probably due to unresolved AGN [89, 103], which is isotropic and has a power law index $\alpha_B \approx -2.22$. We will assume that both diffuse backgrounds are time independent.

We can write an N source model, then, as being the sum of these three components:

$$P(\ell_0, b_0, E_0 | t) = \sum_{i=1}^{N} S_i(E_0, t)\, \delta(\ell_0 - \ell_i)\, \delta(b_0 - b_i) + G_{\mathrm{M}} M(\ell_0, b_0) E_0^{-\alpha_m} + G_{\mathrm{B}} E_0^{-\alpha_B},$$

and combine it with the instrument response function to find the probability of detecting a photon with a measured position and energy:

$$
\begin{aligned}
P(\ell, b, E|t) &= \int d\ell_0 \int db_0 \int dE_0 \, P(\ell_0, b_0, E_0|t) P(\ell, b, E|\ell_0, b_0, E_0, I(t)) \\
&= \int dE_0 \sum_{i=1}^{N} S_i(E_0, t) P(\ell, b, E|\ell_i, b_i, E_0, I(t)) \\
&\quad + \int d\ell_0 \int db_0 \int dE_0 \left[G_{\mathrm{M}} M(b_0, E_0) E_0^{-\alpha_M} + G_{\mathrm{B}} E_0^{-\alpha_B} \right] \\
&\quad \cdot P(\ell, b, E|\ell_0, b_0, E_0, I(t)).
\end{aligned}
\tag{3.13}
$$

It is impractical to evaluate equation (3.13) as written, for several reasons. Evaluation of the triple integral term for all necessary positions, energies, and times is computationally infeasible. In addition, it is impractical to measure the instrument response function adequately as a function of so many parameters.

3.3.2 A Calculable Model

The first simplifying assumption is that the instrument response is separable into three different functions:

$$
\begin{aligned}
P(\ell, b, E|\ell_0, b_0, E_0, I(t)) &= SA(\ell_0, b_0, E_0, I(t)) \times PSF(\ell, b|\ell_0, b_0, E_0, I(t)) \\
&\quad \times ED(E|\ell_0, b_0, E_0, I(t)),
\end{aligned}
\tag{3.14}
$$

where SA is the sensitive area of the instrument, PSF is the normalized point spread function, and ED is the normalized energy dispersion function.

If the spectral index of the source is known in advance, the PSF and SA can be "pre-dispersed". To do this, we construct $\widetilde{PSF}$ and $\widetilde{SA}$ such that

$$
\begin{aligned}
\widetilde{SA}(\ell_0, b_0, E, I(t)) \widetilde{PSF}&(\ell, b|\ell_0, b_0, E, I(t)) E^{-\alpha} = \\
\int dE_0 \, [SA(\ell_0, b_0, E_0, I(t)) &\times PSF(\ell, b|\ell_0, b_0, E_0, I(t)) \times \\
& ED(E|\ell_0, b_0, E_0, I(t)) E_0^{-\alpha}].
\end{aligned}
\tag{3.15}
$$

This can be done by the definitions

$$\widetilde{SA}(\ell_0, b_0, E, I(t)) = \frac{\int dE_0 SA(\ell_0, b_0, E_0, I(t)) \times ED(E|\ell_0, b_0, E_0, I(t)) E_0^{-\alpha}}{E^{-\alpha}} \quad (3.16)$$

and

$$\widetilde{PSF}(\ell_0, b_0, E, I(t)) = \frac{P(\ell, b, E|\ell_0, b_0, E_0, I(t)) E_0^{-\alpha}}{\widetilde{SA}(\ell_0, b_0, E, I(t)) E^{-\alpha}} \quad (3.17)$$

Calculations using $\widetilde{SA}$ and $\widetilde{PSF}$ can be performed as if there were no energy dispersion (and using measured rather than true energy). It should be remembered, however, that the spectral index of the γ-rays was assumed in the construction of these functions.

The next simplification is the pre-calculation of the convolution integral in equation (3.13). Because our background model $M(\ell_0, b_0)$ is fixed, the integrals

$$\begin{aligned}\tilde{M}(\ell, b, E, I(t)) &= \int d\ell_0 \int db_0 \int dE_0\, M(b_0, E_0) E_0^{-\alpha_M} SA(\ell_0, b_0, E_0, I(t)) \\ &\times PSF(\ell, b|\ell_0, b_0, E_0, I(t)) ED(E|\ell_0, b_0, E_0, I(t)) \end{aligned} \quad (3.18)$$

and

$$\begin{aligned}\tilde{B}(\ell, b, E, I(t)) &= \int d\ell_0 \int db_0 \int dE_0\, E_0^{-\alpha_B} SA(\ell_0, b_0, E_0, I(t)) \\ &\times PSF(\ell, b|\ell_0, b_0, E_0, I(t)) ED(E|\ell_0, b_0, E_0, I(t)) \end{aligned} \quad (3.19)$$

can be precalculated.

This is a lot of data to precalculate, however. It is usual for *EGRET* analysis to use $0.5° \times 0.5°$ bins, about 25,000 of which are needed for the for the full field of view. The energy variation is obtained by interpolation between 20 measured points. Thus, to calculate this for 78 instrument modes would require the integrals to be evaluated over 30 million times. These calculations would need to be redone whenever the pointing of the instrument changed.

By averaging over the instrument modes, and by assuming that the convolved energy spectrum is still a power law with index ≈ 2, the calculations may be sped up considerably. If the instrument response is averaged over the incident photon

direction as well, the calculations do not have to be redone for the different instrument pointings: the computations can be performed once and stored for future use.

3.3.3 `LIKE` Model

The `LIKE` program [63] performs a likelihood analysis in one energy band, using the average instrument parameters for that band, and the counts and exposure maps which are the standard *EGRET* data products. Thus, it is a binned analysis using one energy bin, and spatial bins of $0.5° \times 0.5°$ in ℓ and b.

The `LIKE` program can be used to analyze several different energy bands sequentially. This is then equivalent to having multiple energy bins, but with the caveat that source and background fluxes are allowed to vary independently in the different bins.

The source and null models used by `LIKE` generally have other known sources included at fixed positions (the same position in both models), with the source model having one additional source at a trial location. The comparison of two models which have multiple sources differing between them must be done by hand. Thus a "two vs. one" test, comparing a model with one source to a model with the same source split into two sources, is difficult to perform.

3.3.4 `unlike` Model

Although it would be desirable to perform an unbinned analysis on the *EGRET* data, the computational difficulties shown in §3.3.2 make it impractical. In addition, the two quantities in equation (3.4) can both become very large. The fact that we are differencing these two large numbers to get the log likelihood and then differencing two log likelihoods to get the log likelihood ratio means that very small errors can cause large changes in the test statistic. Although similar concerns exist for the binned case, in practice there are fewer problems, since the differencing can be done for each bin, rather than after the sum in equation (3.6).

Thus, the `unlike` program uses a binned model, but incorporates more flexibility than does `LIKE`. It will simultaneously analyze several different maps (using the same

model), and so allows multiple energy bins in a more natural way than does `LIKE`, which analyzes only one map at a time. Because of this, the flux of a source is not correlated between different `LIKE` maps, while in `unlike` either correlated or uncorrelated fluxes can be used. The maps in `unlike` can have different spatial bin sizes, so that high energy maps are binned on a finer scale than low energy. The models assume a power law spectrum for the backgrounds, and allow either a power law or an arbitrary spectrum for the sources.

The `unlike` program is, however, not fully developed, and is thus not suitable for everyday analysis purposes. Because the benefit gained by using multiple energy bins is smaller for *EGRET* data than *GLAST* data (see §3.4.1), it did not seem worthwhile to produce a robust, user-friendly program. The principal use of `unlike` to date was for the generation of the likelihood curves used in the variability analysis in Chapter 8. The code is available from the author at `http://razzle.stanford.edu/~billt`.

Because of the *GLAST* instrument's scanning mode, new analysis programs will have to be developed. It is hoped that such programs can benefit from concepts used in the `unlike` analysis system, particularly the simultaneous analysis of multiple energy bins, and the inclusion of multiple sources in a model.

3.3.5   Future Development

Nothing so far has been said of different classes of events, either due to different instrument modes, or to varying quality of the events themselves. Such modes, and any other experimentally determinable quality parameters, can and should be added into the above analysis. This is accomplished by letting our rate R be a function of these quantities as well as the photon direction, energy, and time.

In *EGRET*, there are 78 different triggering configurations of the instrument, and the sensitive area, energy dispersion, and point spread function were measured for each [98]. Events were also classified as Class A, Class B, or Class C events, depending on the quality of the electron tracks. For all practical analysis purposes, however, the rate was averaged over these parameters when finding the likelihood function. This

averaging lost little information, however, since quantities like the PSF did not very dramatically from class to class or mode to mode.

In *GLAST*, it is conceivable that the events should be separated into separate categories for the purposes of analysis. For example, at high energies, the PSF might depend dramatically on the point of conversion in the tracker. Especially if events which did not convert in the tracker at all (calorimeter-only events) are included in the analysis, the events should be binned by separating them into classes which have similar PSF's. Calculations like those shown in §3.4 can help determine when such a separation of events into multiple classes will be worthwhile.

3.4 Quantitative Comparison of Methods

We will now calculate how much information is being lost in the binning process, using the results of §3.2.3. We will take the situation of a source on a flat background, where each has some spectral index (α_S and α_B). The source will be at ($\theta = 0, \phi = 0$), and we will only use data with $\theta < R_{\text{anal}}$ and $E_{\text{min}} < E_{\text{meas}} < E_{\text{max}}$. This corresponds to the usual case in *EGRET* analysis: cuts are made based on the measured energy, and only photons within a fixed radius of the source position are used (to speed the analysis, and allow for backgrounds which differ as a function of sky position). First let us write the rate from the source and from the background independently. The unnormalized source rate will be

$$K_{\text{S}}(\theta, \phi, E) \, d\theta \, d\phi \, dE = \int dE_0 \, ED(E, E_0) PSF(\theta, E_0) \, SA(E_0) \, E_0^{-\alpha_\text{S}} \, d\theta \, d\phi \, dE, \quad (3.20)$$

where E_0 is the true energy and E is the measured energy. The normalized source rate will be

$$R_{\text{S}}(\theta, \phi, E) = \frac{K_{\text{S}}(\theta, \phi, E)}{\int_0^{R_{\text{anal}}} d\theta \int_0^{2\pi} d\phi \int_{E_{\text{min}}}^{E_{\text{max}}} dE \, K_{\text{S}}(\theta, \phi, E) \sin \theta}. \quad (3.21)$$

Similarly, the unnormalized background rate will be

$$K_B(\theta, \phi, E) \, d\theta \, d\phi \, dE = \int dE_0 \, ED(E, E_0) SA(E_0) \, E_0^{-\alpha_B} \, d\theta \, d\phi \, dE \qquad (3.22)$$

leading to a normalized rate of

$$R_B(\theta, \phi, E) = \frac{K_B(\theta, \phi, E)}{\int_0^{R_{anal}} d\theta \int_0^{2\pi} d\phi \int_{E_{min}}^{E_{max}} dE \, K_B(\theta, \phi, E) \sin \theta}. \qquad (3.23)$$

Then if a fraction f of the photons are from the source, we have

$$R(\theta, \phi, E) = f R_S(\theta, \phi, E) + (1 - f) R_B(\theta, \phi, E) \qquad (3.24)$$

For a binned model, the rate will be piecewise constant, where the constant value in each bin is the average of the unbinned rate over that bin:

$$R_{bin\,i}(\theta, \phi, E) = \int_{\theta_{min_i}}^{\theta_{max_i}} \int_{\phi_{min_i}}^{\phi_{max_i}} \int_{E_{min_i}}^{E_{max_i}} R(\theta, \phi, E) \qquad (3.25)$$

Application of equation (3.12), with R_T and R_1 equal to the unbinned model and R_2 equal to the binned model, will now yield the expected decrease in the log likelihood ratio when the binned model is used. Similarly, use of two different binned models for R_1 and R_2 can indicate which of two binned models is better, and by how much.

3.4.1   Implications for *GLAST*

The above calculations have been carried out in Mathematica to determine how binning will affect the analysis of *GLAST* data. For the purposes of this analysis, the instrument parameters were taken from the Baseline II instrument (Feb 1998), and both the point spread function and the energy dispersion function were assumed to be Gaussian. Only energy binning was considered: events were considered unbinned in position (equivalent to the use of bins which are small compared to the point spread

function), and the dependence of the point spread function on factors like the incident direction or conversion point was not taken into account.

The integrals in equation (3.25), equation (3.20), and equation (3.12) can be very time consuming, so it was necessary to pre-disperse the point spread function as described in §3.3.2, and approximate $\widetilde{PSF}$ (and the appropriate energy averaged analogue) by interpolation between previously calculated points.

The calculations were performed for models with up to six energy bins, as well as one model with 18 energy bins, to approximate the unbinned case. All results are normalized to the one-bin case, and thus represent the factor of improvement gained by using multiple bins. The model used a source flux of 1×10^{-8} cm^{-2} s$^{-1}(E_{\mathrm{meas}} >$ 100 MeV), with an photon energy spectrum of E^{-2}, and a flat background with flux 5×10^{-5} cm^{-2} s^{-1} sr$^{-1}(E_{\mathrm{meas}} > 100$ MeV) with a similar spectrum. This is equivalent to a source near the *GLAST* threshold in a moderately strong background. For comparison, the same calculations were done for a very bright source, with a source/background flux 1000 times higher.

The two-bin results are shown in Figure 3.1. For a source near threshold, the best division between the energy bins is around 1 GeV, and the test statistic used to measure the significance of the detection ($T_S = 2\Delta \ln \mathcal{L}$) is increased by a factor of seven. In the background dominated situation, T_S is proportional to the source strength. Thus, an sevenfold increase in T_S is equivalent to a sevenfold decrease in the source threshold. For the very bright source, the best division is around 50 MeV, since the source is detectable in even the lowest energy photons.

The results of the other binning systems are given in Table 3.1 and Figure 3.2. As shown there, four or five energy bins are probably adequate for detection analysis. For spectral analysis of sources, of course, more bins would be desirable, particularly at low energies.

Similar calculations for *EGRET* indicate that the benefits from multiple energy bins are much more modest. Because the energy range of *EGRET* is smaller than *GLAST*, and because the point spread function reaches a limiting width at a lower energy for *EGRET*, the gain from using multiple bins ranges from 5%–80%, depending on the source strength. The analysis technique used in the Third *EGRET* Catalog
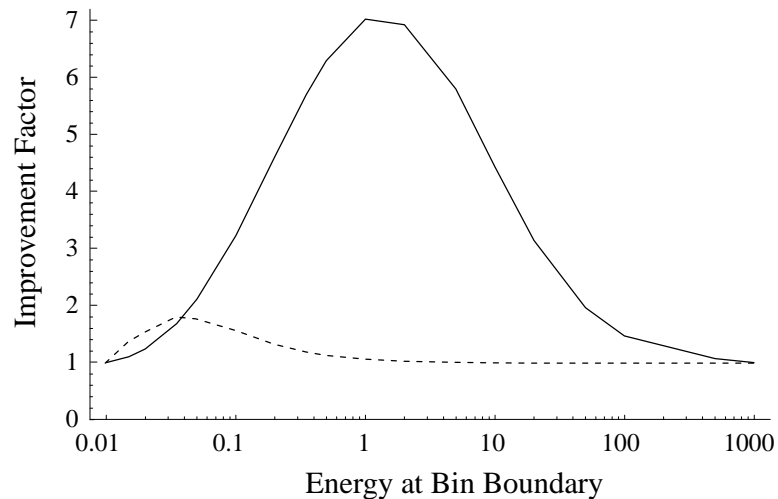
Figure 3.1:   Two-bin analysis of *GLAST* data. The improvement factor reflects the change in $\Delta \ln \mathcal{L}$ vs. the one-bin model. The solid curve is for a source near threshold, the dashed curve is for a very bright source.

Number	Breaks	Improvement
2	1 GeV	7.0
3	500 MeV, 5 GeV	9.1
4	200 MeV, 1 GeV, 5 GeV	10.2
5	200 MeV, 500 MeV, 2 GeV, 10 GeV	10.7
6	100 MeV, 350 MeV, 1 GeV, 2 GeV, 10 GeV	11.0

Table 3.1:   Best energy binning schemes for a fixed number of bins, together with the improvement vs. the one-bin model.
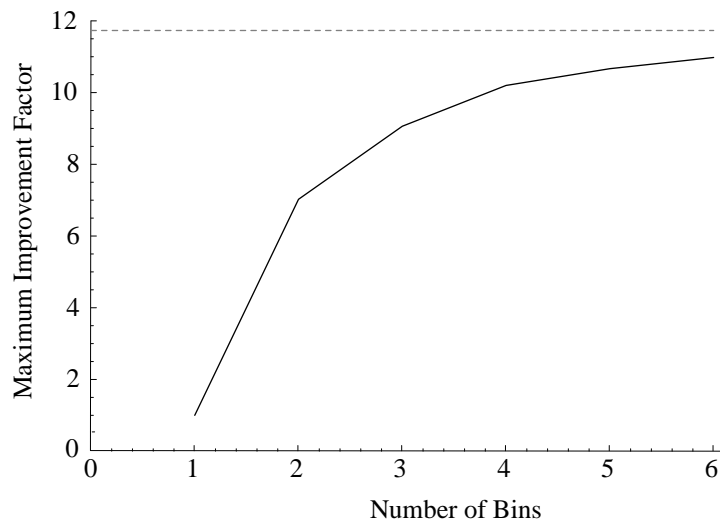
Figure 3.2: The improvement over the one-bin model as a function of number of bins. The horizontal line is the improvement using an unbinned model.

[40] of summing likelihood maps for different energy bands yields results which are nearly as good as a simultaneous fit.

Chapter 4

Thresholds

4.1   Thresholds vs Upper Limits

Before we begin calculating thresholds, it is useful to review the difference between a threshold and an upper limit (see Chapter 5). We can define the α-threshold (for a given observation time, instrument sensitivity, etc...) as that source flux which would result in a detection a fraction α of the time. Note that the threshold does not depend on any observed data. Typically, one uses the 50% threshold, as the average limiting source flux which will be detectable by the instrument.

Upper limits, on the other hand, do depend on the data. Although this definition might not always be meaningful, we would like to define the α-upper limit by saying that the true source flux will be less than the α-upper limit a fraction α of the time. Here, α is typically 90% or 95%: as with confidence regions, one wants to avoid the situation where the true flux is larger than the upper limit. Clearly, an upper limit contains more information than a threshold, since it incorporates the information in the data as well as the models. When a threshold is used in conjunction with data, the only information used from the data is whether or not a source was actually detected. The fact that a source was not detected does not neccesarily mean that the source flux was less than the threshold, since 50% of sources at threshold will not be detected. Because thresholds do not depend on the data, however, they can be

easier to calculate than upper limits, and are useful when discussing the merits and projected results of a proposed mission, like *GLAST*.

4.2   Calculation of Thresholds

One can calculate a threshold by using the results from §3.2.3 to calculate the expected likelihood, given a source strength. By varying that source strength so that the expected likelihood is that required for a detection, one obtains approximately the 50% detection threshold. By calculating the moments of the likelihood distribution, the distribution itself can be found, and other thresholds can be obtained.

The two rates in equation (3.12) in this application will come from the two models under consideration: the model with a source as well as background, and the null model with background only. The background in *EGRET* is modeled as the sum of a gas-map component and a constant, where the intensity of each is fit for any given observation, and the energy spectrum of each* is $\alpha = -2.1$. For simplicity, we will consider first the case where the gasmap is constant as well, and thus there is really only one background component.

We then can use equation (3.12) with the model in equation (3.24). Our null model will have f (the fraction of photons coming from the source) set to 0, while for our source model, it will be set to the fraction of photons within R_{anal} coming from the source. Because $\Delta \ln \mathcal{L}$ (and thus the detection test statistic T_s) is linear with the number of photons, the distribution of T_s for the model with the true source intensity when i photons are observed will be the convolution of i copies of the one photon distribution, which we will call T_s^1. The full distribution will then be the sum of the distributions for $0, 1, 2 \ldots$ photons, each weighted by the Poisson probability of getting that number of photons. The moments of this distribution are easily calculated.

---

*As noted in §3.3, the spectral indices of the two background components are slightly different. Here, for ease of calculation, they are assumed to be equal.

$$
\left\langle T_s^{\text{"true"}} \right\rangle = \sum_{N_T^{\text{obs}}=0}^{\infty} P(N_T^{\text{obs}}) \sum_{i=1}^{N_T^{\text{obs}}} N_T^{\text{obs}} \langle T_s^1 \rangle
$$
$$
= N_T \langle T_s^1 \rangle \tag{4.1}
$$

where $\langle T_s^1 \rangle$ is given by

$$
\begin{aligned}
\langle T_s^1 \rangle &= 4\pi \int_0^{R_{anal}} d\theta \int_{E_{min}}^{E_{max}} dE \; (f R_{\text{S}}(\theta, E) + (1-f) R_{\text{B}}(\theta, E)) \times \\
&\quad [\ln (f R_{\text{S}}(\theta, E) + (1-f) R_{\text{B}}(\theta, E)) - \ln R_{\text{B}}(\theta, E)] \\
&= 4\pi N_T \left[\int_0^{R_{anal}} d\theta \int_{E_{min}}^{E_{max}} dE \; (f R_{\text{S}}(\theta, E) + (1-f) R_{\text{B}}(\theta, E)) \times \right. \\
&\quad \left. \ln \left(\frac{f R_{\text{S}}(\theta, E)}{R_{\text{B}}(\theta, E)} + (1-f) \right) \right] \tag{4.2}
\end{aligned}
$$

The calculations in equation (4.2) are calculable as written, but can be simplified if the spectral index of the source and background are the same:

$$
\begin{aligned}
\langle T_s^1 \rangle &= \frac{4\pi}{\int_{E_{min}}^{E_{max}} dE \; \widetilde{SA}(E) E^{-\alpha}} \left[\int_0^{R_{anal}} d\theta \int_{E_{min}}^{E_{max}} dE \; \widetilde{SA}(E) E^{-\alpha} \times \right. \\
&\quad \left. \left(f \widetilde{PSF}(\theta, E) + \frac{1-f}{A} \right) \ln \left(f A \widetilde{PSF}(\theta, E) + (1-f) \right) \right] \tag{4.3}
\end{aligned}
$$

Similar computations show that

$$
\left\langle (T_s^{\text{"true"}})^2 \right\rangle = N_T \left\langle (T_s^1)^2 \right\rangle + \left(\left\langle (N_T^{\text{obs}})^2 \right\rangle - N_T \right) \left\langle T_s^1 \right\rangle^2 , \tag{4.4}
$$

where

$$
\begin{aligned}
\langle (T_s^1)^2 \rangle &= \frac{8\pi}{\int_{E_{min}}^{E_{max}} dE \; \widetilde{SA}(E) E^{-\alpha}} \left[\int_0^{R_{anal}} d\theta \int_{E_{min}}^{E_{max}} dE \; \widetilde{SA}(E) E^{-\alpha} \times \right. \\
&\quad \left. \left(f \widetilde{PSF}(\theta, E) + \frac{1-f}{A} \right) \left[\ln \left(f A \widetilde{PSF}(\theta, E) + (1-f) \right) \right]^2 \right] \tag{4.5}
\end{aligned}
$$

Because N_T^{obs} has a Poisson distribution, $\left\langle (N_T^{\text{obs}})^2 \right\rangle = N_T(N_T + 1)$, and equation (4.4) becomes

$$\left\langle \left(T_s^{\text{“true”}} \right)^2 \right\rangle \;=\; N_T \left\langle (T_s^1)^2 \right\rangle + N_T^2 \left\langle T_s^1 \right\rangle^2 . \tag{4.6}$$

The variance of $T_s^{\text{“true”}}$ is then

$$
\begin{aligned}
\left\langle (\Delta T_s^{\text{“true”}})^2 \right\rangle \;&=\; \left\langle (T_s^{\text{“true”}})^2 \right\rangle - \left\langle T_s^{\text{“true”}} \right\rangle^2 \\
&=\; N_T \left\langle (T_s^1)^2 \right\rangle
\end{aligned}
\tag{4.7}
$$

4.3   Allowance for Extra Degrees of Freedom

As discussed earlier in §3.1.3, if the parameters of the model are allowed to vary from the true value, the distribution of the change in T_s will be distributed like χ^2, with the number of degrees of freedom equal to the number of parameters which may vary. Because there are 5 parameter in the typical *EGRET* source model (one for source intensity, and two each for source position and background level), and 2 parameters in the null model, we know that $T_S - T_S^{\text{“true”}}$ is distributed like χ_3^2. This results in

$$
\begin{aligned}
\mu_{T_s} \;&=\; \langle T_s \rangle \\
&=\; \left\langle T_s^{\text{“true”}} \right\rangle + 3
\end{aligned}
\tag{4.8}
$$

and

$$
\begin{aligned}
\sigma_{T_s}^2 \;&=\; \left\langle (\Delta T_s)^2 \right\rangle \\
&=\; \left\langle \left(\Delta T_s^{\text{“true”}} \right)^2 \right\rangle + 6.
\end{aligned}
\tag{4.9}
$$

4.3.1   The Full Distribution of T_s

Unfortunately, the distribution of T_s is quite skew, and thus the Gaussian with mean μ_{T_s} and standard deviation σ_{T_s} is not a good approximation to the distribution of T_s. A much better approximation is that $\sqrt{T_s}$ has a Gaussian distribution. The mean

and standard deviation of $\sqrt{T_s}$ can be written in terms of μ_{T_s} and σ_{T_s} (calculated above):

$$\mu_{\sqrt{T_s}} = \sqrt[4]{\mu_{T_s}^2 - \frac{\sigma_{T_s}^2}{2}}, \tag{4.10}$$

and

$$\sigma_{\sqrt{T_s}} = \sqrt{\mu_{T_s} - \mu_{\sqrt{T_s}}^2}. \tag{4.11}$$

The calculation of $\langle T_s^1 \rangle$ and $\langle (T_s^1)^2 \rangle$ must be done numerically because of the form of the point spread function. For *EGRET* sufficiently accurate empirical approximations are:

$$\langle T_s^1 \rangle = 18.556 \left(x^{0.7602} + 1.77 \right)^{-2.63}, \tag{4.12}$$

and

$$\langle (T_s^1)^2 \rangle = 73.424 \left(x^{0.94} + 1.568 \right)^{-2.1277}, \tag{4.13}$$

where $x \equiv B_c/S_c$, $S_c \equiv S \times E$, the expected number of photons received from the source, and $B_c \equiv 214.09 \times B \times E$, the expected number of photons which would be received within $15°$ of the source position if the background were uniform.

Monte Carlo simulations indicate that equation (4.10) and equation (4.11) are accurate to within 5% for flat backgrounds.

The threshold usually desired is the 50% threshold, which will be the source flux necessary to make $\mu_{\sqrt{T_S}} = 4$ (or 5 for $|b| < 10°$). The full distribution of T_S (and thus the probability that a source of a certain strength would be detected) should be useful when analyzing source distributions, as sources which are nominally below threshold do have some chance of being detected (as well as the reverse).

4.3.2 Background Structure

Unfortunately, the presence of background structure can have dramatic effects on the instrumental threshold. It is not feasible to perform the above calculations with every possible shape of background. Rather, the general effects of the varying background

were modelled by multiplying the expected T_S by a compensation factor:

$$C = .37 + .0061 \, |b| \, , \tag{4.14}$$

where b is the galactic latitude in degrees. Although there is significant longitude dependence near the plane, this dependence could not be easily modelled in this way.

The expected T_s from above should be multiplied by this correction factor for a more realistic estimate of the source significance; unfortunately the result is correct only on average, and additional structure of the diffuse emission make it accurate only far from the plane.

For an estimation of the probability that the T_s is greater than a certain level, one must change variables from T_s to $\sqrt{T_s}$, and use equation (4.10) and equation (4.11), multiplying by the compensation factor from equation (4.14)

Thresholds calculated by the above technique may still have significant errors. Pointlike structure in the background can change the expected T_S by up to a factor of 2. Nonetheless, this technique does capture the average behavior of the instrumental threshold, and is a significant improvement to the assumption that the threshold is constant. If desired, accurate determination of the threshold at a given location can be found by repeating the calculation with the appropriate background included.

Chapter 5

Upper Limits

The concept of an upper limit is often ambiguous. The average graph reader might think that the region below a "1σ" upper limit is equivalent to a "1σ" confidence region: implying that there is a 68% chance that the true value is less than the upper limit. Unfortunately, if one sets out to create an upper limit, there is no such value from the frequentist point of view. The various means of calculating something to call an upper limit are discussed below.

The Bayesian analyst has no such problems: the interval estimation done in Bayesian analysis (which does not strictly correspond to a confidence region) is directly applicable to upper limits, that is, situations where the interval includes 0.

To demonstrate the problem with defining a upper limit which is a confidence region, we will begin by reviewing the definition of a confidence region.

5.1   Confidence Regions

According to the frequentist philosophy, one can make no probabilistic statements about the truth of a model. There is a model which is correct, and others which are incorrect: there is no probability about it. This is somewhat different than what one might say in everyday conversation, and thus can lead to some confusion for the statistics student, who might say something like: "There is a 95% chance that this is a a two-headed coin," when faced with a series of all-heads coin flips. Strictly

speaking (according to the frequentist) the coin is either two-headed or not, there is no probability about it. The only probability is that related to the data set: the probability of getting a data set with that many heads in a row might be less than 5%. This is in keeping with Bernoulli's definition of probability, relating the probability of an event to the frequency of that outcome in repeated trials: thus the appellation "frequentist".

How then is a confidence region defined? Well, the first step is to note that the estimate $\hat{x}$ of a model parameter x depends on the data. So we are permitted to make probabilistic statements about $\hat{x}$, if not about x itself. In fact, we can make probabilistic statements about $x - \hat{x}$: again a data-set dependent quantity. If there is a way to calculate C such that $P(|x - \hat{x}| < C) = 95\%$, for any value of x, then the region $[\hat{x} - C, \hat{x} + C]$ will contain the true value 95% of the time (that is, for 95% of the data sets). To deal with non-symmetric confidence regions, one may simply change variables in order to make the confidence region symmetric.

5.1.1   The problem with upper limits

The difficulty with the notion of an upper limit is the requirement that the confidence region contain the true value of the model parameter a fixed fraction of the time, *for any true value of the model parameter*. Because the region which an upper limit defines always includes zero, this region will always contain the true value if the value is zero. And thus, no confidence region can be defined by the upper limit. The possible solutions involve relaxing the requirement that the upper limit be greater than the true value exactly some fraction of the time, or by giving up on the idea of constructing an upper limit, and simply constructing a confidence region.

5.2   Definitions of Upper Limits

Given that it is not possible to define a confidence region which always contains the value zero (as we would like the region bounded by the upper limit to do), it remains to

determine what sort of upper limits one can define and use in a statistically meaningful way.

5.2.1   Statistically Rigorous "Upper Limit"

The way in which one can define a statistically exact upper limit is by constructing the appropriate confidence region, and quoting the top end of the confidence region as the upper limit only if the lower end of the confidence region is less than zero. Because we are dealing with a confidence region, it will contain the true value the stated fraction of the time. But, by the nature of the construction, we are not guaranteed an upper limit. This might not seem to be a problem, but in fact can lead to difficulties.

Constructing the confidence region is done by means of a confidence belt. For each value of the true parameter x_T, a range of the measured parameter x is constructed, such that in a fixed fraction of the data sets, the measured value x will be in that range. This is illustrated in Figure 5.1. For concreteness, let us examine the use of a 95% frequency band.

Figure 5.1:   Construction of confidence regions. The shaded region is formed by picking a true value x_T, then finding an interval in x which will contain the measured value 95% of the time.

The confidence belt is constructed horizontally then (for each value of x_T, a range in x is constructed), but then read out vertically. The justification is simple: for any value of x_T, the probability of a measurement in the shaded region is 95%. Thus, the

probability of a pair (x_T, x) being in the band is also 95%. And thus, for a measured value of x, the probability that the band contains the true value x_T is 95%.

Figure 5.1 shows a standard, symmetric, confidence belt. Reading vertically from a measured value of $x = -1$, an upper limit of slightly less than 1 is obtained. What, though, if a measurement of $x = -3$ is obtained? Certainly this is unlikely, but it will occasionally happen, and one is left with no region at all. One might be tempted to extend the confidence belt to negative values of x_T, resulting in a negative upper limit, but this is meaningless from both a statistical point of view (if a model with $x_\mathrm{T} < 0$ is impossible, it makes no sense to discuss the probability of data sets arising from it), and an analyst's point of view (what does a negative upper limit mean?). The one possibly useful thing about such negative upper limits is if they are combined with the negative point estimate of x_T (the value of x_T with the maximum likelihood) in an effort to rate physically meaningful values of x_T. Better than this approach, however, is to use the likelihood function itself in the physically meaningful range.

5.2.2   The Feldman-Cousins Method

In the 1998 Review of Particle Properties [16], the prefered method listed is that of Feldman and Cousins [27]. This unified approach to the calculation of upper limits and confidence regions is similar to that of §5.2.1, but has the benefit that there are no measured values for which one does not obtain a confidence region.

This is done with confidence regions that look like those in Figure 5.2. By using non-central confidence regions for the lower values of x_T, non-negative confidence regions will be obtained for negative measurements.

There is some difficulty in deciding how to construct the bands for Figure 5.2. Feldman and Cousins present a method for this construction, and apply it to Gaussian and Poisson data. For *EGRET*-style data, the method would be rather complex, but with some simplifications could probably be implemented.

In this way, one can avoid the problem of not being able to construct upper limits which are confidence regions. This problem (that the upper limits always include zero) is avoided because 5% of the time (for our 95% confidence region) when the
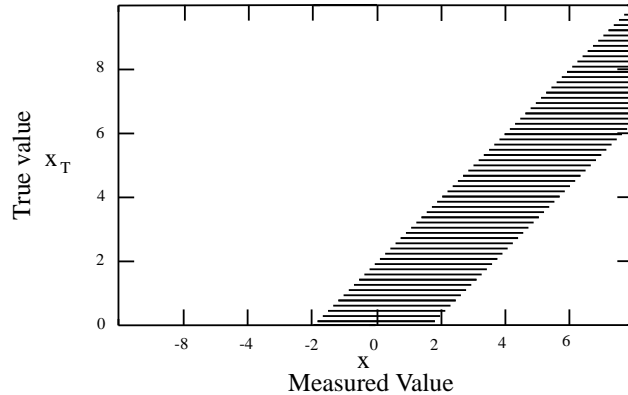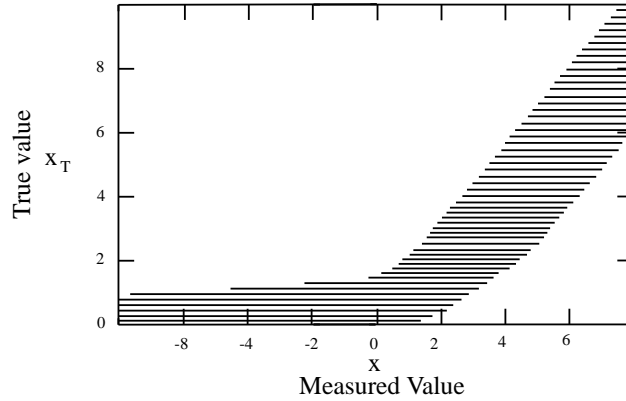
Figure 5.2: Construction of confidence regions. The shaded region is formed by picking a true value x_T, then finding an interval in x which will contain the measured value 95% of the time. If this interval extends to $-\infty$ for some values of x_T, this confidence region will be an upper limit when appropriate.

true flux is zero, we will not have an upper limit. Instead, there will be a positive flux estimate and a confidence region which does not include zero.

The chief problem with this method is that some fraction of the time, one will obtain a confidence region which does not include zero (and is thus not an upper limit). This would not be a problem, except that this will happen even when a source detection is not claimed. For example, suppose that the one trial significance of an intensity measurement is 99.5%. This will not be accepted as a real detection at the 5σ level (standard for *EGRET* analysis near the galactic plane). But the 95% confidence region will not include zero, and thus one cannot claim a 95% upper limit which is statistically rigorous. The solution to this problem is typically to quote the upper end of the 95% confidence region as the upper limit, with the knowledge that it is a conservative upper limit.

5.2.3 The "PDG Method"

Prior to 1998, the Particle Data Group suggested several alternate methods for calculating upper limits to avoid unphysical values[71]. One, with a decidedly Bayesian flavor, was the sole suggestion in early PDG publications [105], and thus has been referred to as the "PDG method", to the consternation of some in the PDG[71].

This method involves renormalizing the likelihood curve so that the integral over the physical region is 1.0. For an upper limit, this corresponds to the requirement

$$\int_0^\infty \mathcal{L}(x)\,dx = 1.$$

The upper limit x_{UL} is then determined by

$$\int_0^{x_{\mathrm{UL}}} \mathcal{L}(x)\,dx = \alpha.$$

This is equivalent to a Bayesian analysis where the prior probability is

$$P(x) = \begin{cases} 1 & x \geq 0 \\ 0 & x < 0 \end{cases}$$

This prior is generally conservative, as there tend to be more dim sources than bright ones (and for most locations, no source at all).

5.2.4   Ad Hoc Methods

Other methods are presented in the 1994 Review of Particle Properties [71] as well. One, which is clearly conservative, is to find the central interval from §5.2.1 (where the confidence belt was extended to negative x_{T}) but to shift the interval so that the point estimate (the value of the parameter with the peak likelihood) is at zero, rather than the non-physical negative value. Because this upper limit is always greater than one which would contain the true value the stated fraction of the time, it is necessarily conservative. This is the method used by LIKE, and thus investigators should be aware of this built-in conservatism in the upper limit.

Another method is to pretend that the likelihood function has a maximum for the zero value of the intensity, and to generate the upper limit by finding where the likelihood has decreased a set amount from this "maximum", just as if it were a true maximum. This is, again, necessarily conservative, because the true maximum likelihood is higher, and thus the upper limit from §5.2.1 must be lower than this one.

As pointed out by Feldman and Cousins [27], the post-hoc choice to calculate an

upper limit rather than a confidence region can bias the results in strange ways. In particular, both overcoverage of the confidence belt (Conservatism) and undercoverage can result.

Chapter 6

Distribution of T_s

As discussed in §3.1.3, the distribution of the maximum log likelihood ratio is generally the χ^2 distribution with some number of degrees of freedom. As noted there, however, there are situations where the proof of this does not hold, and we must look for alternate sources for the distribution. In the case of the maximum *EGRET* test statistic in a patch of sky, Wilks' theorem does not hold: here an alternate distribution for the largest T_s in a survey (given that there are no real sources) is derived.

6.1   An Empirical Distribution

The *EGRET* null model is equivalent to the one–source model where the source intensity has been set to zero; the position of the "source" then does not matter. Then, since $\left[\frac{\partial \mathcal{L}(S,\ell,b)}{\partial \ell}\right]_{S=0} = 0$, the proof of Wilks' theorem breaks down. It is clear by inspection that the theorem cannot hold: the distribution of the largest T_s we see (if there is no source) should depend on how large an area of sky we survey. If the maximum T_s were distributed as χ^2, then this could not be true.

One attempt to provide this area dependence has been by acting as though the maximum T_s in a region is the maximum of some (discrete) number of independent random variables, where each of these random variables has a χ^2 distribution. Empirically, it is seen that the χ_3^2 with some number of trials gives a good fit to the Monte

Carlo distribution [63]. An alternate distribution, with a somewhat more convincing derivation is presented here [1, 92].

6.2   Distribution at a fixed point

Wilks' theorem does provide the distribution of T_s at a fixed source position: the degeneracy discussed above is then removed. As has been pointed out several times, and verified by Monte Carlo [63, 103], this distribution is χ_1^2, that is, χ^2 with one degree of freedom, with one complication. Since negative source fluxes are not permitted, half of our T_s values will be zero. Thus the probability distribution of the fixed T_s is:

$$
P_{fixed}(T_s) = \begin{cases} \frac{1}{4\pi}e^{-T_s^2} & T_s > 0 \\ \frac{1}{2}\delta(T_s) & T_s = 0 \\ 0 & T_s < 0 \end{cases}
$$

In practice, since we only wish to look for the maximum T_s in a region, we can take the distribution to be a full Gaussian instead, as it does not matter whether half the values are negative or identically zero: only the positive values have any chance of being the largest T_s found.

Thus, we see that the problem of finding the maximum T_s is equivalent to finding the maximum value of a two dimensional Gaussian random field, where adjacent values have some correlation.

6.3   The One Dimensional Problem

Before presenting the solution to our two dimensional problem, it is instructive to look at the one dimensional case. That is, we examine the distribution of the maximum of a stochastic function $x = f(t)$ where the distribution of x at any point is Gaussian. To account for the correlation in values, we have a distribution of $v = \frac{df(t)}{dt}$.

The problem of finding the probability of a maximum is most easily approached by finding the distribution of upcrossings of the function: that is, where the function

crosses the line $x = b$ while increasing. We start with the probability of an upcrossing in the interval $[t, t + dt]$ as

$$p(b|t)dt = \int_0^\infty f(b, v|t)v \, dv \, dt \tag{6.1}$$

This reduces, for a normal, stationary function with mean zero, to

$$p(b)dt = \frac{1}{2\pi}e^{-\frac{b^2}{2\sigma_x^2}}\frac{\sigma_v}{\sigma_x} \, dt. \tag{6.2}$$

This may be rewritten in terms of the correlation function $C(t)$, as

$$p(b)dt = \frac{1}{2\pi C(0)}e^{-\frac{b^2}{2\sigma_x^2}}\frac{\partial^2 C(t)}{\partial t^2} \, dt. \tag{6.3}$$

In a regime where upcrossings are uncommon, the probability that $\max f(t) < b$ in the interval $[0, \text{T}]$ is equal to the probability that there are no upcrossings of b:

$$
\begin{aligned}
P(\max f < b) &= e^{-Tp(b)} \\
&= \exp\left[-\frac{T}{2\pi C(0)}e^{-\frac{b^2}{2\sigma_x^2}}\frac{\partial^2 C(t)}{\partial t^2}\right].
\end{aligned}
\tag{6.4}
$$

Noting that $\frac{\partial P(\max f\ <b)}{\partial b}db = -P(\max f = b)db$, we can solve for the distribution of $\max f$ in an interval of length T:

$$
\begin{aligned}
P(\max f = b)db &= -\frac{\partial}{\partial b}\exp\left[-\frac{T}{2\pi C(0)}e^{-\frac{b^2}{2\sigma_x^2}}\frac{\partial^2 C(t)}{\partial t^2}\right]db \\
&= -\exp\left[-Ae^{-\frac{b^2}{2\sigma_x^2}}\right]\left(Ae^{-\frac{b^2}{2\sigma_x^2}}\right)\frac{b}{\sigma_x^2} \, db,
\end{aligned}
\tag{6.5}
$$

where $A = \frac{T}{2\pi C(0)}\frac{\partial^2 C(t)}{\partial t^2}$.

6.4 The Multidimensional Problem

By extension, in the multi-dimensional case we have a similar result [1]. If our Gaussian stochastic function is $F(\mathbf{x})$, we first must find the correlation matrix of F, $\mathbf{\Lambda}$,

defined through

$$\langle F(\mathbf{x})F(\mathbf{x}+\delta)\rangle = 1 - \frac{1}{2}\delta^T \mathbf{\Lambda}\delta + O(|\delta|^4)$$

The density of large values of F is

$$\lambda_b = \frac{1}{2\pi}\,|\mathbf{\Lambda}|^{\frac{1}{2}}\,b\phi(b)$$

where $|\mathbf{\Lambda}|$ is the determinant of $\mathbf{\Lambda}$, and $\phi(b)$ is the standard Normal density:

$$\phi(x) = \frac{1}{\sqrt{2\pi}}e^{-\frac{x^2}{2}}$$

By using $F(\mathbf{x}) = [T_s(\ell,b)]^2$, we find that the distribution of the maximum T_s in an area A is given by

$$
\begin{aligned}
P(\max_A T_s < k) &= e^{-\lambda_{k^2}A} \\
&= e^{-\frac{1}{2\pi}|\mathbf{\Lambda}|^{\frac{1}{2}}k^2\frac{1}{\sqrt{2\pi}}e^{-\frac{k^4}{2}}A} \\
&= \exp\left(-A(2\pi)^{-\frac{3}{2}}\,|\mathbf{\Lambda}|^{\frac{1}{2}}\,k^2 e^{-\frac{k^4}{2}}\right).
\end{aligned}
\tag{6.6}
$$

The distribution can be calculated as before by taking the derivative, but this cumulative distribution is most appropriate for finding the significance of an observed T_s. The traditional [63] distribution to use for large values of T_s has been χ^2_3 with some number of trials, where the number of trials was found by Monte Carlo. The method presented here also has one free parameter, $|\mathbf{\Lambda}|$, which must be found by Monte Carlo if one cannot calculate it a priori (which appears to be difficult).

One could calculate $|\mathbf{\Lambda}|$ from a simulation, but without the large number of trials required for the Monte Carlo, however. The easiest way to do this would probably be using the identity:

$$\Lambda_{ij} = \left\langle \frac{\partial F(\mathbf{x})}{\partial x_i}\frac{\partial F(\mathbf{x})}{\partial x_j}\right\rangle$$

Chapter 7

Quantifying Source Variability

7.1 Introduction

One of the biggest questions raised by the EGRET mission is that of the nature of the unidentified sources. Certainly some of these will turn out to be AGN [103], and it is likely that some of the ones near the galactic plane are associated with pulsars [104, 73, 69] and supernova remnants [91, 25]. A few, as well, may be discovered to be artifacts of the galactic diffuse emission. But as has been discussed elsewhere [69], there are more unidentified sources than expected from these populations. The large error regions for the *EGRET* sources often make it difficult to discern which of several candidates is the true counterpart in another wavelength.

When studying the unidentified sources, there are several observables which one might use to determine their nature. One can look at the spatial distribution [53, 38] to estimate what fraction of the population is galactic in nature, and what scale height the galactic fraction has. One can look at positional correlations with other source types [100, 40]. The energy spectrum is another source characteristic which can be used to classify it as "pulsar-like", "AGN-like", or "other" [69].

In this same vein, one can examine the EGRET catalog sources for evidence of time variability, in hopes of distinguishing the various source classes. The known pulsars are seen to have a fairly constant flux (when averaged over many pulse periods), as is expected from the nature of their energy production, while AGN are seen to flare

dramatically. Certainly, if an unidentified source has an obvious flare, we can rule out the possibility that it is a pulsar, and raise the likelihood that it is an AGN or another type of flaring source. But, as with many aspects of the EGRET data, it is difficult to characterize the time variability of most sources, because of the limited statistics and the non-continuous observations. Thus it is natural to look for a statistic which will measure the variability in a rigorous way.

7.1.1   Previous Methods

The primary method used for estimating the variability of EGRET sources has been that introduced by McLaughlin et al. [66]. This method finds the χ^2 of the measured source intensities, and uses $V = -\log Q$, where Q is the probability of obtaining such a large χ^2 if the source flux were constant. There are some complications, such as what to do if there is only an upper limit in a given observation, but this is the general approach.

There are two problems with this method: one statistical, and one conceptual. The statistical problem is that introduced when using upper limits: McLaughlin et al. use zero as the flux estimate when the measured flux estimate would be negative, and use the LIKE upper limits as the error in that estimate. As discussed in §5, these upper limits (together with the flux estimate) are not statistically meaningful as defining a confidence interval. Thus the resulting "χ^2" will not have a χ^2 distribution. Since the LIKE results are statistically conservative, this means that sources which have upper limits included in the analysis will have a lower V than implied by the data.

The conceptual problem with the method is the use of a χ^2 statistic to determine variability. The V statistic is a measure of how inconsistent the data is with the model that the source flux is constant. Thus, sources with a large V are inconsistent with being constant. But we do not know whether such a source has a large V because of large intensity fluctuations, or because of small error bars on the intensity measurements. Similarly, a source with a small V might truly be constant, or might have just have very poor measurements of its flux.

As an example, take a source with an intrinsic variability of 10%. If our measurements of the source flux have an error of 30%, it will have a small V. If our measurements have an error of 1%, it will have quite a large V. Thus, while the V statistic is useful for excluding possible pulsar candidates (by excluding those which are inconsistent with being constant), it is not useful for finding sources which have low intrinsic variability, or for comparing variabilities of sources which have different errors in their flux measurements.

7.2   A Likelihood Approach

7.2.1   What Do We Want to Measure?

The question remains: if we don't really want to measure the χ^2 of a source, what *do* we want to measure? One possibility is the standard deviation of the true flux of a source. This has the following problem: if one views two identical sources, with one twice as far away as the other (and with 1/4 the flux), then the further one will have 1/4 the standard deviation of the closer one.

Another possibility is to estimate the standard deviation of the true flux divided by the true flux. This fractional variability is much closer to what we really want to know about a source, particularly one which always has the same level of variability. There could be other statistics which might be more meaningful for flaring sources, such as the peak flare flux divided by the quiescent level.

In the spirit of measuring fractional variability, we can define*

$$\tau \equiv \frac{\sigma}{\mu}, \tag{7.1}$$

where μ and σ are the average and standard deviation, respectively, of the true flux of the source. Since we have errors in our flux measurements, we must now find a way to estimate τ given the data.

---

*This ratio was defined as "V" by Raleigh [55]. It is defined here as "τ" to minimize confusion with McLaughlin *et al.*'s "V" statistic.[66]

7.2.2   Modeling the Source Flux Distribution

In the spirit of likelihood analysis, we begin by constructing models, for which we can calculate the likelihood of obtaining our data. Our model in this case is the distribution from which the true source fluxes are drawn. Note that there are an infinite number of source flux distributions which will yield the same τ; we want to pick one that is compatible with our notions of what the true source flux distribution should be, but which is fairly general at the same time.

First, we will assume that the source flux is uncorrelated at different times. This can be, in fact, a very poor assumption: AGN flares can last for weeks, or just days. The presence of these correlations means that our estimate of τ will depend on the time scales at which we are looking. If we want to look for long term variability, we should average together observations which take place in the same short time interval. If we wish to examine short time scale variability, we should take out the long time scale variability by normalizing observations to the average within some longer interval.

The first source flux distribution one might try is a Gaussian. Thus, we would find the likelihood of obtaining our data given that the true flux S was drawn from a Gaussian with mean μ and standard deviation $\sigma = \tau\mu$. We could then find the maximum likelihood value of τ, together with a confidence interval for τ defined in the standard way (see §3.1.2). Alternatively, we could follow the Bayesian procedure: form priors for the distributions of μ and τ, and find an estimate of τ, together with an error region, by marginalizing over μ.

The use of the Gaussian distribution for source fluxes has a flaw, however. It allows the possibility of $\mu = 0$ ($\Rightarrow \tau = \infty$), as well as the possibility of negative μ. Thus, we will instead use the log-normal distribution; that is, that $\ln S$ has a Gaussian distribution with

$$\mu_{\ln S} = \ln \mu - 1/2\sigma^2, \tag{7.2}$$

and

$$\sigma_{\ln S} = \sqrt{\ln \frac{\sigma^2}{\mu^2} + 1}. \tag{7.3}$$

This distribution is generally appropriate for quantities which are bounded below by zero and unbounded above, and for quantities where the scatter is proportional to the value, as is the case here.

7.2.3   Characterizing the Single-Measurement Likelihood

It is standard in EGRET analysis to calculate the likelihood of the observed data for a certain source flux (§3). Typically, the values output by an analysis program are the most likely flux, and a confidence interval. In the case of upper limits, the most likely flux is taken as zero, and the confidence interval might be defined in one of several ways (§5).

For this work, we would like to be able to calculate the likelihood for any source flux, not necessarily one near the maximum likelihood value. Thus it is useful to look for a parameterized family of curves which will closely fit the full likelihood function.

If the photons had no spatial measurement, there would be an obvious form of such a function. We could simply write the expected number of counts as $\mu = N_S + N_B$, and then find the Poisson likelihood of observing N photons:

$$
\begin{aligned}
\mathcal{L}(N_S) &= \frac{e^{\mu}(\mu)^N}{N!} \\
&= \frac{e^{-(N_S+N_B)}(N_S + N_B)^N}{N!},
\end{aligned}
$$

giving us a two parameter fit (N and N_B) to $\mathcal{L}(N_S)$.

When we seek to include the effects of the instrument point spread function, we must replace the numbers of counts above with some "effective" number of counts. A photon closer to the source position will be weighted more than one far away, in some sense. To translate between the true source flux and an effective number of counts, we can include an extra parameter, S_M, and try

$$
\mu = S \times S_M + S_0 \tag{7.4}
$$
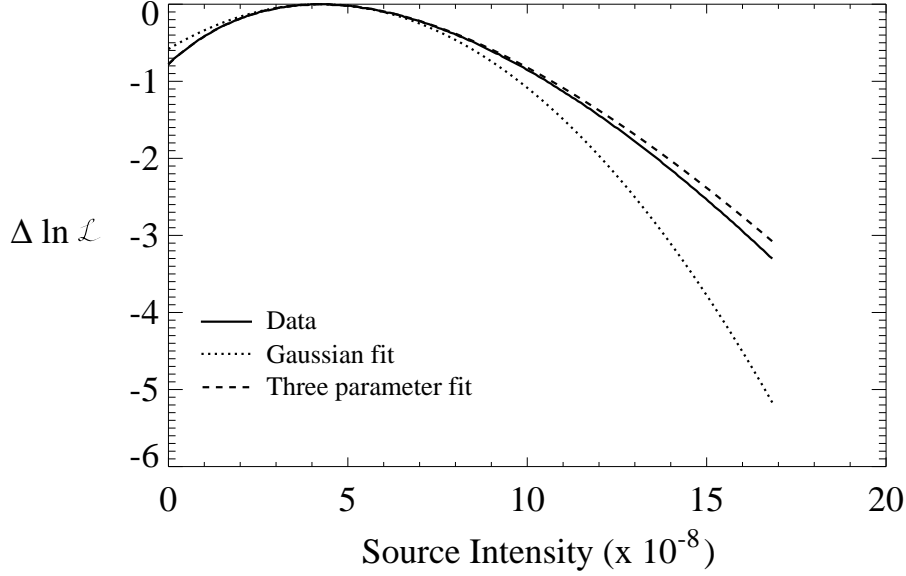
Figure 7.1:   The likelihood curve for a sample source, together with a Gaussian of the same width, and a curve of the form in equation (7.5)

which yields a parameterization of the form

$$\mathcal{L}(S) = \frac{e^{-(S \times S_M + S_0)}(S \times S_M + S_0)^{N_{\text{eff}}}}{N_{\text{eff}}!}. \tag{7.5}$$

This form fits the observed likelihood functions rather well (Figure 7.1) , both in cases of large source flux and in upper limit situations.

Rather than providing S_M, S_0, and N_{eff} for source measurements, it is convenient to transform to a set of variables more related to the measured source flux and the error in that measurement. It can be shown that the maximum likelihood value of S occurs at

$$\mu_S = \frac{N_{\text{eff}} - S_0}{S_M}, \tag{7.6}$$

and that the second derivative of the likelihood function (which equals the standard

deviation if the distribution is Gaussian) is

$$\sigma_S = \frac{\sqrt{N_{\text{eff}}}}{S_M}. \tag{7.7}$$

Thus the likelihood as a function of source flux in a given viewing period can also be characterized by μ_S, σ_S, and S_M.

7.2.4   Calculating τ

With the parameterized distribution of source fluxes from the preceding section, we can write the likelihood of observing a given viewing period's worth of data (D^i) from a source with a certain μ and τ:

$$\begin{aligned}
\mathcal{L}(\mu, \tau, D^i) &= \int_0^\infty dS^i \, P(D^i|S^i) P(S^i|\mu, \tau) \tag{7.8} \\
&= \int_0^\infty dS^i \, \frac{e^{-(S^i \times S_M^i + S_0^i)}(S^i \times S_M^i + S_0^i)^{N_{\text{eff}}^i}}{N_{\text{eff}}^i!} \\
&\quad \times \frac{1}{S^i \sqrt{2\pi \ln(\tau^2 + 1)}} \left[\frac{\mu}{S^i \sqrt{\tau^2 + 1}}\right]^{\frac{1}{2\ln(\tau^2+1)}}, \tag{7.9}
\end{aligned}$$

where the second term in equation (7.9) is the Log-normal distribution written in terms of μ and τ.

The likelihood of a sequence of observations $(D^1 \ldots D^M)$ will then be

$$\mathcal{L}(\mu, \tau) = \prod_{i=1}^M \mathcal{L}(\mu, \tau, D^i),$$

or

$$\ln \mathcal{L}(\mu, \tau) = \sum_{i=1}^M \ln \mathcal{L}(\mu, \tau, D^i). \tag{7.10}$$

7.2.5   Dealing with Time Scales

Up to this point we have assumed that the source flux during each measurement was drawn independently from the same distribution. This can be problematic if the

measurements last for varying lengths of time. For example, in the *EGRET* data, there are frequently several successive viewing periods of a few days duration, pointing in nearly the same direction. This is in contrast to the normal mode of pointing in one direction for two weeks at a time. We do not want our results to depend on whether or not a two week viewing period was chopped into several bits.

The simplest solution is to lump together successive measurements, when they are on a short enough time scale, and treat them as one measurement. This simply involves replacing the first term in equation (7.9) with the product of several identical terms, one for each sub-measurement.

7.3   Extensions of the Method

There are several ways in which this method could be extended. One of the simplest would be to use a different distribution than the log-normal as the distribution of source fluxes. One could experimentally measure such distributions in hopes of using a more accurate one.

A much more complex (but probably more useful) extension would be to add time dependent correlations to the model. Thus the true source flux as a function of time would be modeled as a time series with a certain spectrum in its correlation function. This would be much more difficult computationally, and one would have to pick an appropriate spectrum for the correlation. The benefit, however, would be a much more realistic model of the variability.

Chapter 8

Time Variability of the *EGRET* Sources

8.1 Introduction

In this chapter we apply the variability analysis described in Chapter 7 to the sources listed in the third *EGRET* catalog [40]. Variability on time scales longer than one month is examined for each source in the catalog, and the variability of various source classes is compared.

8.2 Method

The first step in this analysis was the re-analysis of the third *EGRET* catalog with the `unlike` program. For each Viewing Period, any of the 271 catalog sources which were within the instrument's field of view were added to the source list. In addition, any of the 145 marginal sources (which were used in the original analysis of the catalog but were not significant enough to merit inclusion in the official list) which were in the field of view were added as well. The maximum likelihood set of source fluxes was then found. For each source, the parameters characterizing $\mathcal{L}(S)$ described in §7.2.3 were found. All source measurements were of flux (> 100 MeV), assuming a spectral index of 2.0, using all data within $15°$ of each source, and included all nearby

sources (both catalog and marginal) in the model. All data collected through VP6111 (corresponding to 18 Feb 1997) were used.

The likelihood of the sequence of observations as a function of τ was then calculated, as in §7.2.4. All observations within one month of each other were lumped together, as per §7.2.5.

8.3   Systematic Errors

There are two main sources of systematic error in this analysis. The first is from the instrument itself. As discussed elsewhere [100, 40, 26], the sensitivity of the *EGRET* instrument is time variable. Despite efforts to measure and compensate for long term drifts [26], there is a residual variability of about 10%. In an effort to minimize this systematic error, only source observations within 25° of the instrument axis were used in the analysis.

Because of this variability, the background levels G_M and G_B were allowed to vary from viewing period to viewing period for a given source. Otherwise, a 5% change in a strong background could lead to a large change in a source flux.

The background levels were also allowed to float when $\mathcal{L}(S)$ was calculated. Unfortunately, computational limitations precluded allowing nearby sources to vary during this calculation as well. Thus, nearby sources were fixed at their maximum likelihood intensities (calculated for that viewing period). This will lead to an underestimation of the error in flux, particularly for sources which have another source very close by.

As both systematic effects will tend to exaggerate source variability, it is expected that even constant sources will show some small variability. To the extent that the systematics are dominated by the instrumental effects, the measured variability will be equal to the true variability added in quadrature to a constant systematic variability of about 10%.

8.4 Results

A list of the Third *EGRET* Catalog sources, together with their measured variabilities, is given in Table 8.1. For each source, the 68% upper and lower limits on τ are given as well, together with the mean of the best fit log-normal flux distribution, and the number of observations (within 25°) used in the analysis.

3EG Name	ℓ	b	τ	L limit	U limit	Avg Flux[a]	Num Obs
J0010+7309	119.92	10.54	0.31	0.16	0.55	3.99	4
J0038-0949	112.69	-72.44	0.00	0.00	0.89	1.24	3
J0118+0248	136.23	-59.36	5.17	0.90	∞^b	0.92	4
J0130-1758	169.71	-77.11	0.00	0.00	0.38	1.19	4
J0159-3603	248.89	-73.04	0.00	0.00	1.16	0.79	4
J0204+1458	147.95	-44.32	6.14	1.08	∞	1.62	3
J0210-5055	276.10	-61.78	0.31	0.21	0.48	8.80	7
J0215+1123	153.75	-46.37	10.06	1.19	∞	1.39	3
J0222+4253	140.14	-16.77	0.00	0.00	0.23	2.02	4
J0229+6151	134.20	1.15	0.39	0.16	0.74	3.57	7
J0237+1635	156.77	-39.11	1.16	0.62	3.88	2.98	3
J0239+2815	150.21	-28.80	0.00	0.00	0.24	1.60	5
J0241+6103	135.87	0.99	0.49	0.33	0.79	6.44	7
J0245+1758	157.62	-37.11	2.63	0.73	2287.08	0.99	4
J0253-0345	179.70	-52.56	16.44	1.38	∞	2.74	2
J0323+5122	145.64	-4.67	0.92	0.38	3.23	1.03	8
J0329+2149	164.90	-27.88	0.00	0.00	1.74	0.74	5
J0340-0201	188.00	-42.45	0.00	0.00	0.76	0.94	2
J0348+3510	159.06	-15.01	0.51	0.00	1.41	1.27	6
J0348-5708	269.35	-46.79	6.60	1.29	∞	0.51	10
J0404+0700	184.00	-32.15	0.34	0.00	1.65	0.94	7
J0407+1710	175.63	-25.06	1.33	0.27	19.75	0.59	11
J0412-1853	213.90	-43.29	0.00	0.00	∞	0.06	2
J0416+3650	162.22	-9.97	0.63	0.32	1.17	1.74	9

<div align="center">Table 8.1 continued on next page</div>

---

[a]$\times 10^{-7}$ cm^{-2} s^{-1}($E > 100 MeV$)

[b]All values larger than 10,000 are printed as ∞

Table 8.1 – *continued*

3EG Name	ℓ	b	τ	L limit	U limit	Avg Flux	Num Obs
J0422-0102	194.88	-33.12	0.00	0.00	0.57	1.03	5
J0423+1707	178.48	-22.14	0.51	0.10	1.08	1.35	12
J0426+1333	181.98	-23.82	0.29	0.00	0.71	1.71	14
J0429+0337	191.44	-29.08	0.00	0.00	0.45	1.54	9
J0433+2908	170.48	-12.58	0.39	0.21	0.63	2.70	13
J0435+6137	146.50	9.50	0.00	0.00	0.30	1.57	9
J0439+1105	186.14	-22.87	0.00	0.00	0.42	1.06	14
J0439+1555	181.98	-19.98	1.70	0.74	12.73	0.69	14
J0442-0033	197.20	-28.46	∞	11.21	∞	92.90	9
J0450+1105	187.86	-20.62	1.60	0.99	3.50	1.78	14
J0456-2338	223.96	-34.98	0.16	0.00	1.07	0.95	5
J0458-4635	252.40	-38.40	0.50	0.00	1.26	0.83	7
J0459+0544	193.99	-21.66	0.76	0.08	2.67	0.55	12
J0459+3352	170.25	-5.77	0.56	0.27	1.09	1.46	14
J0500+2529	177.18	-10.28	0.00	0.00	1.08	0.51	14
J0500-0159	201.35	-25.47	2.20	0.92	19.25	1.03	10
J0510+5545	153.99	9.42	0.00	0.00	0.26	2.16	9
J0512-6150	271.25	-35.28	0.00	0.00	0.55	0.55	10
J0516+2320	181.15	-8.77	9.43	1.49	∞	0.48	14
J0520+2556	179.65	-6.40	0.00	0.00	0.31	1.33	14
J0521+2147	183.08	-8.43	0.35	0.00	0.69	1.76	14
J0530+1323	191.37	-11.01	0.74	0.58	1.00	8.04	15
J0530-3626	240.94	-31.29	0.61	0.15	2.28	1.34	3
J0531-2940	233.44	-29.31	0.93	0.22	8.07	0.81	4
J0533+4751	162.61	7.95	0.00	0.00	0.32	1.40	9
J0533-6916	279.73	-32.09	0.00	0.00	0.60	1.65	9
J0534+2200	184.56	-5.78	0.00	0.06	0.10	22.47	14
J0540-4402	250.08	-31.09	0.85	0.56	1.48	3.32	7
J0542+2610	182.02	-1.99	0.70	0.34	1.40	1.49	14
J0542-0655	211.28	-18.52	26.39	2.24	∞	2.39	8
J0546+3948	170.75	5.74	0.11	0.00	0.47	1.71	12
J0556+0409	202.81	-10.29	50.00	0.00	∞	0.00	13
J0613+4201	171.32	11.40	0.71	0.28	1.64	0.99	11

Table 8.1   *continued on next page*

Table 8.1 – continued

3EG Name	ℓ	b	τ	L limit	U limit	Avg Flux	Num Obs
J0616-0720	215.58	-11.06	0.00	0.00	2.04	0.47	10
J0616-3310	240.35	-21.24	0.16	0.00	0.75	1.92	3
J0617+2238	189.00	3.05	0.26	0.15	0.38	5.36	14
J0622-1139	220.16	-11.69	1.35	0.45	11.23	1.49	6
J0628+1847	193.66	3.64	50.00	0.00	∞	0.00^c	12
J0631+0642	204.71	-1.30	75.89	7.89	∞	0.00	16
J0633+1751	195.13	4.27	0.12	0.10	0.16	39.99	12
J0634+0521	206.18	-1.41	72.05	5.15	∞	0.00	16
J0702-6212	272.65	-22.56	1.55	0.67	8.37	0.68	11
J0706-3837	249.57	-13.76	0.00	0.00	1731.83	0.36	4
J0721+7120	143.98	28.02	0.08	0.00	0.28	1.89	7
J0724-4713	259.00	-14.38	2.53	0.87	91.40	1.14	6
J0725-5140	263.29	-16.02	1.09	0.51	4.05	0.87	8
J0737+1721	201.85	18.07	0.00	0.00	0.49	1.53	5
J0743+5447	162.99	29.19	2.46	0.99	32.90	1.10	7
J0747-3412	249.35	-4.48	0.58	0.00	1.64	1.98	7
J0808+4844	170.46	32.48	0.00	0.00	0.39	1.02	7
J0808+5114	167.51	32.66	0.00	0.00	0.73	0.62	6
J0808-5344	268.24	-11.20	1.42	0.69	4.93	1.20	10
J0812-0646	228.64	14.62	0.00	0.00	0.66	2.33	3
J0821-5814	273.10	-12.04	5.75	1.14	∞	0.59	10
J0824-4610	263.28	-4.89	1.25	0.00	36.72	1.28	9
J0827-4247	260.84	-2.46	0.00	0.00	0.54	1.88	8
J0828+0508	219.60	23.82	0.00	0.00	∞	0.50	4
J0828-4954	266.76	-6.45	0.62	0.28	1.43	1.92	9
J0829+2413	200.02	31.87	0.54	0.28	1.27	4.48	2
J0834-4511	263.55	-2.79	0.17	0.12	0.24	101.07	9
J0841-4356	263.29	-1.10	4.03	0.83	∞	1.44	8
J0845+7049	143.54	34.43	0.65	0.33	1.40	0.93	6
J0848-4429	264.50	-0.46	1.31	0.19	33.43	1.26	8

---

^{c}A fitted mean flux of zero indicates either an unphysically strict upper limit, due to instrument systematics, or numerical convergence problems with the method. Such sources are most likely variable, but caution should be used in interpreting the results.

Table 8.1 – continued

3EG Name	ℓ	b	τ	L limit	U limit	Avg Flux	Num Obs
J0852-1216	239.06	19.99	2.06	0.74	147.20	1.39	5
J0853+1941	206.81	35.82	0.00	0.00	0.37	1.11	4
J0859-4257	264.57	2.01	0.23	0.00	0.73	2.36	8
J0903-3531	259.40	7.40	0.52	0.19	1.20	1.69	7
J0910+6556	148.30	38.56	0.49	0.00	1.14	0.79	6
J0917+4427	176.11	44.19	0.00	0.00	0.34	1.63	6
J0952+5501	159.55	47.33	0.46	0.00	0.84	1.16	10
J0958+6533	145.75	43.13	1.17	0.55	5.06	0.64	8
J1009+4855	166.87	51.99	0.00	0.00	0.60	0.51	9
J1013-5915	283.93	-2.34	0.22	0.00	0.46	4.65	11
J1014-5705	282.80	-0.51	0.65	0.33	1.13	4.17	12
J1027-5817	284.94	-0.52	0.26	0.09	0.45	6.93	11
J1045-7630	295.66	-15.45	0.00	0.00	0.28	1.52	9
J1048-5840	287.53	0.47	0.00	0.00	0.18	5.93	10
J1052+5718	149.47	53.27	0.21	0.00	0.74	0.66	6
J1058-5234	285.98	6.65	0.00	0.00	0.25	3.28	10
J1102-6103	290.12	-0.92	0.00	0.00	0.90	2.78	9
J1104+3809	179.83	65.03	0.33	0.05	0.63	1.41	8
J1133+0033	264.52	57.48	0.71	0.16	2.00	0.58	11
J1134-1530	277.04	43.48	2.85	1.11	51.53	1.12	10
J1200+2847	199.42	78.38	2.36	1.16	11.36	1.32	10
J1212+2304	235.57	80.32	78.82	0.00	∞	0.00	13
J1219-1520	291.56	46.82	1.78	0.74	13.70	0.56	12
J1222+2315	241.87	82.39	61.09	2.44	∞	0.48	12
J1222+2841	197.27	83.52	0.58	0.31	1.02	1.51	9
J1224+2118	255.07	81.66	0.47	0.20	0.90	1.27	11
J1227+4302	138.63	73.33	136.23	2.90	∞	3.20	5
J1229+0210	289.95	64.36	0.51	0.35	0.77	2.30	11
J1230-0247	292.58	59.66	0.60	0.27	1.25	0.66	11
J1234-1318	296.43	49.34	0.42	0.12	0.81	0.89	11
J1235+0233	293.28	65.13	0.23	0.00	0.65	0.66	11
J1236+0457	292.59	67.52	0.00	0.00	1.45	0.38	11
J1246-0651	300.96	55.99	0.59	0.33	1.03	1.08	11

Table 8.1

Table 8.1 – continued

3EG Name	ℓ	b	τ	L limit	U limit	Avg Flux	Num Obs
J1249-8330	302.86	-20.63	0.71	0.18	2.74	1.12	6
J1255-0549	305.09	57.06	1.60	1.11	2.71	5.99	11
J1300-4406	304.60	18.74	0.48	0.00	1.57	0.70	8
J1308+8744	122.74	29.38	0.00	0.00	0.57	0.59	9
J1308-6112	305.01	1.59	0.72	0.38	1.53	3.07	10
J1310-0517	311.69	57.25	2.94	1.69	7.92	4.32	11
J1314-3431	308.21	28.12	0.00	0.00	0.25	1.51	6
J1316-5244	306.85	9.93	0.39	0.00	0.81	1.83	9
J1323+2200	359.33	81.15	2.69	0.93	46.77	0.79	9
J1324-4314	309.32	19.21	0.00	0.00	0.30	1.42	8
J1329+1708	346.29	76.68	0.60	0.00	5.51	0.21	13
J1329-4602	309.83	16.32	0.00	0.00	0.48	1.02	8
J1337+5029	105.40	65.04	0.54	0.00	1.35	1.08	6
J1339-1419	320.07	46.95	0.68	0.17	1.70	0.69	10
J1347+2932	47.32	77.50	0.48	0.00	1.45	1.14	7
J1409-0745	333.88	50.28	14.43	3.39	917.88	6.16	11
J1410-6147	312.18	-0.35	0.33	0.16	0.55	8.95	8
J1420-6038	313.63	0.37	1.22	0.51	7.43	3.52	8
J1424+3734	66.82	67.76	0.01	0.00	∞	1.50	1
J1429-4217	321.45	17.27	1.11	0.58	3.20	1.31	10
J1447-3936	326.12	17.96	0.27	0.00	0.85	1.13	11
J1457-1903	339.88	34.60	0.42	0.00	3.64	0.68	6
J1500-3509	330.91	20.45	0.00	0.00	0.61	1.03	11
J1504-1537	344.04	36.38	10.33	1.21	∞	1.47	5
J1512-0849	351.49	40.37	0.00	0.00	0.32	2.35	5
J1517-2538	339.76	26.60	0.00	0.00	8.90	0.43	8
J1527-2358	342.97	26.50	4.04	0.00	∞	0.49	11
J1600-0351	6.30	34.81	68.17	0.00	∞	0.00	4
J1605+1553	29.18	43.84	0.00	0.00	0.56	1.45	4
J1607-1101	0.91	29.05	2370.92	6.19	∞	16.37	11
J1608+1055	23.03	40.79	1.92	0.45	4993.42	1.91	2
J1612-2618	349.76	17.64	1.78	0.76	11.74	1.02	15
J1614+3424	55.15	46.38	0.73	0.45	1.36	4.03	5

Table 8.1 *continued on next page*

Table 8.1 – *continued*

3EG Name	ℓ	b	τ	L limit	U limit	Avg Flux	Num Obs
J1616-2221	353.00	20.03	0.00	0.00	0.33	1.56	15
J1621+8203	115.53	31.77	0.00	0.00	0.29	1.16	5
J1625-2955	348.82	13.32	4.56	2.23	18.18	8.80	15
J1626-2519	352.14	16.32	1.64	0.79	6.02	1.65	16
J1627-2419	353.36	16.71	0.00	0.00	0.35	2.10	15
J1631-1018	5.55	24.94	0.38	0.00	0.89	1.34	13
J1631-4033	341.61	5.24	0.62	0.23	1.28	1.76	16
J1633-3216	348.10	10.48	0.51	0.00	1.09	1.30	16
J1634-1434	2.33	21.78	0.00	0.00	0.55	1.08	13
J1635+3813	61.09	42.34	0.35	0.13	0.71	2.28	5
J1635-1751	359.72	19.56	2.38	0.00	∞	0.30	16
J1638-2749	352.25	12.59	0.45	0.23	0.76	2.03	17
J1638-5155	334.05	-3.34	0.00	0.00	0.69	4.55	15
J1639-4702	337.75	-0.15	0.00	0.00	0.38	6.63	14
J1646-0704	10.85	23.69	0.68	0.28	1.42	1.55	13
J1649-1611	3.35	17.80	0.54	0.00	1.40	1.28	17
J1652-0223	15.99	25.05	0.00	0.00	0.62	1.27	8
J1653-2133	359.49	13.81	1.34	0.65	4.65	0.91	17
J1655-4554	340.48	-1.61	0.91	0.46	2.27	2.94	15
J1659-6251	327.32	-12.47	0.75	0.00	3.31	1.20	8
J1704-4732	340.10	-3.79	29.90	2.67	∞	2.93	15
J1709-0828	12.86	18.25	0.84	0.11	2.21	1.18	13
J1710-4439	343.10	-2.69	0.16	0.06	0.27	13.49	17
J1714-3857	348.04	-0.09	0.15	0.00	0.38	6.01	16
J1717-2737	357.67	5.95	0.99	0.60	1.90	2.20	18
J1718-3313	353.20	2.56	0.93	0.54	1.85	2.59	18
J1719-0430	17.80	18.17	0.00	0.00	0.39	1.63	10
J1720-7820	314.56	-22.17	0.65	0.00	∞	0.37	3
J1726-0807	15.52	14.77	0.35	0.00	0.81	1.93	14
J1727+0429	27.27	20.62	0.31	0.00	0.87	1.84	5
J1733+6017	89.12	32.94	0.39	0.00	1.38	1.29	6
J1733-1313	12.03	10.81	0.31	0.17	0.49	3.96	14
J1734-3232	355.64	0.15	0.00	0.00	0.24	4.12	19

Table 8.1 – *continued*

3EG Name	ℓ	b	τ	L limit	U limit	Avg Flux	Num Obs
J1735-1500	10.73	9.22	1.09	0.00	10.14	0.52	16
J1736-2908	358.79	1.56	0.66	0.40	1.09	4.13	18
J1738+5203	79.37	32.05	1.01	0.49	3.12	1.91	6
J1741-2050	6.44	5.00	0.41	0.14	0.70	2.74	17
J1741-2312	4.42	3.76	0.52	0.18	1.03	2.17	18
J1744-0310	22.19	13.42	0.72	0.26	1.94	1.20	9
J1744-3011	358.85	-0.52	0.38	0.20	0.62	7.74	18
J1744-3934	350.81	-5.38	0.63	0.28	1.17	2.42	15
J1746-1001	16.34	9.64	0.32	0.00	0.60	2.50	14
J1746-2851	0.11	-0.04	0.50	0.36	0.69	12.04	18
J1757-0711	20.30	8.47	0.52	0.00	0.99	2.37	16
J1800-0146	25.49	10.39	0.00	0.00	0.48	1.99	10
J1800-2338	6.25	-0.18	0.03	0.00	0.32	6.11	19
J1800-3955	352.45	-8.43	0.00	0.00	0.84	0.77	16
J1806-5005	343.29	-13.76	1.30	0.00	39.40	0.46	12
J1809-2328	7.47	-1.99	0.69	0.49	1.02	6.06	18
J1810-1032	18.81	4.23	0.35	0.00	0.79	2.16	16
J1812-1316	16.70	2.39	0.94	0.61	1.65	3.80	17
J1813-6419	330.04	-20.32	0.00	0.00	0.54	1.65	4
J1822+1641	44.84	13.84	1.91	0.77	26.63	1.98	6
J1823-1314	17.94	0.14	0.72	0.40	1.37	4.06	16
J1824+3441	62.49	20.14	68.64	6.86	∞	0.00	11
J1824-1514	16.37	-1.16	0.00	0.00	0.51	3.60	16
J1825+2854	56.79	18.03	73.19	2.59	∞	0.00	10
J1825-7926	314.56	-25.44	0.75	0.22	3.06	2.32	4
J1826-1302	18.47	-0.44	0.75	0.49	1.28	5.74	16
J1828+0142	31.90	5.78	3982.51	6.92	∞	57.13	8
J1832-2110	12.17	-5.71	0.52	0.25	0.92	2.32	15
J1834-2803	5.92	-8.97	0.00	0.00	0.42	1.61	16
J1835+5918	88.74	25.07	0.15	0.00	0.32	7.29	4
J1836-4933	345.93	-18.26	0.00	0.00	0.64	0.98	11
J1837-0423	27.44	1.06	12.01	2.17	∞	5.88	10
J1837-0606	25.86	0.40	0.24	0.00	0.49	6.24	10

Table 8.1 – *continued*

3EG Name	ℓ	b	τ	L limit	U limit	Avg Flux	Num Obs
J1847-3219	3.21	-13.37	0.80	0.33	1.92	0.91	16
J1850+5903	88.92	23.18	0.00	0.00	∞	0.15	5
J1850-2652	8.73	-11.76	0.88	0.16	2.56	0.81	15
J1856+0114	34.60	-0.54	0.80	0.50	1.51	9.94	8
J1858-2137	14.21	-11.15	0.00	0.00	0.56	1.12	14
J1903+0550	39.52	-0.05	0.35	0.18	0.60	9.00	7
J1904-1124	24.22	-8.12	0.24	0.00	0.67	1.60	12
J1911-2000	16.87	-13.22	0.27	0.00	0.60	1.72	13
J1921-2015	17.81	-15.60	52.62	2.67	∞	1.01	14
J1928+1733	52.71	0.07	0.82	0.43	2.01	3.68	8
J1935-4022	358.65	-25.23	4.67	1.45	199.30	2.80	6
J1937-1529	23.95	-17.12	82.30	2.69	∞	2.01	10
J1940-0121	37.41	-11.62	4.58	1.13	∞	1.21	7
J1949-3456	5.25	-26.29	2.83	1.00	164.05	1.03	8
J1955-1414	27.01	-20.56	0.89	0.37	2.42	1.51	8
J1958+2909	66.23	-0.16	0.46	0.15	0.98	2.73	10
J1958-4443	354.85	-30.13	58.02	5.85	∞	0.00	4
J1959+6342	96.61	17.10	0.00	0.00	0.49	1.38	6
J2006-2321	18.82	-26.26	30.22	1.86	∞	1.82	6
J2016+3657	74.76	0.98	0.37	0.08	0.75	3.80	10
J2020+4017	78.05	2.08	0.07	0.00	0.18	12.04	10
J2020-1545	28.09	-26.62	0.00	0.00	0.80	0.76	4
J2021+3716	75.58	0.33	0.29	0.11	0.53	5.66	10
J2022+4317	80.63	3.62	0.13	0.00	0.50	2.45	10
J2025-0744	36.90	-24.38	1.10	0.57	3.58	3.22	4
J2027+3429	74.08	-2.36	0.00	0.00	0.28	2.63	10
J2033+4118	80.27	0.73	0.20	0.00	0.37	7.41	10
J2034-3110	12.25	-34.64	2.88	0.89	154.84	0.92	7
J2035+4441	83.17	2.50	0.00	0.00	0.42	3.28	10
J2036+1132	56.12	-17.18	0.12	0.00	0.77	1.47	6
J2046+0933	55.75	-20.23	0.00	0.00	0.57	1.81	7
J2055-4716	352.56	-40.20	0.99	0.44	3.71	1.50	5
J2100+6012	97.76	9.16	0.15	0.00	0.52	2.29	6

Table 8.1   *continued on next page*

Table 8.1 – continued

3EG Name	ℓ	b	τ	L limit	U limit	Avg Flux	Num Obs
J2158-3023	17.73	-52.25	0.40	0.10	0.87	1.62	5
J2202+4217	92.59	-10.44	0.99	0.43	3.48	1.16	9
J2206+6602	107.23	8.34	0.27	0.00	0.63	2.14	6
J2209+2401	81.83	-25.65	0.79	0.00	4.86	0.63	7
J2219-7941	310.64	-35.06	0.00	0.00	0.51	1.16	4
J2227+6122	106.53	3.18	0.10	0.00	0.41	4.33	6
J2232+1147	77.44	-38.58	0.64	0.37	1.16	1.89	8
J2241-6736	319.81	-45.02	0.00	0.00	1.09	0.73	3
J2243+1509	82.69	-37.49	3.42	0.88	3097.37	0.63	8
J2248+1745	86.00	-36.17	1.07	0.43	3.98	1.00	8
J2251-1341	52.48	-58.91	9.49	1.58	∞	1.47	7
J2254+1601	86.11	-38.18	0.89	0.60	1.50	5.11	8
J2255+1943	89.03	-35.43	2.31	0.80	48.58	0.98	8
J2255-5012	338.75	-58.12	0.41	0.00	1.46	1.70	4
J2314+4426	105.32	-15.10	1.72	0.53	150.35	1.71	3
J2321-0328	76.82	-58.07	10.36	1.63	∞	1.76	6
J2352+3752	110.26	-23.54	24.92	1.68	∞	2.91	4
J2358+4604	113.39	-15.82	0.00	0.00	0.33	1.48	4
J2359+2041	107.01	-40.58	0.68	0.06	2.07	0.97	8

Table 8.1: Variability τ of sources in the Third *EGRET* catalog, together with the bounds of the 68% confidence region. The fitted average source flux and number of observations used in calculating τ are also given.

8.5   Variability by Source Class

As can be seen from Table 8.1, the limits on the variability of an individual source are not very strict. By grouping similar sources together, one can more tightly constrain the confidence regions, but the results are meaningful only if the sources truly have the same variability.

For this purpose, the sources were divided into four principal source classes: Unidentified sources, Pulsars, Active Galactic Nuclei (AGN), and sources which are

spatially coincident with Supernova Remnants (SNR). The Unidentified source class was further divided according to the source latitude, and the AGN class was divided according to the strength of the identification as an AGN. These source classes were determined from the "source ID" (and by the "Other Name" category for the SNR associations).

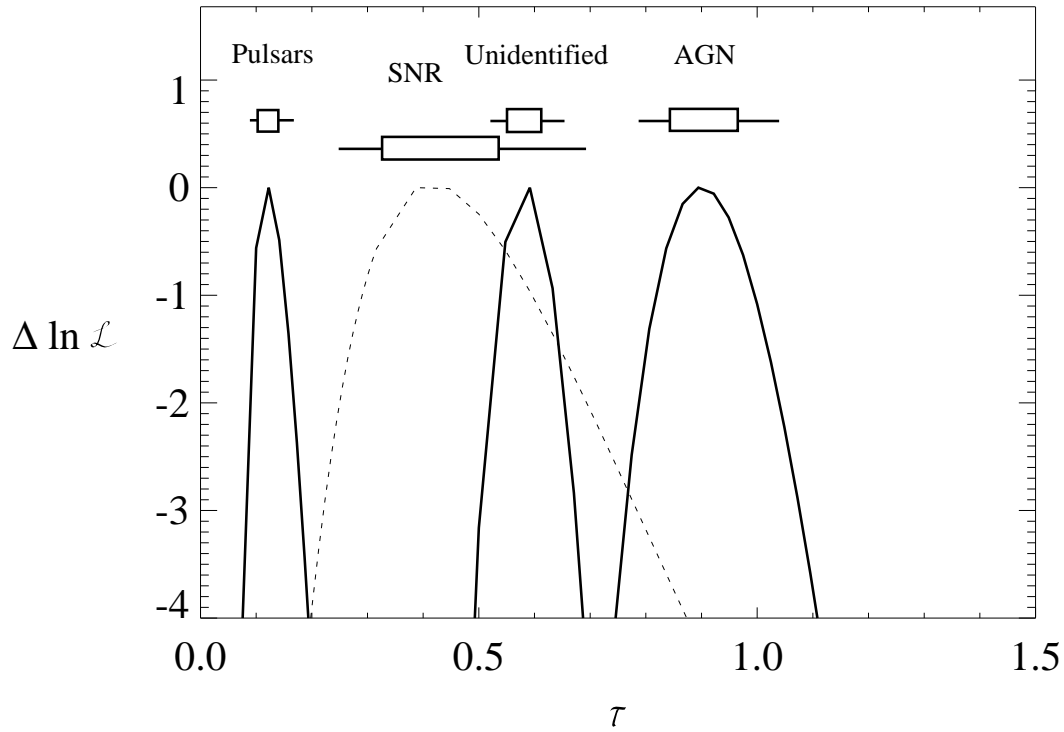The added $\ln \mathcal{L}$ vs τ curves for the different classes are shown in Figure 8.1 below, together with the implied 68% and 95% confidence limits on τ.

Figure 8.1: Log Likelihood vs Variability Index for the four principal source classes: Pulsars, Supernova Remnant associations (dashed), Unidentified sources, and Active Galactic Nuclei. The 68% and 95% confidence regions of τ for each class are indicated by the box and stem, respectively, under each name.

As seen in Figure 8.1, the pulsars, AGN, and unidentified sources clearly differ in their variability. The variability of the five pulsars is about 12%: not significantly higher than the predicted systematic variability for a constant sources of 10%.

The six sources in the SNR source class are not distinguishable from the unidentified sources, on the basis of variability, and show significantly more variation than the pulsar class. The generally weaker flux of these sources leads to the large error bar for this source class.

The change in unidentified source variability with latitude can be seen in Figure 8.2. It is clear from the spatial distribution of the unidentified sources that there are multiple types of astrophysical object which are not being identified [38]. It is clear from Figure 8.2 that the different types of unidentified sources have different variabilities as well. The high latitude sources have a variability index consistent with that of the AGN. The low latitude unidentified sources still exhibit variability, at a level similar to the sources coincident with SNR. Thus the data are not consistent with the hypothesis that these sources are Geminga-like pulsars. The comparatively small error regions for the unidentified source classes stems from the number of unidentified sources. There were 164 unidentified sources: 49 in the low–latitude group, 39 in the mid–latitude group, and 76 in the high–latitude group.
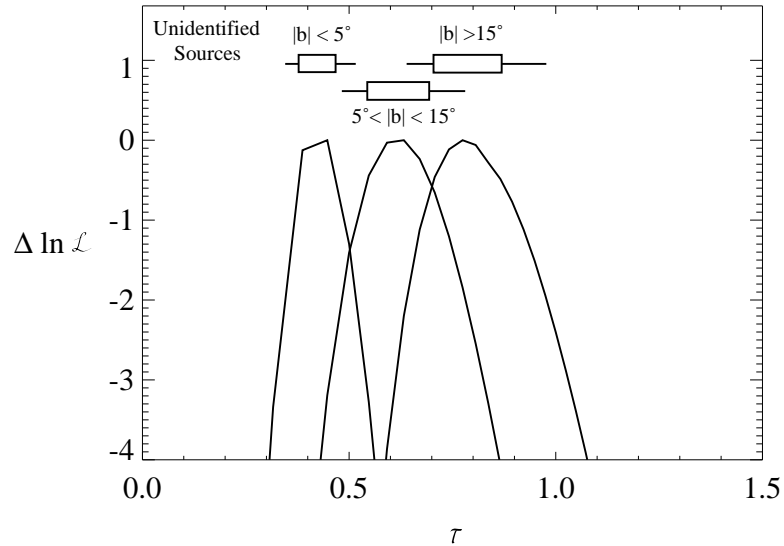
Figure 8.2: Log Likelihood vs Variability Index for the unidentified sources. The sources have been split into three classes based on source latitude, as shown in the figure. The 68% and 95% confidence regions of τ are indicated by the box and stem as in Figure 8.1.

In the Third *EGRET* Catalog, 27 of the 94 sources identified as AGN are listed
as questionable identifications (and marked with an "a" rather than an "A"). In an
effort to see if many of these questionable identifications were mis-identifications, the
variability of these questionable identifications was compared with the variability of
the more confidently identified AGN. As can be seen in Figure 8.3, the two classes
are consistent in their variability. The slightly lower variability seen in the "small a"
class may be due to a selection effect: AGN which flare brightly are more likely to be
identified.
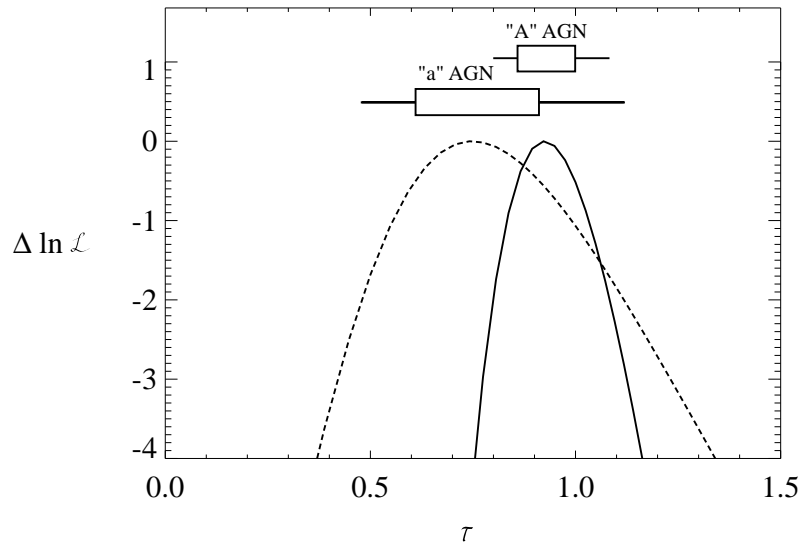
Figure 8.3:   Log Likelihood vs Variability Index for the Active Galactic Nuclei. The
AGN have been split into two classes based on the confidence of their identification
in the Third *EGRET* catalog: "a" for questionable identifications (dashed), and "A"
for confident identifications (solid). The 68% and 95% confidence regions of τ are
indicated by the box and stem as in Figure 8.1.

8.6   The Low Variability Sources

With the variability of the source classes in hand, it is possible to see which sources
can be excluded from a source class based on the variability data. We begin by
examining those sources which are inconsistent with being strongly variable: that is,
the upper bound of the 68% region for τ is small. The list of sources where this upper

bound is less than 0.3 (significantly lower than the AGN or unidentified sources) is shown in Table 8.2.

It is reassuring to see the bright pulsars at the top of the list; the possibility that others on the list might also be pulsars is intriguing. The sources are discussed individually below.

The position of the Crab pulsar, at the top of the list, is a bit surprising given its listing in McLaughlin et al. as moderately variable [66]. There are two reasons for this. The first is the difference in the methods: McLaughlin et al. measure how inconsistent the source is with being constant*. In this analysis, the Crab, Geminga, and Vela pulsars are all inconsistent with being constant at the 95% level. The second reason is the difference in data used: McLaughlin et al. used all measurements up to to 30° from the instrument axis. In this analysis, we have used only data out to 25°, because of the larger systematic errors at higher inclinations.

3EGJ2020+4017 is coincident with the γ-Cyg supernova remnant, and is thus an intriguing pulsar candidate. No pulsed signal has been detected from it, however, and the possibility exists that it is a low variability SNR.

3EGJ1048-5840 is coincident with PSR1046-58, a high $\dot{E}/d^2$ pulsar. Although pulsed emission was not seen in the first three years of *EGRET* data [32], there has been a detection in recent data [54].

3EGJ0222+4253 is coincident with the BL Lac 3C 66A, and is 1° from the position of PSR0218+42, from which pulsed emission above 100 MeV has been detected [101, 60, 41]. In the Third Catalog, the pulsar was not detected as a separate source, and it is suggested that the flux between 100 MeV and 1 GeV is primarily from the pulsar, and the flux above 1 GeV is from 3C 66A [40]. The flux measurements of this "source" will be dominated by the lower energy emission, hence the low variability.

The apparent variability of the Vela pulsar is due to the presence of several artifactual sources nearby. In a few viewing periods, the measured flux of Vela is low, and the flux from an artifact is quite high. Because nearby source fluxes were not re-fit for each point on the likelihood-vs-intensity curve, such "flux-leaking" can lead

---

*More strictly, how inconsistent it is with being 6.5% variable, as they include a 6.5% systematic error.

3EG Name	τ	Lower Limit		Upper Limit		3EG	Notes
		95.5%	68%	68%	95.5%	Identification	
J0534+2200	0.071	0.018	0.058	0.104	0.147	Crab Pulsar	T
J0633+1751	0.122	0.071	0.096	0.162	0.219	Geminga Pulsar	
J2020+4017	0.075	0.000	0.000	0.181	0.321	UnID	C, GeV, T
J1048-5840	0.000	0.000	0.000	0.184	0.403	UnID	C, GeV, T
J0222+4253	0.003	0.000	0.000	0.234	0.599	0219+428	T
J0834-4511	0.173	0.092	0.121	0.237	0.352	Vela Pulsar	T
J1734-3232	0.005	0.000	0.000	0.238	0.547	UnID	C, GeV
J0239+2815	0.000	0.000	0.000	0.242	0.679	0234+285?	
J1058-5234	0.000	0.000	0.000	0.248	0.529	PSR B1055-52	
J1314-3431	0.004	0.000	0.000	0.252	0.685	1313-333?	
J0510+5545	0.000	0.000	0.000	0.264	0.577	UnID	em
J1710-4439	0.163	0.000	0.058	0.266	0.387	PSR 1706-44	
J1045-7630	0.002	0.000	0.000	0.279	0.736	UnID	em, C
J0721+7120	0.083	0.000	0.000	0.282	0.536	0716+714	T
J2027+3429	0.005	0.000	0.000	0.282	0.753	UnID	em, C
J1621+8203	0.000	0.000	0.000	0.292	0.958	UnID	em, C
J0435+6137	0.004	0.000	0.000	0.299	0.772	UnID	em, C

T: See note in text

C: Listed as confused in 3EG

GeV: Detected above 1 GeV in (REF?)

em: Listed as extended morphology in 3EG

Table 8.2:   Sources with low probability of being highly variable. The sources are sorted by the upper limit of the 68% confidence region, and all sources where the this limit is less than 0.3 are shown. The list includes all five pulsars listed in the Third *EGRET* catalog, as well as two unidentified sources from which pulsation has been reported (see notes in the text). Detection above 1 GeV indicates a relatively hard spectrum: another attribute of pulsars. The extended morphology and confused nature of several of the sources might indicate emission from diffuse gas which is not accounted for in the gas map.

to an apparently high variability. By fixing the fluxes of the spurious sources one could lower Vela's variability, but only if those nearby sources were not themselves variable. This was not done because of the unknown biases that could result.

3EGJ0721+7120 is identified in the Third Catalog as the BL Lac 0716+714 [40, 72, 74]. The presence of a definitely identified AGN on the list indicates a few of the limitations of the method. The upper end of the 95.5% confidence region for τ is 0.54, well below the typical AGN variability of ~ 0.9. In large part, this is because this source had no dramatic flares during any observations. The model of the variability is that the standard deviation of the source is constant, and this quiescent blazar had a low variability between these observations. In addition, the highest and lowest fluxes were each averaged with a different observation, because of the one month averaging system (§8.2, §7.2.5). A more sophisticated model might pick up longer or shorter term trends.

8.7 The High Variability Sources

From Table 8.1, 35 sources have a 68% confidence region which has a lower bound greater than 1.0. These include 15 sources identified as AGN, as well as the solar flare. The unidentifed sources are primarily at high latitudes, and are thus generally assumed to be AGN [40]. The few low latitude, unidentified, sources are listed in Table 8.3.

Because the V statistic used by McLaughlin et al. indicates how improbable it is that the observations come from a constant source, the use of the τ statistic in this way is nearly equivalent to the use of V to find variable sources. Indeed, when there is a close correspondence between 2EG and 3EG sources, sources with a high V also have a high lower limit on τ.

8.8 Variability Measurements with *GLAST*

The two limitations on the variability measurements above are the number of distinct observations of a source's flux, and the accuracy of those measurements. As seen from

3EG Name	ℓ	b	τ	Lower Limit 95.5%	68%	Notes
J1828+0142	31.90	5.78	3982.5	> 1.5	6.92	em,C
J1704-4732	340.10	-3.79	29.9	1.1	2.67	C
J1837-0423	27.44	1.06	12.0	1.1	2.16	em, C

Table 8.3:   Low latitude unidentified sources which are unlikely to have low variability. The sources are sorted by the lower bound of the 68% confidence region for τ.

Table 8.1 and Figure 8.4, many of the sources had few observations, and this (together with the often large error bars in the measurements themselves) leads to large errors in the determination of τ.
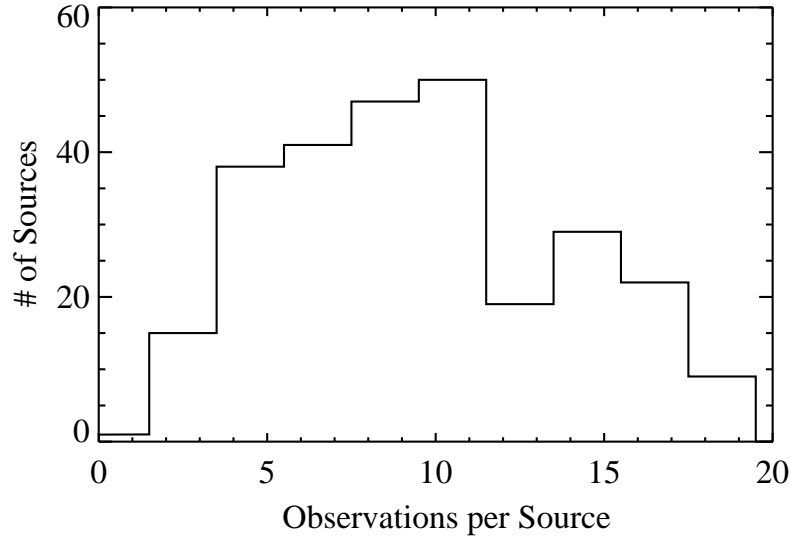
Figure 8.4:   Distribution of Number of Observations from Table 8.1.

The proposed *GLAST* mission will address both of these limitations, and thus offers great promise for measurements of variability. The large field of view of *GLAST* implies a much larger number of observations, and the improved sensitivity means that the error bars on τ will be much smaller. In addition, with the scanning mode of the *GLAST* instrument, it will be possible to look at variation on a continuous range of time intervals from several hours (for bright sources) to months.

The improved quality and quantity of data will also permit more sophisticated models of the variability, as discussed in §7.3.

8.9   Conclusions

The τ statistic was calculated for the sources in the Third *EGRET* Catalog, as well as for several classes of sources. As expected, pulsars exhibited little variability, while the AGN showed very large variability on a month timescale. The unidentified sources showed indications of increasing variability with increasing latitude, indicating that they are a mixture of two or more types of sources with different spatial distributions and variabilty.

For a few sources, the confidence regions for τ could exclude the possibility that the source belonged to the AGN or the pulsar source class. For most sources, however, the confidence regions were too large to make any strong conclusions about the source. Future measurements should allow much better measurements of the variability of gamma ray sources.

Chapter 9

Testing the *GLAST* Design

The designs for the *GLAST* instrument discussed in §2.5 have been refined through much computer simulation. In order to verify the results of those simulations, as well as demonstrate the state of the detector technology, a prototype instrument was tested in a tagged γ-ray beam at the Stanford Linear Accelerator Center (SLAC) in October 1997 [81]. The prototype consisted of models of the three detector systems: the silicon tracker, calorimeter, and the anti-coincidence detector. The performance of each subsystem was evaluated, and the results of the tests were compared with detailed simulations of the instrument. The ability of the simulations to predict the performance of this prototype validated the simulations used to to design the *GLAST* instrument.

9.1   The SLAC Test Beam

The Stanford Linear Accelerator Center (SLAC) contains a two mile linac designed to produce electrons and positrons at energies of up to 50 GeV, in bunches containing approximately 100 billion particles. In order to obtain the single γ-rays desired for the October 1997 Beam test, the energy contained in a few of these electrons was converted into γ-rays, then back into electrons, then back into γ-rays.

At the end of the linac (Figure 9.1), each bunch of electrons or positrons is collimated with the use of a small aperture (Figure 9.2). This collimated beam of charged
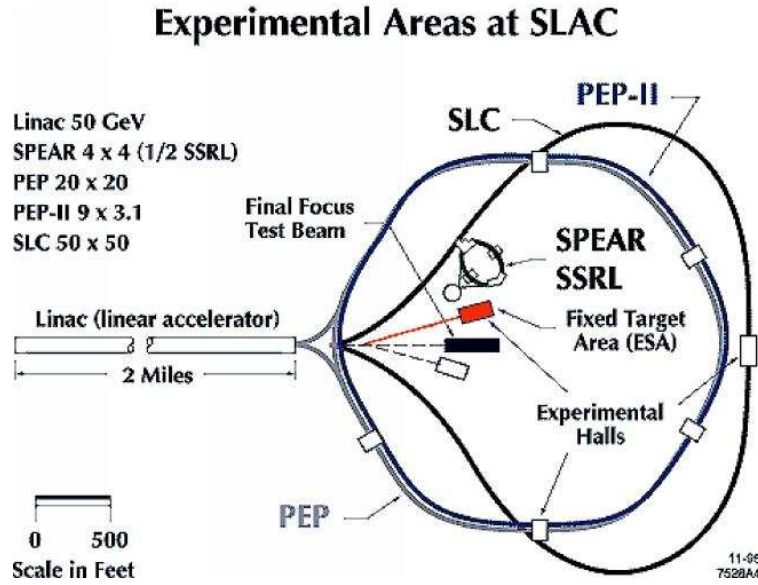
Figure 9.1:   Layout of the Stanford Linear Accelerator Center

particles is then steered around the Stanford Linear Collider (SLC) to the SLC Large Detector (SLD). Those particles which hit the shields around the aperture, however, produce γ-rays which are unaffected by the steering magnets and continue forward. When these γ-rays impact a plate of high-Z material, they pair produce and form a beam of electrons and positrons with a large spread of momenta.

As illustrated in Figure 9.2, electrons with a certain range of momenta are selected from this beam. This monoenergetic beam of electrons is then focused and steered into End Station A (ESA).

Inside ESA (Figure 9.3), two possible setups existed. This beam of electrons could be steered into the *GLAST* prototype for high energy electro-magnetic shower studies of the calorimeter. Or, a copper foil could be inserted into the beam, and a sweeping magnet (called B∅) turned on. In this configuration, the bremsstrahlung γ-rays produced in the coper foil were incident on the prototype instrument, and its capabilities as a pair conversion telescope could be measured.

The ESA electron beam was tunable from 5 GeV to 40 GeV, and the rate of electrons could be controlled via the collimation slits. Most of the gamma ray data
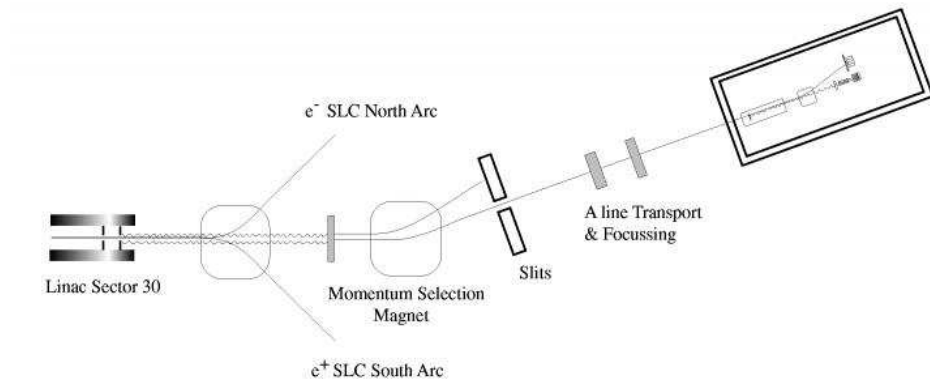
Figure 9.2:   Schematic representation of the End Station A beamline
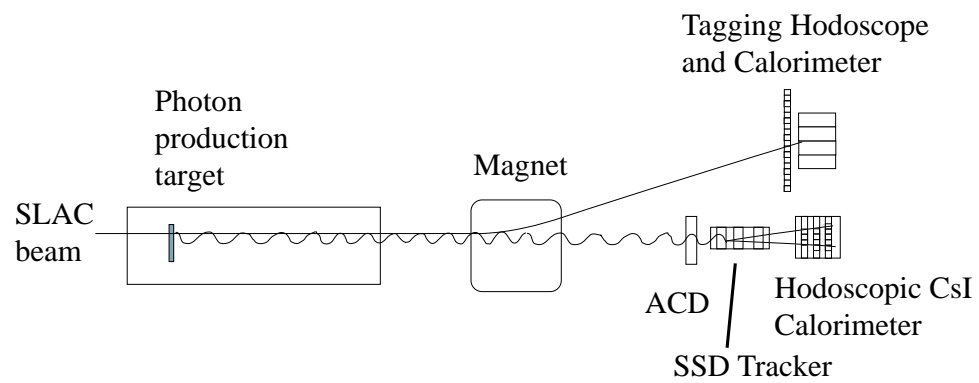
Figure 9.3:   Schematic of the tagged photon beam

were taken with a 25 GeV electron beam, with a rate of approximately one electron per pulse.

The tagging hodoscope and calorimeter permitted a measurement of the energy of the electron after the bremsstrahlung γ-ray was emitted, and thus a measurement of the energy of the γ-ray, since the beam energy was known. In addition, it permitted the rejection of events where multiple electrons might have emitted γ-rays in the copper target.

9.2   The *GLAST* Prototype Instrument

9.2.1   The Silicon Tracker

The directional measurement of the e^+/e^- pair from a γ-ray conversion in the test instrument was performed in the silicon tracker. This scaled down version of the *GLAST* tracker was constructed at by the Santa Cruz Institute for Particle Physics at the University of California, Santa Cruz. A schematic layout can be seen in Figure 9.4. In order to measure several different instrument configurations, the tracker was constructed to allow the separation of planes to be changed, and for the Pb conversion sheets to be exchanged for sheets of various thickness.

The Silicon Strip Detectors (SSD) used were $5 \times 5 \times .05$ cm high purity Si, with a strip pitch of 236 μm. The number of readout chips available for these detectors was limited. Thus each SSD had 192 instrumented strips, corresponding to an area of 4.6×5 cm.

The two competing effects which cause error in the reconstructed direction of a track are the multiple scattering of the track at each plane, and the measurement error due to the finite strip pitch of the detector. The former is due primarily to the Pb converter foils in each layer; the latter is proportional to the strip pitch divided by the distance between planes (as this is the angular measurement error). By varying the separation of the tracker planes and the thickness of the converter foils, all areas of this parameter space could be explored, and the simulations checked. Even though many of the configurations would never be used for a space telescope, it is important
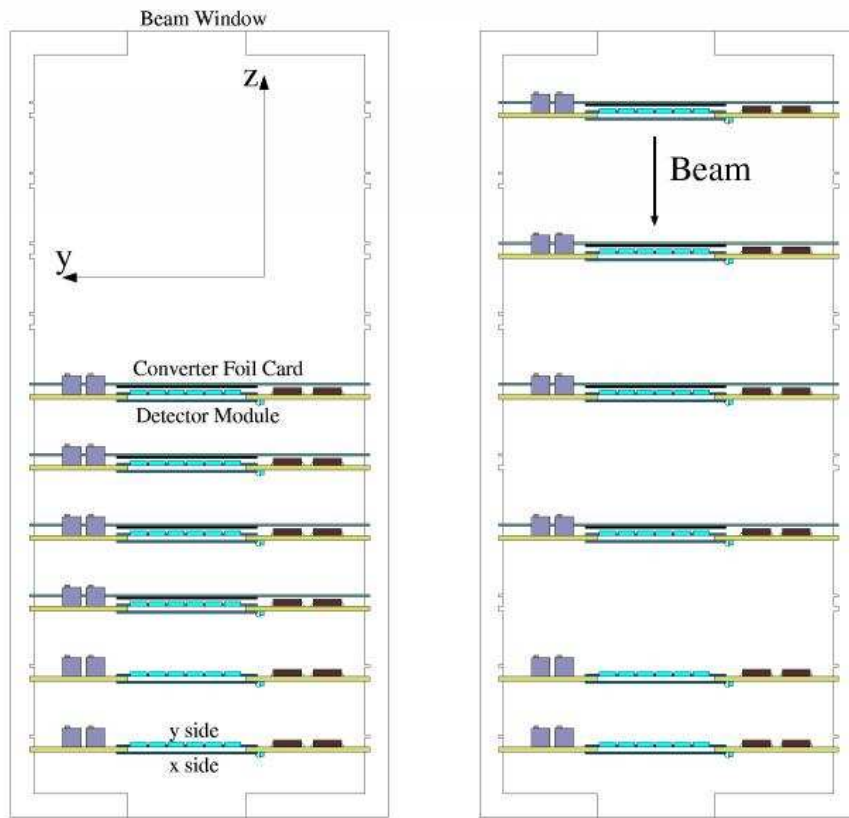
Figure 9.4: Layout of the prototype tracker. The "pancake" configuration is shown on the left and the "stretch" configuration on the right. Note the converter foil cards in front of the first four planes.

that the Monte Carlo results agree with experiment if the Monte Carlo is to be believed.

9.2.2   The CsI(Tl) Calorimeter

The energy measurement by the beam test instrument was performed by a calorimeter prototype constructed by the Gamma and Cosmic Ray Astrophysics Branch at the Naval Research Laboratory. It consisted of eight layers of logs, with six of the 3 x 3 x 24 cm logs in each layer, alternating in orientation as shown in Figure 9.5. Only 24 of the logs were instrumented CsI(Tl), the other logs were Cu with holes drilled through them to obtain the same number of radiation lengths per log. The locations of the instrumented logs can also be seen in Figure 9.5.

A detailed study of the calorimeter can be found elsewhere [81]. For the tracker-oriented analysis presented here, the calorimeter was used as a monolithic block. The energy deposited in each log was summed to find the energy of the photon which had converted in the tracker. This measurement was typically more accurate than that obtained by the tagging hodoscope.

9.2.3   The Anti-Coincidence Detector

The Anti-Coincidence Detector (ACD) was assembled by the Laboratory for High Energy Astrophysics at Goddard Space Flight Center. The principal role of the plastic scintillator ACD in the *GLAST* mission is to serve as a means to reject incoming charged particles: thus the utility of such a detector in the beam test might be questioned. The *GLAST* ACD has several unique challenges, however, and tests of this system were as important as the tests of the other systems.

The problem faced in the design of the ACD is that high energy gamma rays produce a backsplash of X-rays which trigger the plastic scintilator tiles of the ACD. Roughly half of the 10 GeV photons detectable by *EGRET* are self-vetoed in this way. There are many possible steps to solving to this problem: the most important is the segmentation of the ACD. By vetoing events only when the ACD triggers near the incoming particle trajectory, the majority of the backsplash vetos can be eliminated.
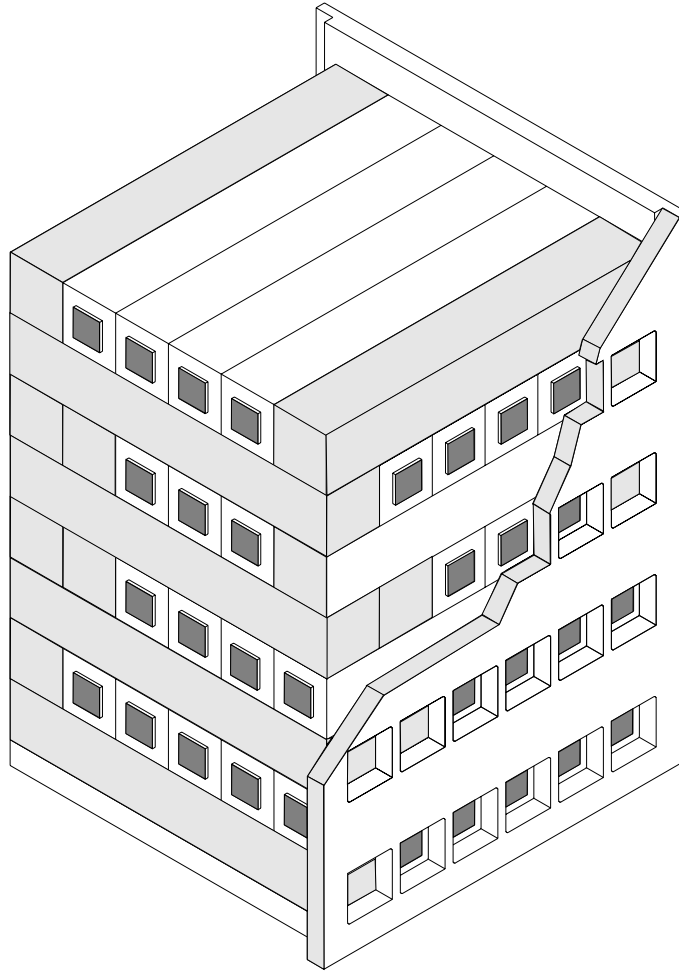
Figure 9.5: Schematic representation of the prototype Calorimeter. The non-instrumented logs are shown in gray.

Anti-Coincidence Detector

Wave-shifting
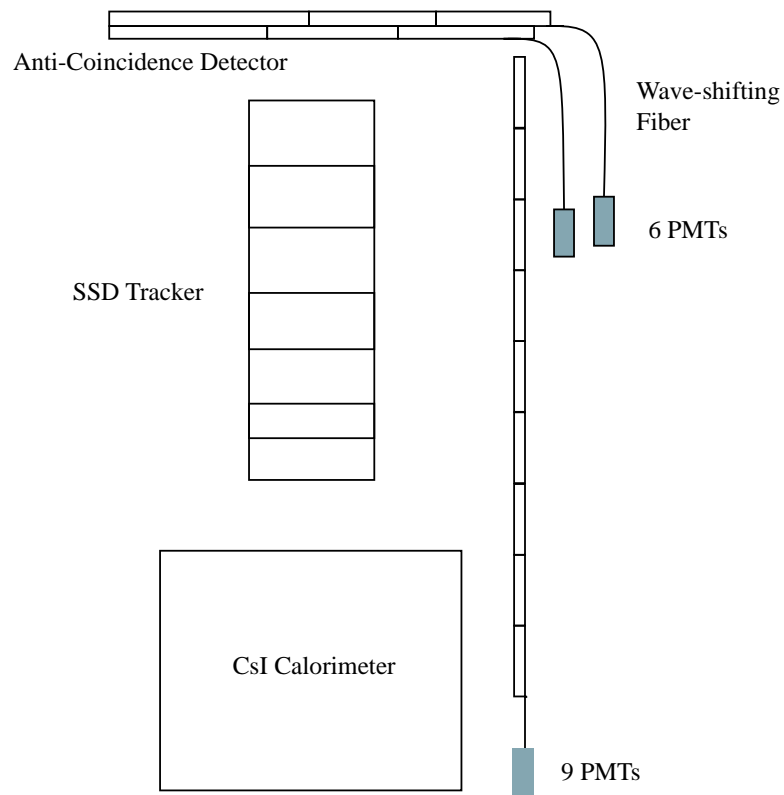Fiber

6 PMTs

SSD Tracker

CsI Calorimeter

9 PMTs

Figure 9.6:   Layout of the components of the beam test instrument.

Another possibility is the use of an ACD with two layers of scintillator, as was tried in the beam test (Figure 9.6).

The ACD used in the beam test was composed of 1 cm thick paddles of Bicron BC-408 plastic scintillator, read out by waveshifting fibers connected to photomultiplier tubes. Nine of these paddles were placed along the side of the instrument, and two sets of three paddles were placed in front. This configuration permitted the measurement of backsplash over a wide area.

9.3 Data taken in the October 1997 test

9.3.1 The Raw Data

Over 400 runs collected 200 gigabytes of data during the 30 days of the beam test. Data were collected 24 hours a day, seven days a week during the runs, by the 30 collaboration members who worked shifts. The 210 million triggers were stored on the SLAC computers [2], where preliminary filtering was done.

9.3.2 Pre-Processing of the Data

The first steps in processing the γ-ray runs were two cuts based on the calorimeter and the tracker. Either three consecutive planes in the tracker must have fired, or more than 6 MeV must have been deposited in the calorimeter. This eliminated 80% of the triggers, and the reduced data were then offloaded to other computers for more processing.

Each event used in the analysis was required to pass several more stringent cuts. First, the Pb glass blocks used in the tagging hodoscope must have indicated that there was only one electron in the bunch (Figure 9.7). This lowered the probability of having mutiple γ-rays produced at the bremstrahlung target. Second, the Anti-Coincidence tiles through which the γ-ray beam passed were required to have less than 1/4 of the energy deposited by a minimum ionizing particle (MIP) in each (Figure 9.8). This ensures that the gamma ray did not convert inside the scintilating tile. Three more cuts were imposed based on the parameters of the reconstructed tracks:

tracks must have had at least three hits regardless of the energy in the calorimeter (Figure 9.9), have had a reduced $\chi^2 < 5$ (Figure 9.10), and the starting position of the track must have been at least 4.7 mm from the edge of the tracker (Figure 9.11). This last requirement lowered the probability that a track might escape the tracker, which could bias the reconstructed track directions.
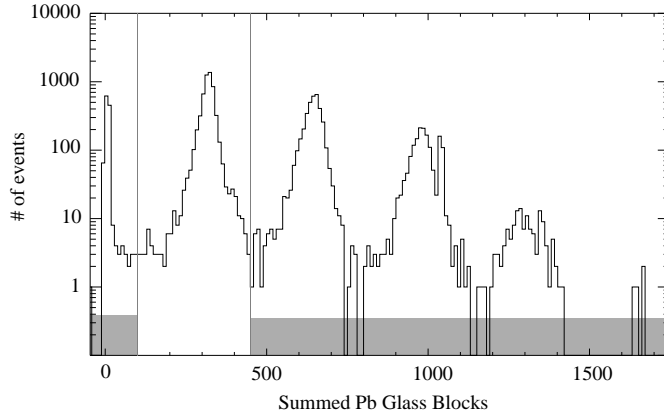

Figure 9.7: Cut based on the summed signal from the Pb Glass hodoscope. The peaks are from various numbers of electrons in a bunch. All events in the upper shaded region were discarded. Events in the lower shaded region which also received less than 5 GeV in the prototype calorimeter were also discarded.

9.4 Simulations

Simulation played two roles in the October 1997 beam test. Simulations of the beam setup and the instrument were crucial for determining how the beam test should be run. But more importantly, these simulations were compared to the beam test results after the test, which enabled the *GLAST* team to judge the quality of the simulation package.

Monte Carlo simulations of the full *GLAST* instrument have been performed with a program called `glastsim` developed by the *GLAST* team. This program is based on `gismo` [5], an object oriented Monte Carlo package written in C++. `gismo`, in turn, incorporates several interaction packages: `EGS` [76], which contains
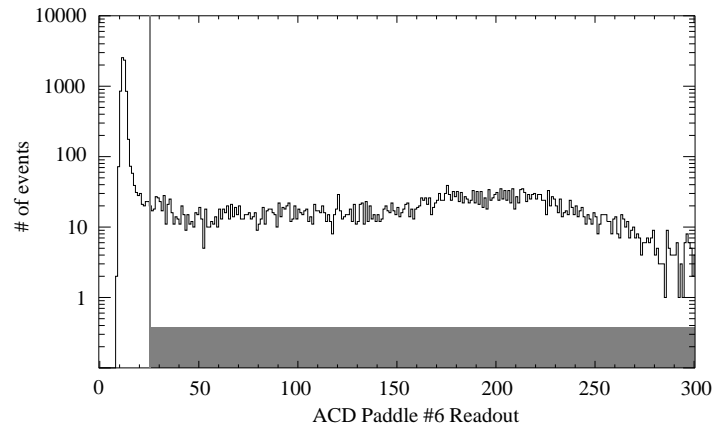
Figure 9.8:   Cut based on ACD paddle #6. A similar cut was imposed on paddle #2, the other paddle directly in front of the tracker.
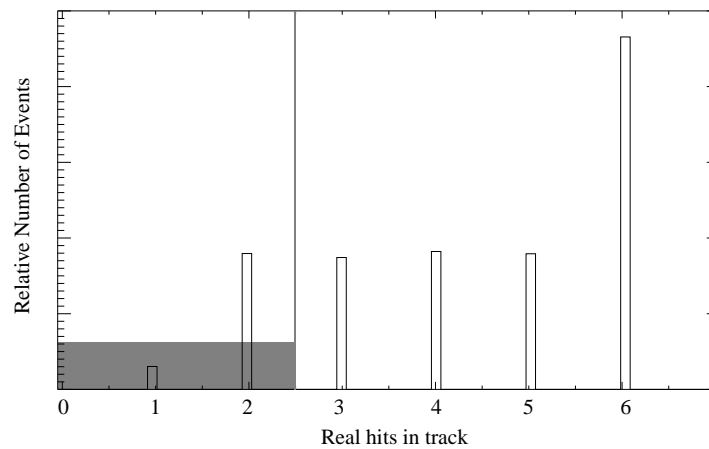

Figure 9.9:   Because fake hits were permitted when a track apparently went through a dead strip, it was required that at least three of the hits in the track be real hits.
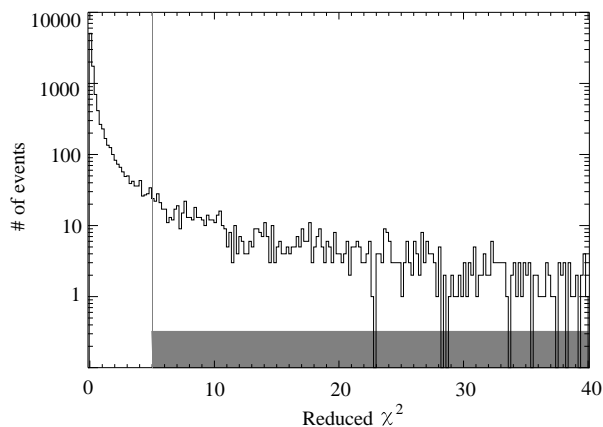
Figure 9.10:   Both particle tracks from the pair conversion were required to pass a quality cut: that the reduced χ^2 was less than 5.
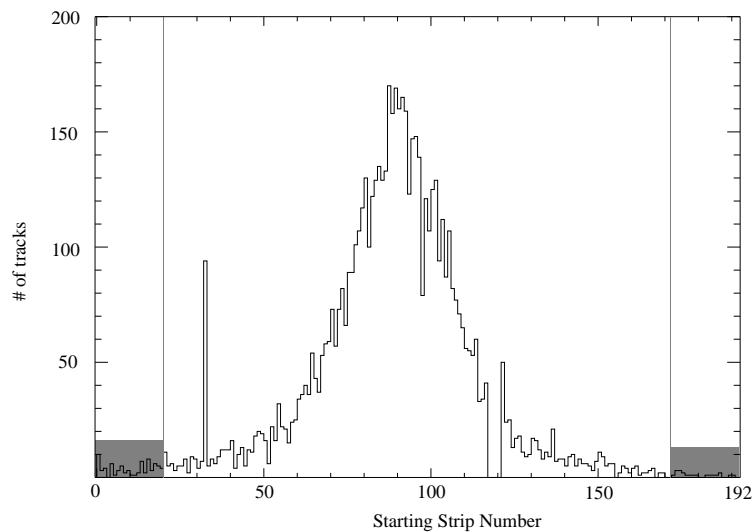

Figure 9.11:   To ameliorate selection effects, tracks which began near the edge of the tracker were eliminated. The same cut was imposed in the X and Y projections.

the electromagnetic interactions, and `GHEISHA` [28, 29] which contains the hadronic interactions.

The simulations of the beam test instrument were performed with a modified `glastsim` program. The geometry of the instrument was incorporated, as well as the beam charactaristics. In order to provide as realistic a simulation as possible, the starting configuration of the simulation had a 25 GeV electron incident on a 3.5% radiation length copper radiator. The beam spot size and collimation were modelled as accurately as possible. Bremsstrahlung γ-rays from the radiator then illuminated the instrument, while the incident electrons were swept away by a magnetic field, just as B∅ did in the real experiment.

The modelled calorimeter was not always incorporated into the simulations: because simulating the high-energy shower development could be quite compute intensive, it was faster to gather simulated data by using an input γ-ray beam, with no calorimeter. This was done when only the tracker response for a given γ-ray energy was needed.

The final modification of the `glastsim` code was the addition to `EGS` of a realistic, polarized cross-section for γ-ray pair conversion, due to Ion Yadigaroglu. In general, the effect of using this cross-section rather than the standard `EGS` pair conversion cross-section was small, but for some simulations this more sophisticated treatment was desired.

The output of the simulation was treated identically to the beam test data. Cuts performed on one were also performed on the other, and strips which were found to be noisy or dead in the beam test instrument were masked out of both datasets. Thus, a comparison of the results was straightforward.

Chapter 10

Beam Test Setup

10.1 Alignment of *GLAST* Prototype

In order to measure the precise direction of the tracks in the detector, it is necessary to know the position and orientation of the detector elements. One option would be to precisely align each of the detector planes and the calorimeter, and to maintain that alignment while the detector is handled (and in the case of *GLAST* , launched). This would, however, be time consuming and would impose additional constraints on the design of the structure holding the instrument together. A better option is to determine the actual alignment while the detector is in use, by using straight tracks to determine the relative positions of the detector elements.

10.1.1 Finding Straight Tracks

The first step, then, is to find the straight tracks which will be used to align the detector. In the beam test instrument, this was fairly straightforward: there was a high frequency of high energy γ-ray events which could be used. If, for some reason, there were not enough of these, there was also data taken with 25 GeV electrons. In the orbital *GLAST* instrument, it will be necessary to use high energy cosmic rays as well, as the flux of high energy γ-rays will not give sufficient data for a quick alignment.

It is necessary then, to select data which have "clean", straight tracks. This can be accomplished somewhat by looking for events which deposit significant energy in the calorimeter. In addition, it is necessary to do a reconstruction of the tracks, and look for outlying hits. Tracks with many outliers can be rejected, and not used for the alignment. There is a bit of a "chicken-and-egg" problem here, however: in order to reconstruct the tracks, some alignment must be assumed. By assuming that the instrument is aligned at the beginning, but by not penalizing the tracks significantly for larger scattering values, it is possible to find the tracks for the alignment.

In addition, there is the problem of multiple hits. Because adjacent strips can fire even when there is a single track, there is the issue of which hit to pick (or whether to generate a virtual hit in between the two). In the beam test, the strip which minimized scatter was used, which tended to straighten out tracks to conform to the assumed alignment of the instrument.

Because of these effects, it is necessary to iterate the process of finding tracks, and then aligning the planes based on those tracks. At each iteration, the track selection procedure will select better tracks, and the estimate of the position of each plane will get better.

10.1.2   The Alignment Parameters

In order to describe the position and orientation of one detector plane relative to a fixed reference (such as the bottom plane), six parameters are needed: three positional and three rotational. Because a given plane of the test instrument measures only one of the X or Y position of a track which is nearly in the Z direction, only one of the three positional parameters is important. For a detector plane which measures the X position of a track, this would be the X position of the plane. Similarly, only one of the three rotations is important: the one about the Z axis. In addition, the importance of the rotation depends on the size of the detector: for the 6 cm beam test detector with pitch 236μm, rotations of $\sim 0.45°$ are important. The rotation can be measured by examining the dependence of the X offset (§10.1.3) on the Y position of a track. Because rotations about the X and Y axes are not important, it is necessary

to define the Z axis by a means other than the orientation of the bottom plane. If it is defined as the line from the center of the bottom tracker plane to the center of the top tracker plane, then both the top and bottom planes are defined to have no offset in the X or Y direction.

This situation changes somewhat for the *GLAST* instrument. Because tracks might have a large incident angle, it becomes important to measure the Z offset as well as the X offset for an X detector plane. Similarly, all three rotations become important, as they each affect the X and/or Z position of the detected hit. Also, rotations become more important: for a *GLAST* detector plane of 30 cm, with strip pitch of 200μm, rotations of only $\sim 0.076°$ will affect the instrument performance.

10.1.3 The Alignment Algorithm

By fitting a straight line to all of the track hits but one, a projected position for that one hit can be found. If the track were perfectly straight and there were no measurement errors, this residual would indicate the alignment error of the plane relative to the average alignment of the tracker. Because of the measurement error, it is necesary to use a large number of these residuals to estimate the alignment error.

There are several methods one might use to find this estimate from the distribution of residuals. The easiest might be to use the mean, median, or mode of the distribution itself. These all have problems however. The mean can be unduly influenced by outliers caused when the track finding algorithm has failed. The median and the mode are both affected by the non-Gaussian nature of the measurement error: because the measurements are discretized, the distribution is not continuous, but instead is spiky from the strip aliasing (Figure 10.1).

By adding some Gaussian noise (with standard deviation equal to the strip pitch), this aliasing may be dispensed with, and the median or mode may be used freely (Figure 10.2). In cases with fewer data, the histogram could be convolved with a Gaussian, resulting in the same curves, but with less noise in each bin. As seen from plane 1 in Figure 10.2, there will be a difference between using the median and the
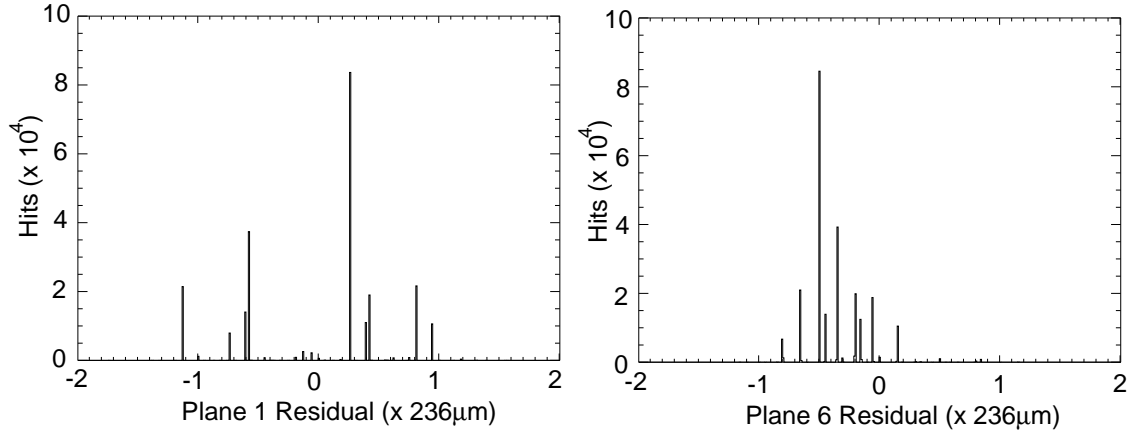
Figure 10.1:   The distribution of residuals for two planes in the prototype instrument. Note the general offset in the plane 6 data, and the peaks separated by one strip (236 μm) in plane 1. Most planes exhibit such double peaks; they are easily understood if one visualizes the residual distribution for on-axis tracks when only a single plane is offset.

mode, due to the asymmetry in the distribution. For the beam test data, the median was used to determine the alignment parameters.

The assumed position of each plane can then be adjusted by the median residual as discussed above. As the position of the first and last plane might now be non-zero, the positions can be translated and rotated so that the coordinate system based on the first and last planes is maintained.

By iterating the process of finding residuals and adjusting the plane positions until the positions converge, a consistent set of plane positions may be found for a given set of tracks. At this point, a new set of tracks can be found, followed by another round of plane adjustments, until the same tracks are found each time.

10.1.4   Alignment Results

The principal determination from the alignment calculations is that the test beam instrument was very close to being aligned. No significant rotation of the planes was detected, and the planes were generally aligned to within one strip pitch (236μm).

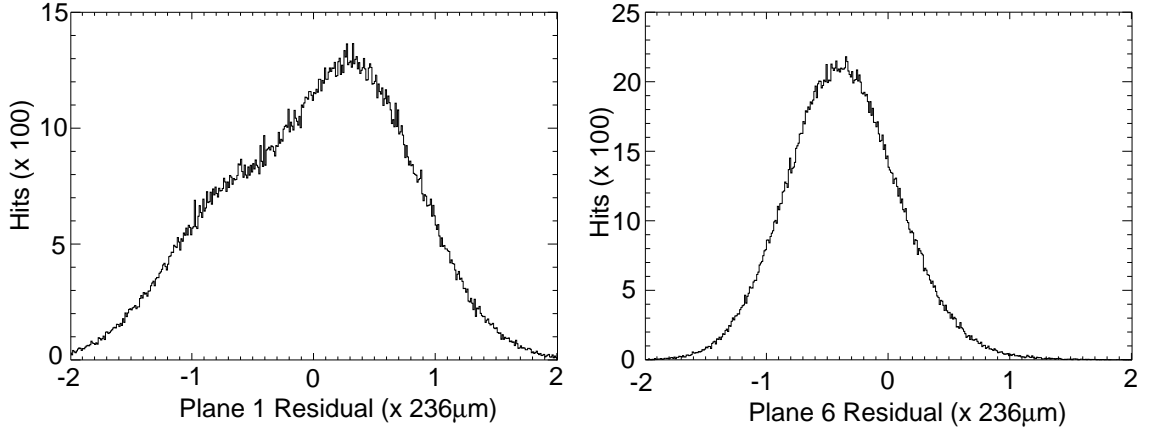Figure 10.2: The distributions shown in Figure 10.1, after the addition of Gaussian noise. The median can now be used to measure the offset error.

Configuration	Direction	Plane 1	Plane 2	Plane 3	Plane 4	Plane 5	Plane 6
Stretch	X	0.000	-0.179	0.176	0.365	0.237	0.000
Stretch	Y	0.000	-0.509	-0.264	0.138	-0.218	0.000
Pancake	X	0.000	-0.92	0.184	0.103	0.083	0.000
Pancake	Y	0.000	-0.058	-0.161	-0.134	-0.060	0.000

Table 10.1: Alignments for the four tested configurations in the Fall 1997 Beam Test. Alignments are in units of strip pitch $(= 236\mu m)$. Planes 1 and 6 define the coordinate system, and thus are identically zero.

The determined alignments are given in Table 10.1, and some sample residual distributions after alignment are shown in Figure 10.3.

10.2 The Reconstruction Algorithm

The reconstruction of particle tracks was done with the Kalman Filter method [51], which has been widely used for particle tracking in high energy physics [37, 36, 9, 13]. The application of these techniques to *GLAST* has been discussed elsewhere ([48, 42]), as has the use for this beam test ([47]). Thus only a brief overview of this technique will be given here.
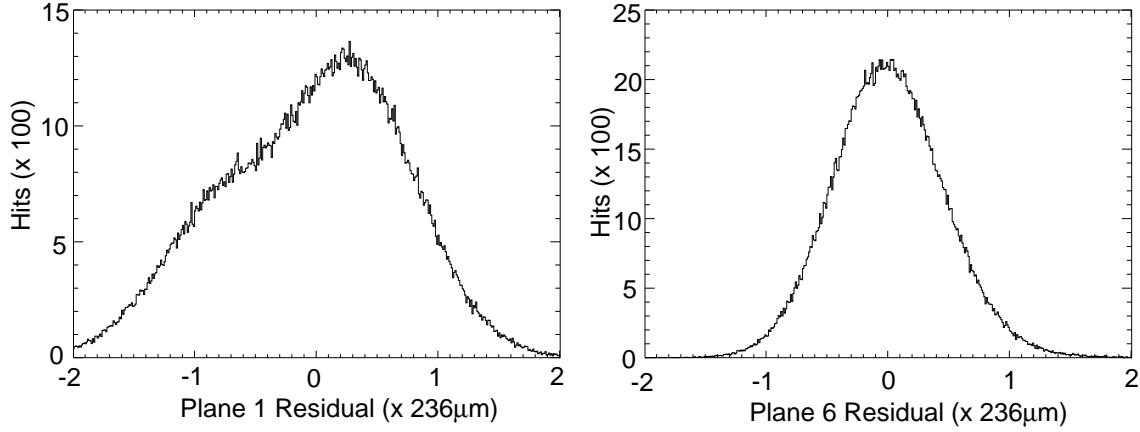
Figure 10.3:   The distributions shown in Figure 10.2, after the iterated alignment procedure discussed in §10.1.3. The second peak (offset by one strip) is again visible in the Plane 1 data.

10.2.1   The Kalman Filter

The Kalman filter is a means to estimate some quantities (termed the "state vector" = $\mathbf{x}$) as a function of time, using some measurements ($\mathbf{m}$), with some errors ($\mathbf{V}$). The k'th measurement is defined through

$$\mathbf{m}_k = \mathbf{H}_k \mathbf{x}_k + \epsilon_k,$$

where $\mathbf{H}_k$ is a matrix relating the state vector to the measured quantities, and ϵ_k represents the error in the measurement. This error is characterized by the covariance matrix $\mathbf{V}_k \equiv \mathrm{cov}[\epsilon_k]$.

The remaining complication to the problem which remains to be specified is that of the evolution of the state vector. If the state vector were the same for all of the measurements, it would be simple enough to perform a least squares fit to the data. This change of the state vector through time is given by the evolution equation

$$\mathbf{x}_{k+1} = \mathbf{F}_k \mathbf{x}_k + \mathbf{w}_k.$$

Where $\mathbf{F}_k$ contains the deterministic component of the evolution, and $\mathbf{w}_k$ the stochastic. Again, $\mathbf{w}_k$ is characterized by its covariance matrix: $\mathbf{Q}_k \equiv \mathrm{cov}[\mathbf{w}_k]$.

It is not difficult to see how to find an estimate of the state vector at one time from a measurement at another. We have

$$\langle \mathbf{x}_k \rangle = \mathbf{H}_k^{-1} \mathbf{m}_k,$$

and can use the evolution equation to find $\langle \mathbf{x}_j \rangle$ given $\langle \mathbf{x}_k \rangle$. Similarly, the covariance of the estimate of $\mathbf{x}_k$ given the one measurement may be found by

$$\mathbf{C}_k \equiv \mathrm{cov}[\bar{\mathbf{x}}_k] = \mathbf{H}_k^{-1} \mathbf{V}_k \left(\mathbf{H}_k^{-1} \right)^T,$$

and by evolving $\mathbf{C}$ appropriately:

$$\mathbf{C}_{k+1} = \mathbf{F}_k \mathbf{C}_k \mathbf{F^T}_k + \mathbf{Q}_k.$$

Note that all these estimates (so far) rely only on one measurement. The complications arise when we wish to use multiple measurements for an estimate. We could simply find all of the estimates for the different measurements independently, and combine them: this would be equivalent to a least squares fit with no correlations between the measurements. The correct approach, however, begins with the realization that the state vector has no "non-local" evolution. Thus, the estimate at time k should be influenced by the best estimate at time $k-1$, but should not explicitly depend on the estimate at time $k-2$. This dependence enters only because the best estimate at time $k-1$ does depend on the estimate at time $k-2$.

This leads us to the filtering equations. Given that we've found the best estimate of the state vector at time k, using the measurements at $t <= k$, how do we find the best estimate at $k+1$ using the measurement at $k+1$? First, we find the best estimate by evolving the old estimate, and then include the new measurement as we would for standard least squares.

The notation here becomes a bit awkward, as we need to denote various estimates and covariances at different times, and also made with different data. Let us write

the estimate at time k, using the data through time k as $\mathbf{x}_k$. The estimate, using the same data, at time $k+1$ we write as $\mathbf{x}_{k+1,\text{proj}}$. The covariance matrices are denoted similarly.

We have

$$\mathbf{C}_k = \left[\mathbf{C}_{k,\text{proj}}^{-1} + \mathbf{H}_k^T \mathbf{V}_k^{-1} \mathbf{H}_k\right]^{-1}, \tag{10.1}$$

$$\mathbf{x}_k = \mathbf{C}_k \left[\mathbf{C}_{k,\text{proj}}^{-1} \mathbf{x}_{k,\text{proj}} + \mathbf{H}_k^T \mathbf{V}_k^{-1} \mathbf{m}_k\right], \tag{10.2}$$

$$\mathbf{x}_{k+1,\text{proj}} = \mathbf{F}_k \mathbf{x}_k, \tag{10.3}$$

and

$$\mathbf{C}_{k+1,\text{proj}} = \mathbf{F}_k \mathbf{C}_k \mathbf{F}_k^T + \mathbf{Q}_k. \tag{10.4}$$

With the above equations, the best estimate of the state vector at some time n can be found by iteration, beginning with k=1 and progressing to $k = n$. The only difficulty is the specification of $\mathbf{x}_{1,\text{proj}}$ and $\mathbf{C}_{1,\text{proj}}$. This is essentially the prior estimate of the state vector. The safest option is to pick a sensible value for $\mathbf{x}_{1,\text{proj}}$, with a very large error matrix $\mathbf{C}_{1,\text{proj}}$. As the elements of the error matrix approach infinity, the initial value for $\mathbf{x}_{1,\text{proj}}$ will not matter. Equivalently, one may take $\mathbf{C}_{1,\text{proj}}^{-1} = 0$.

10.2.2   The Kalman Smoother

What, though, if the best estimate of the state vector using later measurements as well as earlier ones is desired? One could simply run the Kalman filter backwards, and combine the two (independent) estimates at time k. Alternatively, one can define a sort of "back-correction-propagator",

$$\mathbf{A}_k \equiv \mathbf{C}_k \mathbf{F}_k^T \mathbf{C}_{k+1,\text{proj}}^{-1}.$$

Defining our desired estimate (using all the data) as $\mathbf{x}_{k,\text{smooth}}$, we have

$$\mathbf{x}_{k,\text{smooth}} = \mathbf{x}_k + \mathbf{A}_k(\mathbf{x}_{k+1,\text{smooth}} - \mathbf{x}_{k+1,\text{proj}}), \tag{10.5}$$

and

$$\mathbf{C}_{k,\text{smooth}} = \mathbf{C}_k + \mathbf{A}_k(\mathbf{C}_{k+1,\text{smooth}} - \mathbf{C}_{k+1,\text{proj}})\mathbf{A}_k^T. \qquad (10.6)$$

These smoothing equations can be iterated from the final measurement back to the first, yielding a set of estimates using all of the measurements.

10.2.3   Limitations of the Kalman Equations

As noted above, the Kalman formalism is equivalent to least squares fitting, and thus is equivalent to the maximum likelihood analysis when the two stochastic terms ($\mathbf{w}_k$ and ϵ_k) are Normally distributed. The benefit of the Kalman filter approach is the speed with which estimates can be found: in $\mathcal{O}(N)$ time, where N is the number of measurements, with simple matrix operations (on small matrices) at each step. The alternative, for a straightforward least squares fit, would require inverting a correlation matrix of size N, which is $\mathcal{O}(N^3)$. The straightforward maximum likelihood computation would involve maximizing a function of ND variables, where D is the number of components in the state vector $\mathbf{x}$.

What though, of the case when the formalism breaks down? This might happen in many different ways: the evolution operator $\mathbf{F}$ might not be linear, or the scattering term $\mathbf{w}$, or the error term ϵ might not have a Gaussian distribution. Alternatively, these terms might depend on the state vector. These cases may be approached with changes of variables, although with differing degrees of difficulty [49, 50, 90, 80].

Linearizing $\mathbf{F}$ is common in high energy applications, because of the curved particle tracks in a magnetic field. When measurement points are sufficiently close together, this linearization is not a problem. Note that measurements can be made arbitrarily close by inventing new measurements, where the error on the measurement is infinite.

For the case of the beam test, no extensions to the Kalman formalism were used. Because tracks were necessarily almost perpendicular to the planes (or else the track escaped the tracker, and thus was not seen), the scattering and error matrices had little dependence on the state vector. Similarly, although multiple scattering at large

angles is not Gaussian, this effect was minimized in the tracker, because large angle scatters deflected out of the instrument.

Chapter 11

Results of the Beam Test

11.1 Characterization of the Point Spread Function

The principal characterization of the SSD tracker in the beam test is the Point Spread Function (PSF), or the distribution of reconstructed directions given a collimated beam of γ-rays at a specific energy. This distribution for beam test data is compared with that from simulated data at several energy ranges, and for several configurations in Figure 11.1 – Figure 11.4. As can be seen, the real and simulated PSF are very similar, indicating that the simulations do an admirable job of predicting the instrument performance.

11.2 PSF as a function of energy

In order to characterize the PSF as a function of energy, one might typically fit a Gaussian to the distributions described above. Because of the non-Gaussian tails of the distributions, however, it was decided to use the 68% and 95% containment radii instead. Using these two numbers to summarize the data from distributions like those in Figure 11.1, the plots in Figure 11.5 were constructed. Again, good agreement is seen between the beam test data and the simulations.
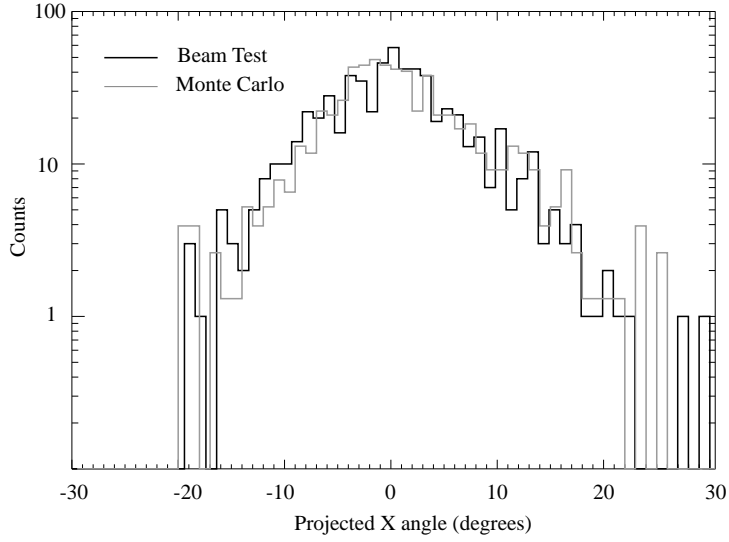
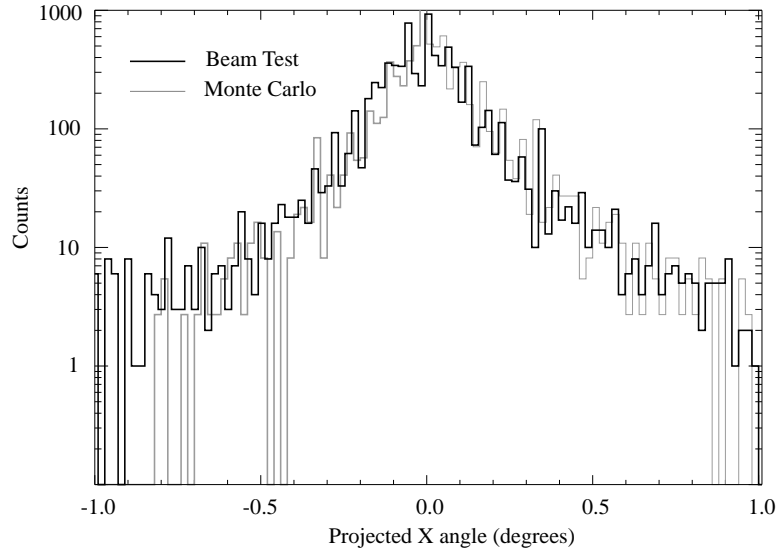Figure 11.1: PSF for 10–20 MeV γ-rays, with 2% R.L. Pb radiators, in the Pancake configuration.

Figure 11.2: PSF for 10–20 GeV γ-rays, with 4% R.L. Pb radiators, in the Pancake configuration.
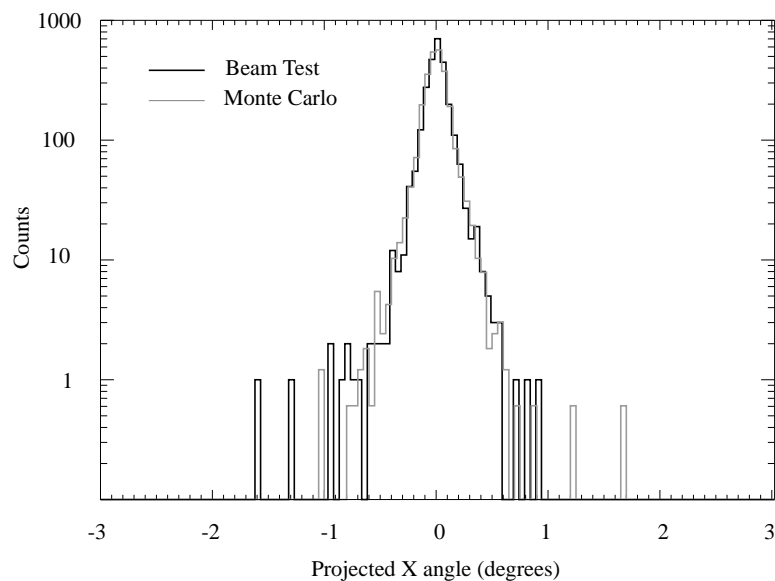
Figure 11.3:   PSF for 2–5 GeV γ-rays, with no Pb radiators, in the Stretch configuration.
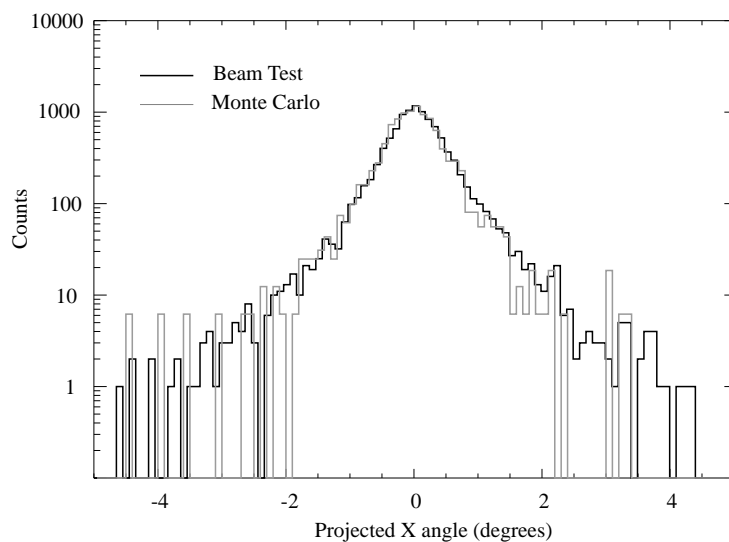

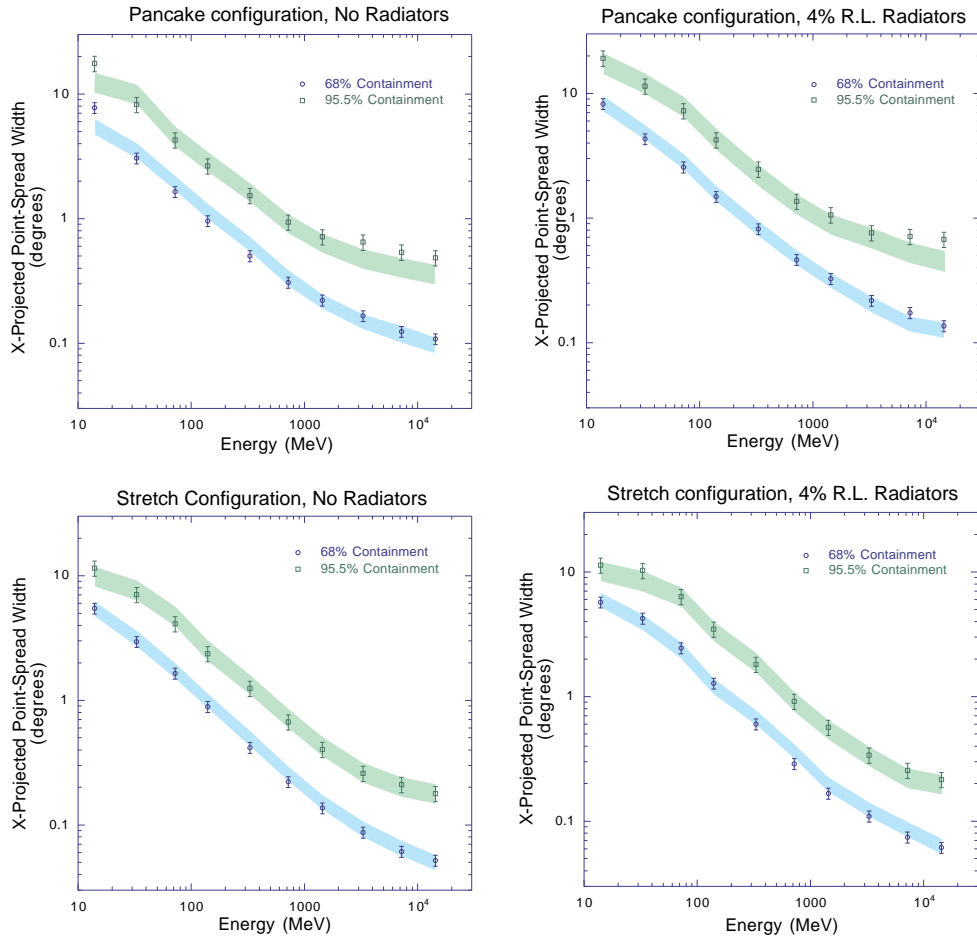Figure 11.4:   PSF for 500–1000 MeV γ-rays, with 6% Pb radiators, in the Stretch configuration.

Figure 11.5: PSF vs Energy for four different instrument configurations. The Monte Carlo data are represented by the shaded band. Error bars are 2σ.

11.3   Conclusion

The Fall 1997 beam test set out to demonstrate the validity of many components of the *GLAST* project: from the detector and readout technology of the three separate detectors, to the generation of a γ-ray beam which can be used to calibrate the full *GLAST* instrument, to the simulations around which the detector design is being based.

As seen from the data shown in the previous sections, in all of these respects the beam test was quite a success. The γ-ray beam was well collimated, all three detectors performed as expected, and the simulations of the *GLAST* prototype instrument proved to be quite accurate.

This verification of the *GLAST* design and detector technology paves the way for the next stage of the *GLAST* project: a prototype tower to be constructed for beam (and possibly flight) tests in the fall of this year.

Bibliography

[1] Aldous, D., *Probability Approximations via the Poisson Clumping Heuristic* (Springer-Verlag), 1989.

[2] Anthony, P. L. and Szalata, Z. M., *Flexible high performance VME based data acquision system for the ESA physics program*, SLAC-PUB-7201, 1996.

[3] Arnold, J. *et al.*, Journal of Geophysical Research, **67**, 4876, 1962.

[4] Atwood, W. B., *Gamma-Large Area Silicon Telescope (GLAST) Applying Silicon Detector Technology to the Detection of Gamma-Rays in Space*, Nuclear Instruments and Methods in Physics Research, **342**, 1, 302–307, Mar 1994.

[5] Atwood, W. B., Burnett, T., Cailliau, R., Myers, D. R., and Storr, K. M., *GISMO: An Object Oriented Program for High Energy Physics Simulation and Reconstruction*, International Journal of Modern Physics, **C3**, 459, 1992.

[6] Bayes, T., *An Essay Towards Solving a Problem in the Doctrine of Chances*, Biometrika, **45**, 293–315, 1958. Reprint of 1763.

[7] Bertsch, D. L., Dame, T. M., Fichtel, C. E., Hunter, S. D., Sreekumar, P., Stacy, J. G., and Thaddeus, P., *Diffuse Gamma-Ray Emission in the Galactic Plane from Cosmic-Ray, Matter, and Photon Interactions*, Astrophysical Journal, **461**, 2, 587–600, Oct 1993.

[8] Bignami, G. F., *The* COS-B *Experiment for γ-ray Astronomy*, Space Science Instruments, **1**, 245, 1975.

[9] Billoir, P. and Qian, S., *Simultaneous Pattern Recognition and Track Fitting by the Kalman Filtering Method*, Nuclear Instruments and Methods in Physics Research, **A294**, 219–228, 1990.

[10] Bloom, E. D., *GLAST*, Space Science Reviews, **75**, 1–2, 109–125, Jan 1996.

[11] Bloom, E. D., Godfrey, G., and Ritz, S. (editors), *Proposal for the Gamma-ray Large Area Space Telescope*, Feb 1998. SLAC-R-522.

[12] Bloom, S. *et al.*, *Short Time-scale Gamma-Ray Variability of Blazars and EGRET Unidentified Sources*, in C. Dermer, M. Strickman, and J. Kurfess (editors), *Proceedings of the Fourth Compton Symposium*, vol. 410 of *AIP Conference Proceedings*, p. 1262, 1997.

[13] Bock, R., Grote, H., Notz, D., and Regler, M., *Data Analysis Techniques for High-Energy Physics Experiments* (Cambridge University Press), 1990.

[14] Browning, R., Ramsden, D., and Wright, P., *Detection of Pulsed Gamma Radiation from the Crab Nebula*, Nature, **232**, 99, 1971.

[15] Cash, W., *Parameter-Estimation in Astronomy through Application of the Likelihood Ratio*, Astrophysical Journal, **228**, 3, 939–947, 1979.

[16] Caso, C. *et al.*, *Review of Particle Properties*, European Physical Journal, **C3**, 1998.

[17] Catelli, J. R., Dingus, B. L., and Schneid, E. J., EGRET *Observations of Bursts at MeV Energies*, in *Proceedings of the Fourth Huntsville Gamma-Ray Burst Symposium*, 1997.

[18] Cheng, K. S., Ho, C., and Ruderman, M., *Energetic Radiation from Rapidly Spinning Pulsars. I. Outer Magnetosphere Gaps*, Astrophysical Journal, **300**, 500–521, Jan 1986.

[19] —, *Energetic Radiation from Rapidly Spinning Pulsars. II. Vela and Crab*, Astrophysical Journal, **300**, 522–539, Jan 1986.

[20] Clark, G., Garmire, G., and Kraushaar, W., *Observation of High-Energy Cosmic Gamma Rays*, Astrophysical Journal Letters, **153**, L203, 1968.

[21] Crichfield, C. *et al.*, Physical Review, **85**, 461, 1952.

[22] Daugherty, J. K. and Harding, A. K., *Electromagnetic Cascades in Pulsars*, Astrophysical Journal, **252**, 337, 1982.

[23] Dingus, B. L., Catelli, J. R., and Schneid, E. J., *Bursts Detected and NOT Detected by* EGRET *Imaging Spark Chambers*, in *Proceedings of the Fourth Huntsville Gamma-Ray Burst Symposium*, 1997.

[24] Eadie, W. T., Drijard, D., James, F. E., Roos, M., and Sadoulet, B., *Statistical Methods in Experimental Physics* (Amsterdam: North-Holland), 1971.

[25] Esposito, J. *et al.*, EGRET *Observations of Radio-Bright Supernova Remnants*, Astrophysical Journal, 1996.

[26] Esposito, J. A. *et al.*, *In-Flight Calibration of the Energetic Gamma-Ray Experiment Telescope (EGRET) on the Compton Gamma Ray Observatory*, Astrophysical Journal, 1999. In press.

[27] Feldman, G. and Cousins, R., *Unified Approach to the Classical Statistical Analysis of Small Signals*, Physical Review D, **57**, 7, 3873–3889, April 1998.

[28] Fesefeldt, H., *The Simulation of Hadronic Showers, Physics and Applications*, Tech. rep., RWTH Aachen Report PITHA, Feb 1985.

[29] Fesefeldt, H., Hamacher, T., and Schug, J., *Tests of Punch-Through Simulation*, Nucl. Instrum. Meth. Phys. Res., **A292**, 279, 1990.

[30] Fichtel, C. and Trombka, J., *Gamma-Ray Astrophysics- New Insight Into the Universe* (NASA Reference Publication 1386), 1997.

[31] Fichtel, C. E., Hartman, R. C., Kniffen, D. A., Thompson, D. J., Bignami, G. F., Ögelman, H. B., Özel, M. E., and Tümer, T., *High-Energy Gamma-Ray Results from the Second Small Astronomy Satellite*, Astrophysical Journal, **198**, 163, 1975.

[32] Fierro, J. M., *Observations of Spin-Powered Pulsars with the* EGRET *Gamma-Ray Telescope*, Ph.D. thesis, Stanford University, 1995.

[33] Fierro, J. M. *et al.*, EGRET *High-Energy Gamma-ray Pulsar Studies. II. Individual Millisecond Pulsars*, Astrophysical Journal, **447**, 807–812, 1995.

[34] Fisher, R. A., *Studies in Crop Variation. I An Examination of the Yield of Dressed Grain from Broadbalk.*, J. Agric. Sci., **11**, 107, 1921.

[35] Frontera, F., *Recent Results on Gamma-Ray Bursts with the* BeppoSAX *Satellite*, in *Proceedings of the 25th International Cosmic Ray Conference* (World Scientific Publishing), 1997. Available as `http://xxx.lanl.gov/astro-ph/9802157`.

[36] Frühwirth, R., *Application of Kalman Filtering to Track and Vertex Fitting*, Nuclear Instruments and Methods in Physics Research, **A262**, 444–450, 1987.

[37] Frühwrith, R., *Application of Filter Methods to the Reconstruction of Tracks and Vertices in Events of Experimental High Energy Physics*, Ph.D. thesis, Institut für Hochenergiephysik der Österreichischen Akademie der Wissenschaften, A-1040 Wien, Nikolsdorfergasse 18, Vienna, 1988. HEPHY-PUB 516/88.

[38] Grenier, I. *et al.*, *Spatial Distribution of the Unidentified* EGRET *Sources Off the Galactic Plane*, Advances in Space Research, **15**, 5, 73–6, May 1995.

[39] Harding, A., *Pulsar γ-Rays: Spectra, Luminosities, and Efficiencies*, Astrophysical Journal, **245**, 267–273, 1981.

[40] Hartman, R. C. *et al.*, *The Third* EGRET *Catalog of High-Energy Gamma-Ray Sources*, Astrophysical Journal Supplement, 1999. In press.

[41] Hermsen, W. *et al.*, in *Proceedings of COSPAR, Nagoya*, 1998. Submitted to Advanced Space Research.

[42] Hernando, J.-A., *The Kalman Filter Technique applied to Track Fitting in GLAST*, World Wide Web: `http://scipp.ucsc.edu/groups/glast/pub/offline/kalman.ps`, 1998.

[43] Hulsizer, R. and Rossi, B., *Search for Electrons in the Primary Cosmic Radiation*, Physical Review, **73**, 1402, 1948.

[44] Hunter, S. D., Kinzer, R. L., and Strong, A. W., *Diffuse Galactic Continuum Radiation*, in C. D. Dermer, M. S. Strickman, and J. D. Kurfess (editors), *Proceedings of the Fourth Compton Symposium*, vol. 410, pp. 192–207 (Woodbury, New York: American Institute of Physics), 1997.

[45] Hunter, S. D. *et al.*, EGRET *Observations of the Diffuse Gamma-Ray Emission from the Galactic Plane*, Astrophysical Journal, **481**, 1, 205–240, May 1997.

[46] Hurley, K. *et al.*, *Extended High Energy Emission from a Gamma-Ray Burst*, Nature, **372**, 652, 1994.

[47] Jones, B. B., *A Search for Gamma-Ray Bursts and Pulsars, and the Application of Kalman Filters to Gamma-Ray Reconstruction*, Ph.D. thesis, Stanford University, 1998.

[48] Jones, B. B. and Tompkins, W. F., *A Physicist's Guide to Kalman Filters*, World Wide Web, Mar 1998. `http://razzle.stanford.edu/~bbjones/expkal.pdf`.

[49] Julier, S. J. and Uhlmann, J. K., *A New Extension of the Kalman Filter to Nonlinear Systems*, in *Signal Processing, Sensor Fusion, and Target Recognition VI.: Proceedings of the SPIE*, vol. 3068, pp. 182–93, Orlando, Florida, 1997.

[50] Julier, S. J., Uhlmann, J. K., and Durrant-Whyte, H. F., *A New Approach for Filtering Nonlinear Systems*, in *Proceedings of the 1995 American Control Conference*, pp. 1628–1632, Seattle, Washington, 1995.

[51] Kalman, R. E., *A New Approach to Linear Filtering and Prediction Problems*, Transaction of the ASME—Journal of Basic Engineering, pp. 35–45, Mar 1960.

[52] Kanbach, G. *et al.*, *Detection of a long-duration solar gamma-ray flare on June 11, 1991 with* EGRET *on Compton-GRO*, Astronomy and Astrophysics Supplement Series, **97**, 1, 349–53, 1993.

[53] —, *Characteristics of Galactic Gamma-Ray Sources in the Second* EGRET *Catalog*, in *3rd Compton Symposium*, vol. 120, pp. C461–4, June 1995. Astronomy & Astrophysics Supplement Series (3 Dec. 1996).

[54] Kaspi, V. *et al.*, *Gamma-ray Observations of the Young Radio Pulsars PSRs B1046-58 and J1105-6107*, in *Proceedings of the Workshop on the Relation Between Neutron Stars and Supernova Remnants, Elba Island, Italy*, 1998.

[55] Kendall, M. G. and Stuart, A., *The Advanced Theory of Statistics* (Charles Griffin and Co. Ltd), 1968.

[56] Kniffen, D. and Fichtel, C., *A Study of Gamma Rays from the Region of the Galactic Center*, Astrophysical Journal, **161**, 3, L157–60, 1970.

[57] Kniffen, D. A., Bignami, G. F., Fichtel, C. E., Hartman, R. C., Ögelman, H. B., Thompson, D. J., Özel, M. E., and Tümer, T., in *Proceedings of the 14th International Cosmic Ray Conference*, vol. 1, p. 100, Munich, 1975.

[58] Kouveliotou, C. *et al.*, *Discovery of a Magnetar Associated with the Soft Gamma Repeater SGR 1900+14*, Astrophysical Journal, **510**, L115–118, Jan 1999.

[59] Kraushaar, W. *et al.*, *High-energy Cosmic Gamma-Ray Observations from the OSO-3 Satellite*, Astrophysical Journal, **177**, 341, 1972.

[60] Kuiper, L. *et al.*, in *Proceedings of the Third INTEGRAL Workshop: "The Extreme Universe"* (Taormina).

[61] Kwok, P.-W. *et al.*, EGRET *Observations of Gamma-Ray Bursts on June 1, 1991 and August 14, 1991*, in M. Friedlander, N. Gehrels, and D. J. Macomb (editors), *Compton Gamma-Ray Observatory Symposium*, vol. 280 of *AIP Conference Proceedings*, pp. 855–859 (New York: American Institute of Physics), 1993.

[62] Lin, Y.-C. *et al.*, EGRET *Observations of the Region to the South of* $b = -30$ *in Phase 1 and Phase 2 of the Compton Gamma Ray Observatory Viewing Program*, Astrophysical Journal Supplement, **105**, 331, Aug 1996.

[63] Mattox, J. R. *et al.*, *The Likelihood Analysis of* EGRET *Data*, Astrophysical Journal, **461**, 396, Apr 1996.

[64] Mayer-Hasselwander, H. and Simpson, G., COS-B *Gamma-Ray Sources Beyond the Predicted Diffuse Emission*, in *The Energetic Gamma Ray Experiment Telescope (EGRET) Science Symposium*, p. 153, 1989.

[65] Mayer-Hasselwander, H. *et al.*, *High-Energy Gamma-Ray Emission from the Galactic Center*, Astronomy and Astrophysics, **335**, 161–172, July 1998.

[66] McLaughlin, M. A., Mattox, J. R., Cordes, J. M., and Thompson, D. J., *Variability of* CGRO/EGRET *Gamma-Ray Sources*, Astrophysical Journal, **473**, 763, Dec 1996.

[67] Meegan, C. A., Fishman, G. J., Wilson, R. B., Paciesas, W. S., Pendleton, G. N., Horack, J. M., Brock, M. N., and Kouveliotou, C., *Spatial distribution of γ-ray bursts observed by* BATSE, Nature, **355**, 143, Jan 1992.

[68] Meegan, C. A. *et al.*, *The Third* BATSE *Gamma-Ray Burst Catalog*, Astrophysical Journal Supplement, **106**, 65–110, 1996.

[69] Merck, M. *et al.*, *Study of the Spectral Characteristics of Unidentified Galactic* EGRET *Sources. Are they Pulsar-Like?*, Astronomy and Astrophysics Supplement Series, **120**, 4, 465, Dec 1996.

[70] Michelson, P. F., NASA Mission Definition Study Proposal, 1995. `http://www-glast.stanford.edu/studyprop/overview.html`.

[71] Montanet, L. *et al.*, *Review of Particle Properties*, Physical Review D, **50**, 1173–1826, 1994.

[72] von Montigny, C., *High-Energy Gamma-Ray Emission from Active Galaxies: EGRET Observations and Their Implications*, Astrophysical Journal, **440**, 525, Feb 1995.

[73] Mukherjee, R., Bertsch, D. L., Dingus, B. L., Kanbach, G., Kniffen, D. A., Sreekumar, P., and Thompson, D. J., *On the Nature of the Unidentified* EGRET *Sources: Are They Geminga-Like Pulsars?*, Astrophysical Journal, **441**, L61–L64, Mar 1995.

[74] Mukherjee, R. *et al.*, *EGRET Observations of High-energy Gamma-Ray Emission from Blazars: An Update*, Astrophysical Journal, **490**, 116, Nov 1997.

[75] Nel, H. I. *et al.*, EGRET *High-Energy Gamma-Rays Pulsar Studies. III. A Survey*, Astrophysical Journal, **465**, 898–906, Jul 1996.

[76] Nelson, W. R., Hirayama, H., and Rogers, D. W. O., *The EGS4 Code System*, Tech. Rep. SLAC-265, Stanford Linear Accelerator Center, 1985.

[77] Nolan, P. L. *et al.*, EGRET *Observations of Pulsars*, Astronomy and Astrophysics Supplement Series, **120**, 4, C61–C64, Dec 1996.

[78] Pollock, A. *et al.*, *The Einstein View of the Wolf-Rayet Stars*, Astrophysical Journal, **320**, 1, 283–95, Sept 1987.

[79] Pollock, A. M. T., Bignami, G. F., Hermsen, W., Kanbach, G., Lichti, G. G., Masnou, J. L., Swanenburg, B. N., and Wills, R. D., *Search for Gamma-Radiation from Extra-Galactic Objects Using a Likelihood Method*, Astronomy and Astrophysics, **94**, 1, 116–120, 1981.

[80] Regler, M. and Frühwirth, R., *Reconstruction of Charged Tracks*, in *Proceedings of the Advanced Study Institute on Techniques and Concepts in High Energy Physics* (Plenum Publishing Corporation), 1988.

[81] Ritz, S. *et al.*, *Beam Test of Gamma-Ray Large Area Space Telescope Components*, Nuclear Instruments and Methods, in preparation.

[82] Romani, R. W. and Yadigaroglu, I.-A., *Gamma-Ray Pulsars: Emission Zones and Viewing Geometries*, Astrophysical Journal, **438**, 314–321, 1995.

[83] Schein, M. *et al.*, *The Nature of the Primary Cosmic Radiation and the Origin of the Mesotron*, Physical Review, **59**, 615, 1941.

[84] Schneid, E. J. *et al.*, EGRET *detection of high energy gamma rays from the gamma-ray burst of 3 May 1991*, Astronomy and Astrophysics, **255**, L13, May 1992.

[85] —, EGRET *measurements of Energetic Gamma Rays from the Gamma-Ray Bursts of 1992 June 22 and 1994 March 1*, Astrophysical Journal, **453**, 95–99, Nov 1995.

[86] Schönfelder, V. *et al.*, *Instrument Description and Performance of the Imaging Gamma-Ray Telescope* COMPTEL *aboard the Compton Gamma-Ray Observatory*, Astrophysical Journal Supplement, **86**, 2, 657, Jun 1993.

[87] Sommer, M. *et al.*, *High Energy Gamma Rays from the Intense January 31, 1993 Gamma Ray Burst*, Astrophysical Journal Letters, **422**, L63, Feb 1993.

[88] Sreekumar, P. *et al.*, *Observations of the Large Magellanic Cloud in High-Energy Gamma-Rays*, Astrophysical Journal Letters, **400**, L67, Dec 1992.

[89] —, EGRET *Observations of the Extragalactic Gamma-Ray Emission*, Astrophysical Journal, **494**, 523–534, Feb 1998.

[90] Stampfer, D., Regler, M., and Frühwirth, R., *Track Fitting with Energy Loss*, Computer Physics Communications, **79**, 157–164, 1994.

[91] Sturner, S. *et al.*, *Association of Unidentified, Low Latitude* EGRET *Sources with Supernova Remnants*, Astronomy and Astrophysics, **293**, 1, L17–20, Jan 1995.

[92] Sveshnikov, A. A., *Problems in Probability Theory, Mathematical Statistics, and Theory of Random Functions* (Dover), 1989.

[93] Thompson, D., Simpson, G., and Özel, M., SAS-2*Observations of the Earth Albedo Gamma Radiation Above 35 MeV*, Journal of Geophysical Research, **86**, A3, 1265, March 1981.

[94] Thompson, D. *et al.*, *EGRET Detection of Gamma Rays from the Moon*, American Astronomical Society Meeting, **189**, 25.02, 1996.

[95] Thompson, D. J., Fichtel, C. E., Hartman, R. C., Kniffen, D. A., and Lamb, R. C., *Final* SAS-2 *Gamma-Ray Results on Sources in the Galactic Anticenter Region*, Astrophysical Journal, **213**, 252, 1977.

[96] Thompson, D. J., Fichtel, C. E., Kniffen, D. A., and Ögleman, H. B., SAS-2 *High-Energy Gamma-Ray Observations of Vela Pulsar*, Astrophysical Journal Letters, **200**, L79, 1975.

[97] Thompson, D. J., Harding, A. K., Hermsen, W., and Ulmer, M. P., *Gamma-Ray Pulsars: The Compton Observatory Contribution to the Study of Isolated Neutron Stars*, in C. D. Dermer, M. S. Strickman, and J. D. Kurfess (editors), *Proceedings of the Fourth Compton Symposium*, vol. 410, pp. 39–56 (Woodbury, New York: American Institute of Physics), Apr 1997.

[98] Thompson, D. J. *et al.*, *Calibration of the Energetic Gamma Ray Experiment Telescope (EGRET) for the Compton Gamma Ray Observatory*, Astrophysical Journal Supplement, **86**, 629, 1993.

[99] —, EGRET *High-Energy Gamma-Ray Pulsar Studies: I. Young Spin-Powered Pulsars*, Astrophysical Journal, **436**, 229–238, 1994.

[100] —, *The Second* EGRET *Catalog of High-Energy Gamma-Ray Sources*, Astrophysical Journal, **101**, 259–286, Dec 1995.

[101] Verbunt, F. *et al.*, *High-energy Observations of the Millisecond Pulsar PSR J0218+4232*, Astronomy and Astrophysics, **311**, L9–12, July 1996.

[102] Wilks, S. S., *The Large-Sample Distribution of the Likelihood Ratio for Testing Composite Hypotheses*, Annals of Mathematical Statistics, **9**, 60, 1938.

[103] Willis, T. D., *Observations of the Isotropic Diffuse Gamma-Ray Background with the* EGRET *Telescope*, Ph.D. thesis, Stanford University, Aug 1996.

[104] Yadigaroglu, I.-A. and Romani, R. W., *Gamma-Ray Pulsars: Beaming Evolution, Statistics, and Unidentified* EGRET *Sources*, Astrophysical Journal, **449**, 211–215, 1995.

[105] Yost, G. *et al.*, *Review of Particle Properties*, Physics Letters B, **204**, 1–486, 1988.